COHERENTLY-COUPLED VERTICAL-CAVITY LASER ARRAYS

BY

MATTHEW THOMAS JOHNSON

DISSERTATION

Submitted in partial fulfillment of the requirements
for the degree of Doctor of Philosophy in Electrical and Computer Engineering
in the Graduate College of the
University of Illinois at Urbana-Champaign, 2013

Urbana, Illinois

Doctoral Committee:

Professor Kent D. Choquette, Chair
Professor James J. Coleman
Assistant Professor Gabriel Popescu
Assistant Professor Daniel M. Wasserman

ABSTRACT

Coherently-coupled vertical cavity surface-emitting laser (VCSEL) arrays offer a unique approach to beam steering and high-radiance applications, and have many advantages such as small size, low cost, high speed, durability and manufacturing ease. Previous work on coherently-coupled VCSEL arrays has left unfinished the tasks of determining the beam steering mechanism within the arrays and achieving current uniformity across large arrays without resorting to overly-complicated fabrication procedures. This work fulfills the former by establishing a full theoretical connection between the differential current injected into the array elements and the observed steering of the far-field beam. Record high beam-steering speed and phase responsivity are also demonstrated, showing promise for applications in high-speed modulation. The first in-phase emission from a coherently-coupled bottom-emitting VCSEL array is also demonstrated, along with significantly improved current uniformity across larger arrays.

To my beloved Kinetta

ACKNOWLEDGMENTS

I would first like to thank my advisor, Professor Kent Choquette, for his guidance, support, insights, inspiration and intellectual challenges, without which this work would not have been possible. I would also like to thank my committee members, Professor James Coleman, Professor Gary Eden, Assistant Professor Gabriel Popescu and Assistant Professor Daniel Wassermann, for their helpful comments and suggestions, and Colonel John Andrews at the United States Air Force Academy for allowing me this incredible opportunity.

I am fortunate to have built upon a large body of work performed by the photonics devices research group at the University of Illinois on coherently coupled VCSEL arrays. I am especially fortunate to have followed on the work of Dr. Dominic Siriani, and to have benefitted tremendously from his continued interest, comments, and suggestions. I would particularly like to acknowledge his initial suggestion and further insightful and edifying correspondence regarding the application of dynamic coupled mode theory to this work. I would also acknowledge my appreciation for the samples he, Dr. Paul Leisher and Dr. Meng Peun Tan prepared, on which much of this work is based, and for useful discussions and training from Dr. Meng Peun Tan, Dr. Joshua Sulkin, and Dr. Matthias Kasten. I would also like to gratefully acknowledge Bradley Thompson, Zihe Gao and Gautham Ragunathan for their tireless work in

fabricating our latest bottom-emitting samples, and Thomas Fryslie for useful discussions on their design.

On a personal note, I would like to thank my parents and my home fellowship group in Illini Life Christian Fellowship for their prayers and for their interest in my research, which have been a constant motivation and encouragement. Lastly, I would like to express my deepest appreciation and acknowledgment to my beautiful and amazing wife, for her editing, support, patience and understanding.

DISCLAIMER CLAUSE: The views expressed in this article are those of the author and do not reflect the official policy or position of the United States Air Force, Department of Defense, or the U.S. Government.

TABLE OF CONTENTS

Chapter 1: INTRODUCTION

1.1 Motivation and Background

Coherently coupled VCSEL arrays have many features that make them viable candidates for beam steering and high-radiance applications. Applications for non-mechanical optical beam steering include fiber switching, free-space communications and laser radar. Radiance, often referred to as 'brightness', is defined as power per area per solid angle. It is an important figure of merit for applications requiring high power in a small area with low divergence, such as for pumping high power fiber lasers that can only accept power into a small diameter within a limited cone of acceptance, or for free-space optical links, where on-axis power is essential. Vertical cavity surface-emitting lasers (VCSELs) are particularly well suited for such applications due to their small size, low cost, high speed, durability, manufacturing ease, single longitudinal mode and two-dimensional configurability.

1.1.1 Beam Steering

Non-mechanical optical beam steering promises lower cost, higher reliability, lower complexity and higher speed than mechanical approaches, which are typically still the norm for applications such as laser radar [1]. Non-mechanical beam steering was first demonstrated at radio frequencies during World War II with phased array radar. The same advantages of electronic control, reliability, and fast/accurate steering have

motivated efforts to migrate to optical frequencies. The difference in wavelength between the radio and optical spectrum has, however, proven a difficult barrier to overcome, and not due to lack of effort. Phased array beam steering was demonstrated in the optical regime as early as 1971 [2], and the ensuing approaches can be generally classified into continuous and discrete methods. The technique of using liquid crystals for continuous beam steering was introduced in 1975 [3], garnered much attention in the early 1990s [4], and remains the dominant technique for non-mechanical beam steering today [1]. This technology is fundamentally limited, however, to a maximum steering angle of 1^{o} in both orthogonal directions at 81% efficiency, with a maximum steering speed on the order of milliseconds [1]. Alternate approaches for continuous beam steering include microelectromechanical systems [5, 6], surface gratings [7], electrowetting [8, 9], waveguides [10-12] and VCSELs [13-15] .

Among the multiple figures of merit for optical beam steering, speed is still a critical and limiting factor for applications such as laser radar. While mechanical methods clearly have inertial limitations, even the fastest methods using liquid crystals are limited to speeds under 10 kHz [16, 17]. Beam steering above the kHz regime has only been shown previously with grating and waveguide techniques. This is because the index change with these methods can rely more directly on carrier-induced [18], electro-optic [10], or quantum-confined Stark [12] effects, as opposed to slower mechanical or thermal changes. These faster methods, however, are often difficult to extend into two

dimensions, require elaborate setups with feedback control [10], are not conducive to free space propagation [12, 18], or suffer from low efficiency [19]. Phased VCSEL arrays are well-suited for high-speed beam steering applications because they do not share these difficulties. They also have the advantages of very high electro-optical efficiency, a natural extension into two dimensions [14] and of being fabricated with standard lithographic processes onto a monolithic semiconductor wafer.

Phased VCSEL arrays also employ a unique beam steering mechanism. With the exception of injection-locked diode laser arrays [20, 21], all other beam steering methods alter the wavefront of an incident beam. In contrast, herein we demonstrate phase control at the quantum well active region of array elements. VCSEL arrays are fundamentally unique in acting as the source of both the emission and of a temporal phase shift, making them a closer analog to their phased array radar counterpart. This fundamental difference is illustrated in Figure 1.1 with a finite difference time domain (FDTD) simulation comparing beam steering with spatial and temporal phase shifts. Both methods in Figure 1.1 steer the beam in the same direction from normal, as apparent in the tilted wavefronts of the electric fields. The typical method in Figure 1.1a relies on a phase lag introduced in the z direction by the region with a linearly increasing index profile. The second method shown in Figure 1.1b relies on an increasing phase lag introduced along the *x* direction at the source, which is what we observe in phased

VCSEL arrays. The first approach can be understood as a *spatial* phase lag introduced in the z direction, and the second as a *temporal* phase lag introduced at the source.

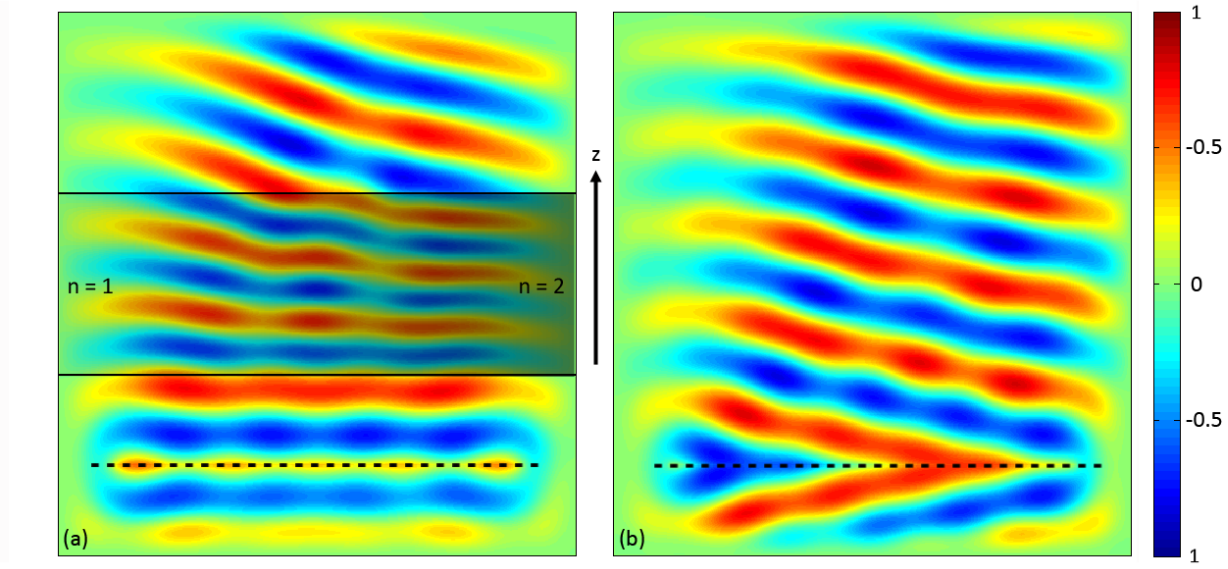

Figure 1.1: FDTD simulation of beam steering, shown by tilted electric field profiles, with (a) spatial and (b) temporal phase shifts. The refractive index is set to one except for the region defined in (a). Dashed lines represent the source.

Since VCSEL arrays offer a fundamentally different approach, our understanding of the physical beam steering mechanism within them has been limited. The primary objective of this work is to further elucidate this steering mechanism, which will aid in optimizing these devices for particular applications. Our approach is to first determine the relative phase of the elements at the VCSEL facet using a Fraunhofer propagation method. We then examine both the beam steering dynamics and spatially-resolved spectra to identify the refractive index and resonant frequency changes occurring within the element cavities. We finally appeal to coupled mode theory to correlate the

observed phase shift with the observed resonant frequency differences between elements.

1.1.2 High Radiance VCSEL Arrays

The high efficiency of diode laser arrays makes them suitable as high-radiance sources for applications such as fiber laser pumps for missile defense [22], where pump radiance remains a limiting factor [23]. Edge-emitting laser arrays have historically dominated this market because they can typically achieve much greater single-mode power per element. Radiance from edge emitters has been scaled up by individually collimating and aligning multiple chips, but the complexity of this approach has caused a recent plateau in scaling efforts, as shown in Figure 1.2. VCSEL arrays offer the primary advantage of two-dimensional scalability, which affords the potential to surpass these limitations.

1.1.2.1 High Power Multimode VCSEL Arrays

While high power is not to be confused with high radiance, a review of the techniques incorporated to achieve high power in multimode VCSELs and VCSEL arrays is informative with regard to achieving high radiance. A historical plot of continuous-wave (CW) high power records is shown in Figure 1.3. Prior to 1993, output power from individual VCSELs was limited to under 20 mW [24]. The first breakthrough came with a bottom-emitting structure with diamond heat sinking and a gain peak optimized

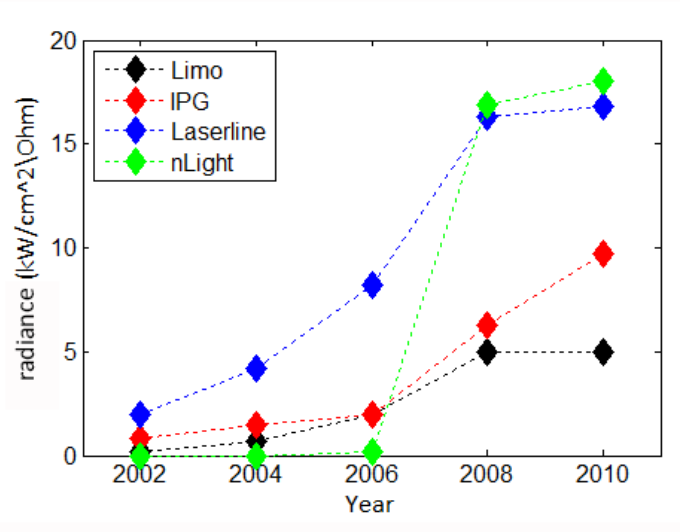

Figure 1.2: Maximum radiance achieved with edge-emitting lasers by various high-power laser manufacturing companies, as sourced from respective websites.

for high temperatures [25]. The importance of thermal management in achieving high power was thus realized early on. The bottom-emitting structure is key to thermal management, as it allows heatsinking at the end of a distributed Bragg reflector (DBR) mirror, reducing the thermal resistance from the active region to the heat sink. It was also noticed later [26] that depositing the top metal contact over the lasing element, as is possible with the bottom-emitting design, significantly balances the carrier density across the aperture, circumventing the problem of current crowding on the aperture perimeter that is found with top-emitting designs. These two distinct advantages of bottom-emitting structures are illustrated in Figure 1.4. The next breakthrough came with realizing the thermal limitations of larger aperture diameters [27], and the need to implement an array of VCSELs in order to continue to scale up the output power [28]. The highest reported CW power of 230 W from a VCSEL array was achieved in 2007 by

Princeton Optronics [29]. The historical plot of Figure 1.3 shows a clear transition to bottom-emitting arrays for increased output power [25,27-34].

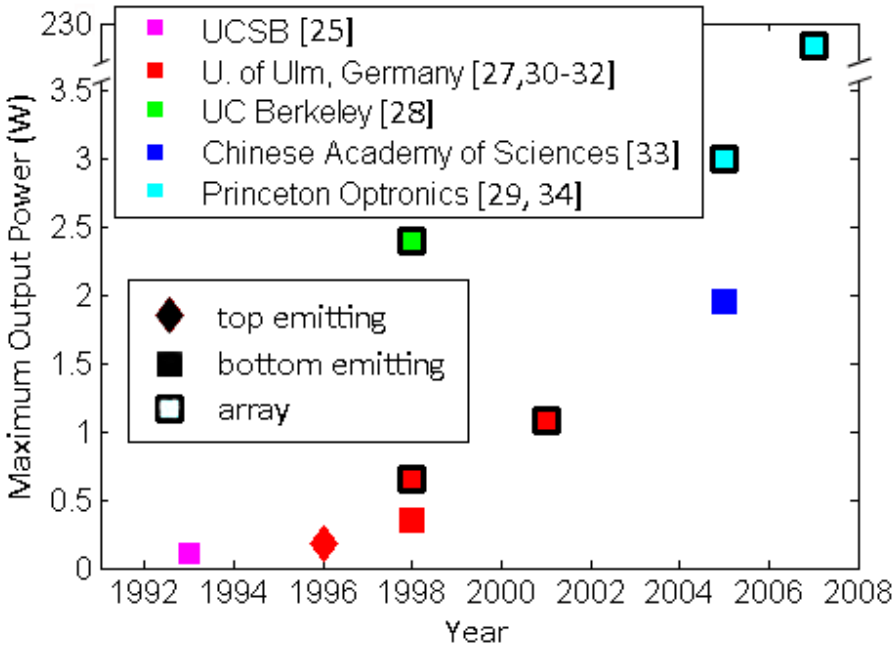

Figure 1.3: Maximum CW output power from multimode VCSELs and VCSEL arrays.

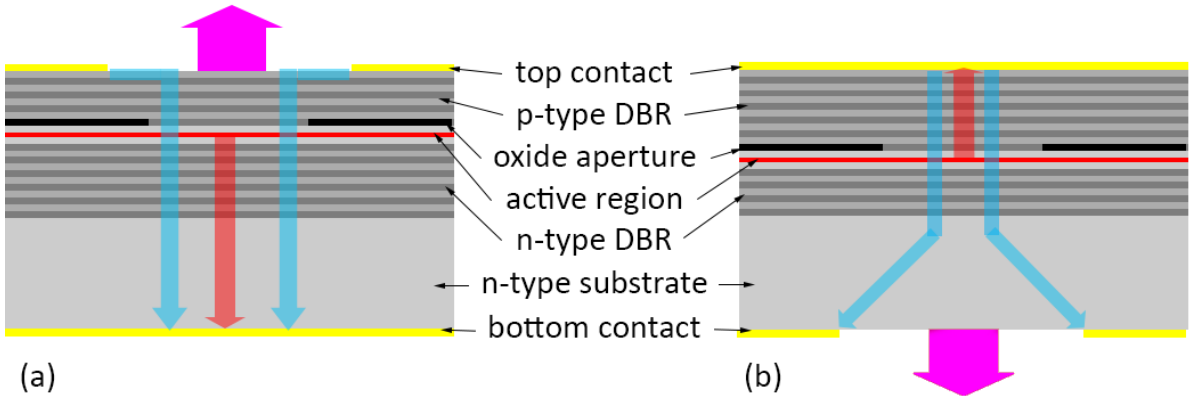

Figure 1.4: Cross sections of (a) top- and (b) bottom-emitting VCSELs. The blue and red arrows signify the paths of least resistance for current and heat, respectively, illustrating the superior current uniformity and decreased thermal resistance of bottom-emitting VCSELs.

1.1.2.2 High Power Single Mode VCSELs

While high output powers are necessary to achieve high radiance, single-mode operation is also critical towards achieving the small spot size, low divergence and

spectral purity necessary for many high-radiance applications. Small aperture diameters are necessary to maintain single fundamental mode output in individual VCSELs, however, which has limited the maximum single fundamental output power to <8 mW. This limitation remains despite numerous approaches by various research groups [35-41], as shown in Figure 1.5.

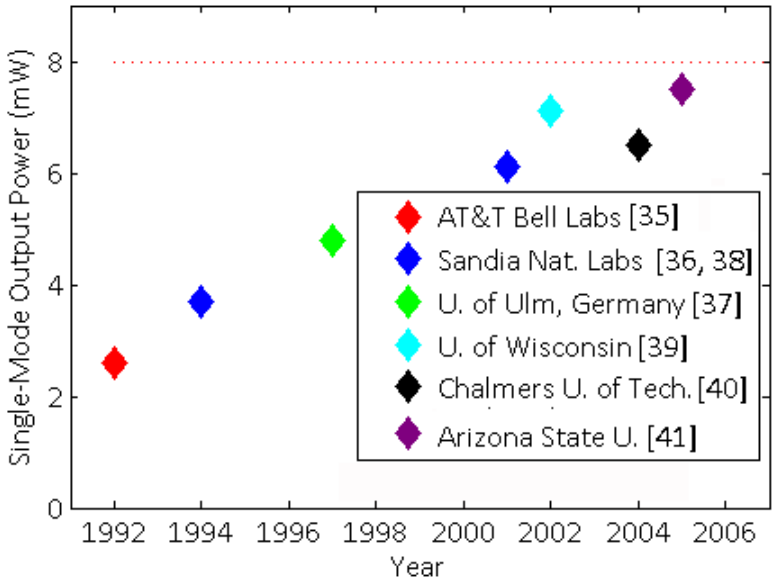

Figure 1.5: Maximum single fundamental mode output power from individual VCSELs achieved by various research groups and limited to less than 8 mW.

In light of the limitations of single fundamental mode VCSELs, VCSEL arrays were sought early on as a way to scale up power in a single higher order mode, or in a superposition of coupled modes (supermode). This is similar to the trend toward VCSEL arrays for high power, but coherent arrays offer distinct advantages over incoherent arrays, which are further detailed in Chapter 2. The advantages of coherent arrays come with much difficulty, however, because the array elements have to be coherently

coupled and the preferred mode has to be preferentially selected. A longstanding problem with this approach is that such arrays tend to operate in the out-of-phase supermode where nearest-neighbor elements are locked out-of-phase [42, 43], as predicted by theory [44]. This leads to an undesirable four-lobed far-field pattern with an on-axis intensity null. In-phase VCSEL arrays, which provide an on-axis intensity peak, have been obtained primarily with antiguided top-emitting arrays [45-47]. These types of arrays, as shown in the historical plot of Figure 1.6 [42, 43, 46-57], have been limited to a maximum power around 2 mW. This limitation is largely due to the difficulties of thermal management and current injection uniformity common to top-emitting arrays. These challenges, just like the challenges of high power VCSELs and VCSEL arrays, can be significantly mitigated with a bottom-emitting design.

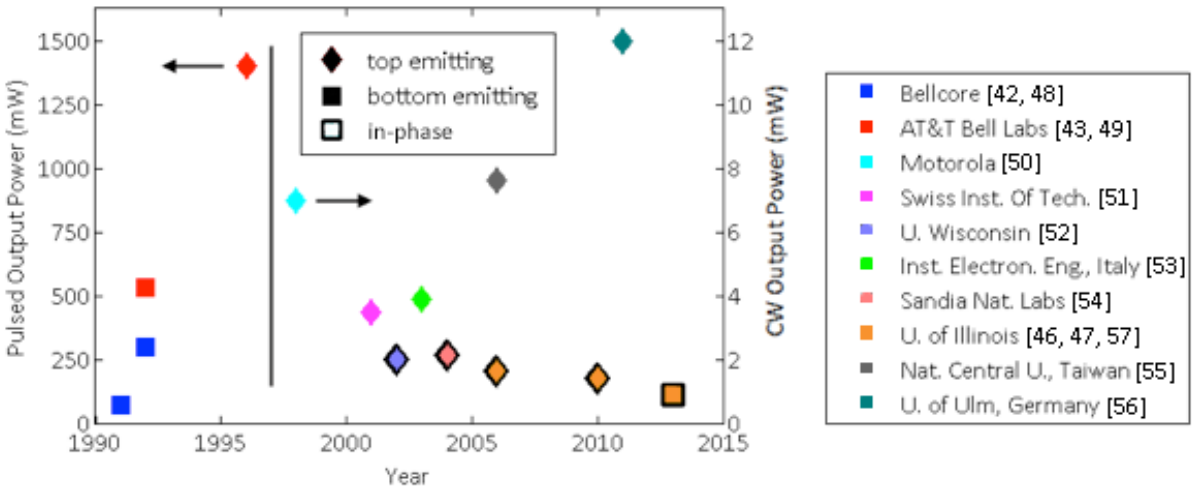

Figure 1.6: Maximum pulsed (before 1997) and CW (after 1997) output power obtained from phase-locked VCSEL arrays by various research groups.

1.1.3 Coupling

High-radiance arrays necessarily rely on coherence between array elements, which in turn requires optical coupling between them. The primary types of optical coupling used in diode laser arrays include injection-locking, diffraction, evanescent and antiguided (or leaky-mode) coupling [58]. The latter two are compared in Chapter 2.

It is instructive to first consider the historical development, following [59], of coherently-coupled edge-emitting laser arrays, which were heavily researched in the 1980s and early 1990s to scale up single-mode power. The first coupled edge emitting arrays relied on gain-guiding. The index profile in these devices was heavily dependent on drive current, which led to significant modal instability. The research moved on to arrays with built-in evanescent coupling, where the array elements were designed to have a larger refractive index than the spacing regions between elements. In these arrays, the light in each element is guided, and the coupling occurs between the evanescent tails of the electric field in neighboring elements. These structures were found to operate almost exclusively in the undesirable out-of-phase supermode, simply because it has better overlap with the gain/loss profile of these arrays. Another significant drawback of both evanescent and diffraction coupling schemes is that they typically rely on nearest neighbor coupling between elements. This type of coupling leads to decreased coherence between elements further separated in the array, which has the undesirable consequences of multimode operation and a broadened far-field

divergence. The maximum diffraction-limited power obtained from arrays of these three types is 200 mW, but the multi-lobed far field pattern due to the out-of-phase coupling significantly reduces their usefulness.

A significant breakthrough in coupled edge-emitting arrays came in 1988 with the incorporation of a built-in antiguided index profile [60]. This type of coupling allows strong, stable coupling between all elements of an array, and can preferentially support the preferred in-phase mode if properly designed. These advantages allowed antiguided edge-emitting arrays to demonstrate CW diffraction limited powers up to 500 mW in a single, in-phase mode [61, 62], which was far superior to that achieved with alternate coupling schemes. The output power of such edge-emitting arrays was eventually thermally limited, and various methods of beam combining have since been sought as an alternative approach to achieving high-radiance sources.

As previously stated, bottom-emitting VCSEL arrays have the potential to surpass these limitations due to advantages in 2D configurability and thermal management. Coupled VCSEL array development is currently in a state similar to that of coupled edge-emitting arrays in 1988, where they have achieved limited powers, typically in the undesirable out-of-phase operation [56]. In-phase emission has been achieved with built-in antiguiding [45], but with difficult re-growth fabrication processes and a thermally-limited output power of less than 2 mW [52]. The breakthrough in phased VCSEL arrays is likely to come from the combination of a bottom-emitting structure

allowing good thermal management and current uniformity with a strong, built-in antiguiding index profile to preferentially select the in-phase supermode. Previous bottom-emitting coherent arrays have employed reflectivity modulation and mesa etching, which led to out-of-phase operation [42, 43]. The first in-phase bottom-emitting VCSEL array is presented in this work. The array is dependent on an antiguided index profile that is created by a simple, self-aligned process. It represents a critical step toward coherent, high-radiance arrays.

1.2 Scope

In this work we examine phased VCSEL arrays designed for both beam steering and high radiance applications. The beam-steering arrays are designed in the top-emitting configuration. They have top contacts that are separated by a focused ion beam (FIB) etch to achieve current confinement between the array elements. In this way, the current injected into each element can be adjusted, which steers the beam in the far field. The high-radiance arrays have a bottom-emitting structure and are designed with a single contact for each array.

The analysis tools used for design and simulation, including the Fraunhofer propagation method and dynamic coupled mode theory, are first introduced in Chapter 2. The processing and experimental methods used are next presented in Chapter 3. Data from the top-emitting arrays is then presented and analyzed in

Chapter 4 with a primary goal of elucidating the physical beam-steering mechanism evident in the arrays. Results from the bottom-emitting array data are discussed in Chapter 5 and conclusions and future work are given in Chapter 6, followed by appendices and references.

CHAPTER 2: ANALYSIS TOOLS

2.1 Introduction

Various analysis tools used to design, model and characterize coherently coupled VCSEL arrays are presented. Different types of coherent coupling are first compared, based primarily on Refs. [58] and [59]. The Fraunhofer propagation method, which is used throughout this work to correlate the near and far field data, is discussed next [63]. Simulations of expected results based on the Fraunhofer propagation method are then presented. Finally, dynamic coupled mode theory, which has proven very capable of modeling various types of VCSEL arrays, is used to derive the connection between the native resonant frequencies of the element cavities and the temporal phase shift between them [64].

2.2 Coupling

Of the several typical types of coupling used in diode laser arrays, guided (evanescent) and antiguided coupling are the most prevalent and are both based on the refractive index profile of a given laser array. A comparison and contrast of these two coupling mechanisms thus provides a good theoretical foundation.

2.2.1 Guided and Antiguided Coupling

The guided and antiguided modes supported by a given index profile are illustrated in Figure 2.1(a-e). Coupled mode theory gives a good approximation for the guided solutions [65]. In this approach, the array elements are assumed to be coupled only to their nearest neighbor elements. In Figure 2.1, the in-phase (Figure 2.1b) and out-of-phase (Figure 2.1c) supermodes are shown for the index profile given in Figure 2.1a. The term *supermode* is used to denote the superposition of multiple, otherwise independently guided modes into a single overarching and coherent mode [65]. Laser arrays can operate in these supermodes with gain applied to the high-index regions. With very few and unstable exceptions [66], such evanescently-coupled arrays are found to operate in the out-of-phase supermode shown in Figure 2.1c, simply because it has better overlap with the required gain profile. Specifically, the electric field of the out-of-phase supermode has a zero crossing in the inter-element regions without gain, while the in-phase supermode of Figure 2.1c has a non-zero field in this region. Also of note, both guided supermodes are shown to fall within an encompassing envelope as shown by the dashed lines in Figure 2.1(b, c).

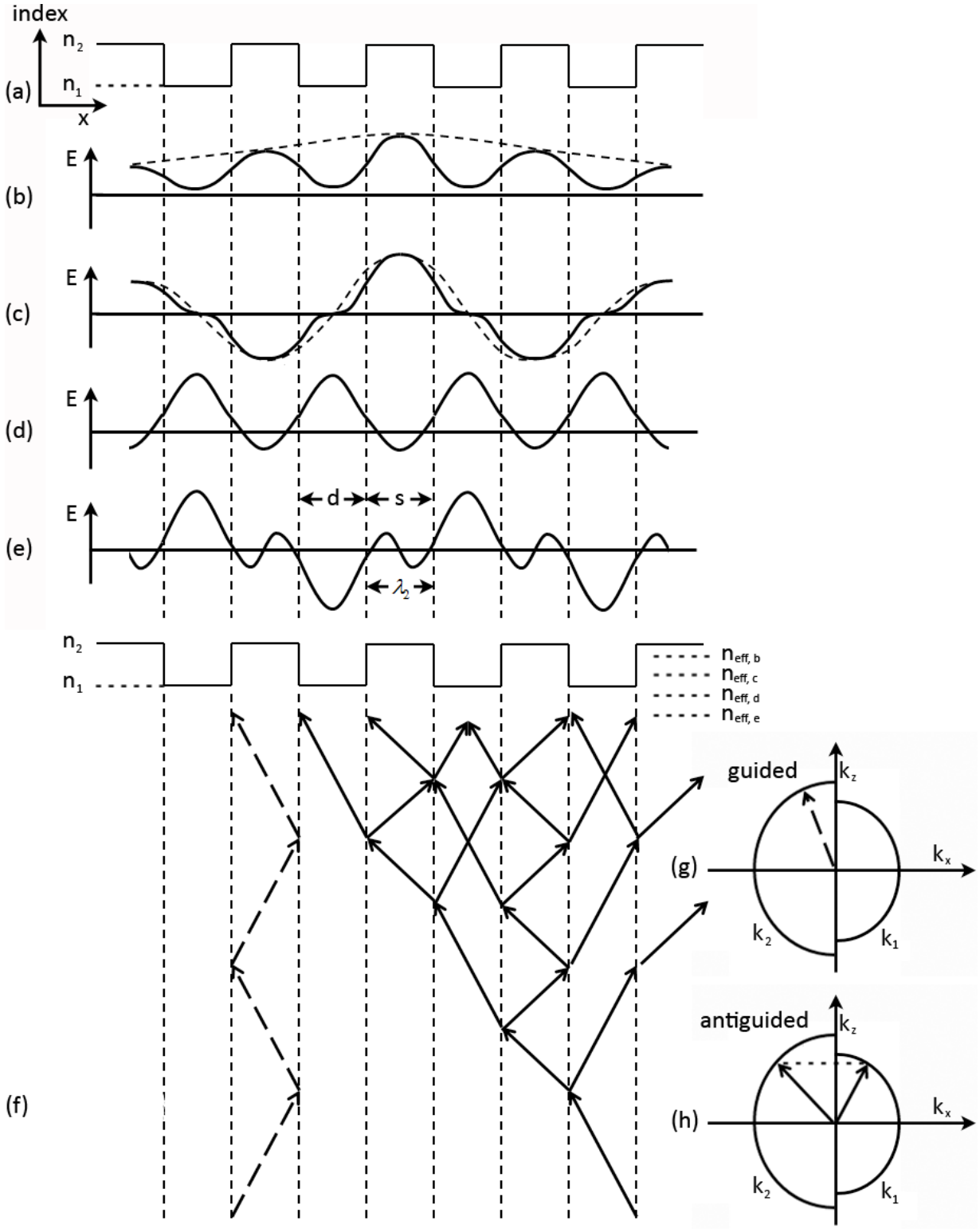

Figure 2.1: (a-e) Comparison of guided (evanescent coupling) and antiguided (leaky-mode) electric field modal profiles for the given index profile. (f) Ray optics representation of guided (dashed) and antiguided (solid) propagation and (g-h) associated k-diagrams. Figures (a-f) follow Ref. [62].

The antiguided modal profiles shown in Figure 2.1d (in-phase) and Figure 2.1e (out-of-phase) can be achieved with gain applied to the low-index regions. The solutions for the electric field profile are typically found using Bloch analysis [67] or a decomposed two-dimensional Helmholtz equation [44]. The antiguided modes are not necessarily subject to the overarching envelopes like the guided supermodes, and can support uniform intensities in all array elements, which is typically desirable.

The ray optics and k-diagram sketches of Figure 2.1(f-h) reveal more coupling differences. In a guided mode the beam is confined by total internal reflection, and there is only a decaying evanescent wave in the low-index regions. In this case the propagation constant is given by $\beta_{guided} = k_0 n_{eff} = k_{2\ z} > k_{1\ z}$, where k_0 is the free space wave vector and k_1 and k_2 are shown in Figure 2.1(g, h). This is also shown by the effective indices $n_{eff,\ b}$ and $n_{eff,\ c}$ in Figure 2.1f, which reside between n_1 and n_2. Alternatively, the antiguided beam only partially reflects at the index boundaries. The propagation constant is found as $\beta_{antiguided} = k_0 n_{eff} = k_{2\ z} = k_{1\ z} < k_1$. In this case, as shown in Figure 2.1f, $n_{eff,d}$ and $n_{eff,e}$ are less than n_1, and the wave is traveling rather than confined. The quantum mechanical analogy would be a bound particle inside a potential well (guided) versus a free particle above the well (antiguided).

While the beam transmission at the index boundaries can introduce edge radiation loss for antiguided arrays, it also affords them the significant advantage of

parallel coupling between all elements in an array. This advantage is more pronounced for larger arrays where weak, nearest-neighbor evanescent coupling leads to decreased coherence among separated elements. The edge radiation loss is also reduced in larger antiguided arrays because only the edge elements leak outwardly. Further, it can be eliminated entirely by incorporating an index guide, such as a photonic crystal cladding, around the perimeter of the array [46, 68]. Antiguiding is therefore more advantageous for larger arrays.

Another primary difference between the two types of coupling is that while evanescent coupling typically leads to the out-of-phase supermode, the preferred mode in antiguided arrays is largely determined by the interelement spacing. The traveling wave in the interelement region has a wavelength, λ_2, as shown in Figure 2.1e, which is based on the index contrast between n_1 and n_2 and on the element width, d [44, 69]. A lateral resonance of the preferred in-phase mode can thus be achieved by varying the interelement separation to $s = m\lambda_1 / 2$, where the array elements are resonantly in-phase for odd values of m. Another method commonly used to suppress the undesirable out-of-phase and adjacent modes in antiguided arrays is to introduce loss in the interelement regions [70].

2.2.2 Summary

To summarize the differences between guided and antiguided arrays, the latter can have the primary disadvantage of edge radiation loss. The primary advantages of

antiguided arrays are the strong, parallel coupling between all elements and the ability to preferentially select the in-phase mode by controlling the interelement spacing and loss. Other advantages of antiguiding include the uniform intensity profiles achievable for the array elements and the ability to build in a large, stable index contrast without allowing higher order modes within the element regions.

2.3 Fraunhofer Propagation Method

The beam properties at the VCSEL array facet must first be understood in order to determine the beam steering mechanism within the array. We can obtain near-field images of the optical mode, but this only provides intensity data. The relative phase of array elements has been retrieved previously by applying antenna array theory to the angular position of the far-field peaks and nulls [71]. The Fraunhofer propagation method described herein, alternatively, takes into account both the near and far fields, and is much less subject to error [63].

The Fraunhofer approximation is a simplified analysis tool for translating a beam from the near to far field as denoted by the $\xi\eta$ and xy planes, respectively, in Figure 2.2. It is fundamentally based on the Helmholtz equation and free-space Green's theorem [72]. The first necessary approximation is to restrict the near-field contribution to the area defined by the aperture Σ, as in Figure 2.2. The field amplitude at point P_1 in the far field, $U(x_1, y_1)$, can then be found as the combination of the field transmitted

from each point, P_0, in the near field. Further necessary assumptions include $\sqrt{\Sigma} \gg \lambda_0$, $\left|\overrightarrow{r_{01}}\right| \gg \lambda_0$, $\sin\theta \gg 1$ and a monochromatic wave front, where λ_0 is the free-space wavelength, $\overrightarrow{r_{01}}$ is the vector from P_0 to P_1, and θ is the off-axis angle of $\overrightarrow{r_{01}}$ as defined in Figure 2.2. The Fraunhofer approximation can then be found as

$$U(x,y) = \frac{e^{jk_0 z}}{j\lambda z} e^{j\frac{k_0}{2z}(x^2+y^2)} \int_{-\infty}^{\infty}\int U(\xi,\eta) e^{j\frac{2\pi}{\lambda z}(x\xi+y\eta)} d\xi d\eta \ , \tag{2.1}$$

where k_0 is the free space wave vector and $U(\xi,\eta)$ is the near-field amplitude. This approximation conveniently lends itself to a 2D Fourier transform, which can be speedily calculated.

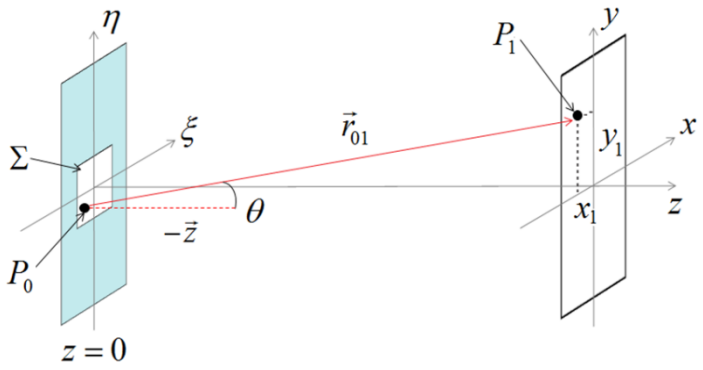

Figure 2.2: Schematic of variables used in the Fraunhofer approximation.

2.3.1 Phase and Coherence Retrieval

The Fraunhofer approximation can also be used to calculate the far fields resulting from multiple near-field apertures. We begin by defining the apertures of a two-element in-phase array, as these are the most commonly characterized in this work. We define left (1), right (2) and middle near-field apertures, where the middle aperture

encompasses the small fringe found in the interelement region. These sections are delineated by the dashed lines in Figure 2.3a where a 1D Helmholtz solution to the shown antiguided index profile shown is found by a finite difference method [73]. If we assumed the three elements were incoherent with each other, the total far field intensity, $I(x,y)_{incoh}$, is found as the combination of the far field intensities of each of the individual apertures

$$I(x,y)_{incoh} = \left|U_1(x,y)\right|^2 + \left|U_{mid}(x,y)\right|^2 + \left|U_2(x,y)\right|^2 \ , \tag{2.2}$$

where the individual far field amplitudes are calculated from their corresponding near-field amplitudes per Equation 2.1, and the phase terms are left out because they have no effect.

If the elements are assumed to be coherent with each other, we can meaningfully assign a relative phase to the middle and right apertures, Φ_{mid} and Φ_2, respectively, with the left aperture phase arbitrarily set to zero. The total far field intensity can then be calculated by the summation of the fields as

$$I(x,y)_{coh} = \left(\left|U_1(x,y)\right| + \left|U_{mid}(x,y)\right|e^{-i\Phi_{mid}} + \left|U_2(x,y)\right|e^{-i\Phi_2}\right)^2 . \tag{2.3}$$

In order to account for partial coherence between the near-field apertures we assign a normalized coherence magnitude, $|\gamma|$, where $0 \le |\gamma| \le 1$, to obtain

$$I(x,y) = |\gamma| I_{coh}(x,y) + (1-|\gamma|) I_{incoh}(x,y), \tag{2.4}$$

which can be expanded to yield

$$I(x,y) = |\gamma|\left(|U_1(x,y)| + |U_{mid}(x,y)|e^{-i\Phi_{mid}} + |U_2(x,y)|e^{-i\Phi_2}\right)^2 + (1-|\gamma|)\left(|U_1(x,y)|^2 + |U_{mid}(x,y)|^2 + |U_2(x,y)|^2\right) \quad (2.5)$$

Experimentally, we are able to determine the intensities $I(\xi,\eta)$ and $I(x,y)$. From $I(\xi,\eta)$ we can directly determine $|U_1(x,y)|$, $|U_{mid}(x,y)|$ and $|U_2(x,y)|$. For an in-phase array, the phase of the middle aperture is assumed to be π out of phase with the average phase of the two outer apertures, or

$$\Phi_{mid} = \pi + \frac{(\Phi_2 + \Phi_1)}{2} = \pi + \frac{1}{2}\Phi_2 . \quad (2.6)$$

This leaves us with two unknown values, $|\gamma|$ and Φ_2, for connecting the experimentally-determined near and far field intensities. These can be extracted independently because $|\gamma|$ determines the visibility of the far-field lobes, while Φ_2 determines the relative far-field peak intensities and their angular location [71]. Equation 2.5 is thus used in an iterative manner in Chapter 4 to retrieve the relative phase and coherence between elements from the experimentally-acquired near and far field intensities [63]. Its application is also described for a one-dimensional simulation in the next section. The MATLAB code used for the Fraunhofer propagation is given in Appendix A.

2.3.2 Simulations

The three near-field sections delineated in Figure 2.3a are propagated to the far field using a one-dimensional variation of Equation 2.5. The far field profiles are shown in Figure 2.3b and Figure 2.3c, as obtained from varying values of $|\gamma|$ and Φ_2. The far field profile is found to exhibit more pronounced peaks and nulls with increased coherence and to shift in angle and shape with varied relative phase.

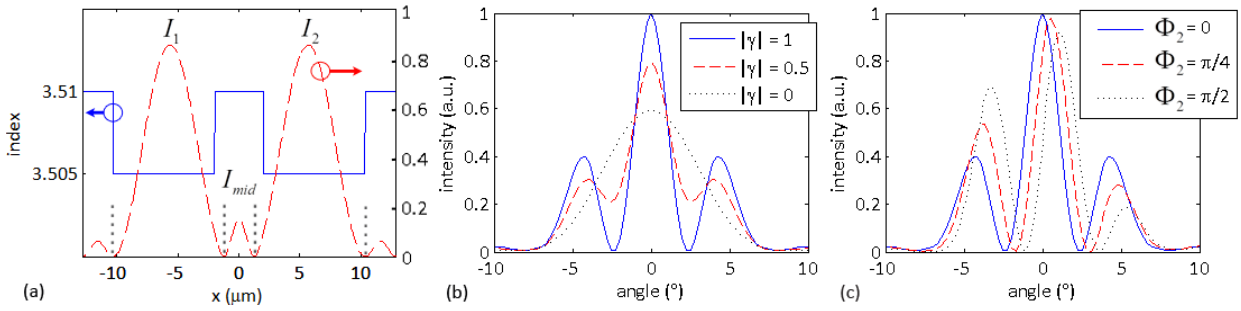

Figure 2.3: (a) Near-field intensity profile obtained from 1D Helmholtz finite difference simulation for an antiguided index profile with λ_0 = 980 nm. (b) Far-field intensity profile obtained with Fraunhofer propagation method of (a) for $\Phi_{mid} = \pi$, $\Phi_2 = 0$ and different values of $|\gamma|$. (c) Far-field intensity profile for $|\gamma| = 1$ and different values of Φ_{mid} and Φ_2.

A rigorous approach for finding the two-dimensional near field for a given two-dimensional index profile would be to extend the one-dimensional Helmholtz solver used above into two dimensions [44]. A simpler approach used in the following simulations is to assume Gaussian, coherent beams of equal magnitude emanating from each array element. In Figure 2.4, we show the simulated impact of the number of elements, N, on the far field. In going from one element to the four elements shown in Figure 2.4a, the far field divergence in Figure 2.4b is shown to decrease while the on-

axis intensity peak shown in Figure 2.4(c and d) scales up by 16 x, or N^2. If the elements were incoherent, the far field intensity peak would only scale up by 4 x, or N. This is the primary advantage of coherent arrays for high brightness applications, and is a consequence of the electric fields from coherently-coupled elements adding, while only the intensities add for incoherent elements.

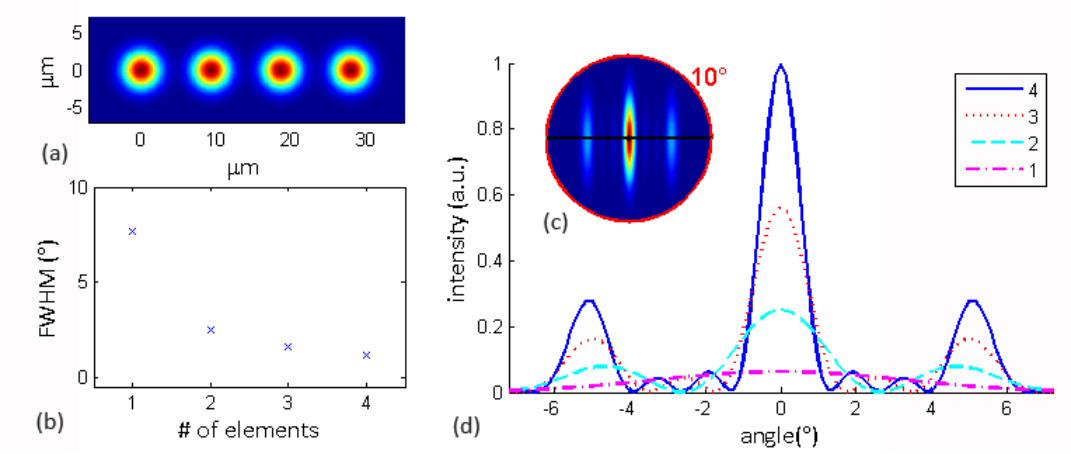

Figure 2.4: Simulated impact of number of elements on far field profile. (a) Near-field and (c) corresponding far-field image for four coherent, Gaussian, in-phase elements. (d) Far field profiles and (b) full width half maximums (FWHMs) for varying numbers of elements.

Steering resolution, defined as the number of distinguishable far-field spot counts, is an important metric for many beam steering applications. It is obtained as the ratio of the maximum steering angle, θ_{max}, to the beam's FWHM [74]. For the four-element array depicted in Figure 2.5a we find a θ_{max} of 5° as the angular gap between the far field lobes when the array is operating in the out-of-phase mode. If the relative phase between elements is properly adjusted, as in Figure 2.5b, the beam peak can be steered within that range. This is shown by the far-field modal profiles of corresponding colors

in Figure 2.5d, which are taken from slices across the line shown in Figure 2.5c. For this four-element array the FWHM is found to be 1.2°, yielding a steering resolution of 4.2. While θ_{max} is the same for a two-element array of the same element pitch, the FWHM is 2.43°, yielding a steering resolution of 2.1. It is thus found that increasing the number of elements increases the steering resolution. Increasing the beam steering range would require decreasing the separation between elements.

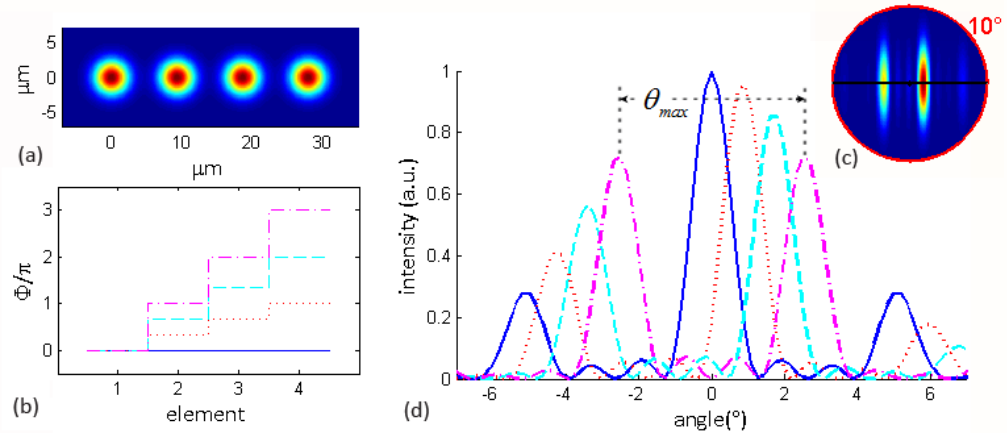

Figure 2.5: Simulated impact of element phase on far field profile. (a) Near field and (c) corresponding far field image for phase profile defined by dashed cyan line in (b). (d) Resultant far-field profiles from phase profiles in (b) per corresponding line styles and colors.

Two-dimensional patterns of 4x4 and cross-shaped arrays are lastly examined in Figure 2.6. The elements defined in the 4x4 array shown Figure 2.6a are self-coherent but mutually-incoherent, and are thus found to yield a much larger far field divergence in Figure 2.6b than the mutually-coherent 4x4 array of Figure 2.6c is found to yield in Figure 2.6d. Figure 2.6e shows an out-of-phase 4x4 array, which is common in evanescently-coupled and reflectivity-modulated VCSEL arrays. The resulting and undesirable, but often encountered four-lobe profile is shown in Figure 2.6f. Finally, the

cross-shaped in-phase near field of Figure 2.6g is shown to give the expected on-axis intensity peak in Figure 2.6h. If the middle element is π out of phase, as in Figure 2.6i, the on-axis intensity in Figure 2.6j is overshadowed by the four outer lobes. It is thus observed that if even a single element out of five is out-of-phase, it can have a very significant effect on the far field pattern.

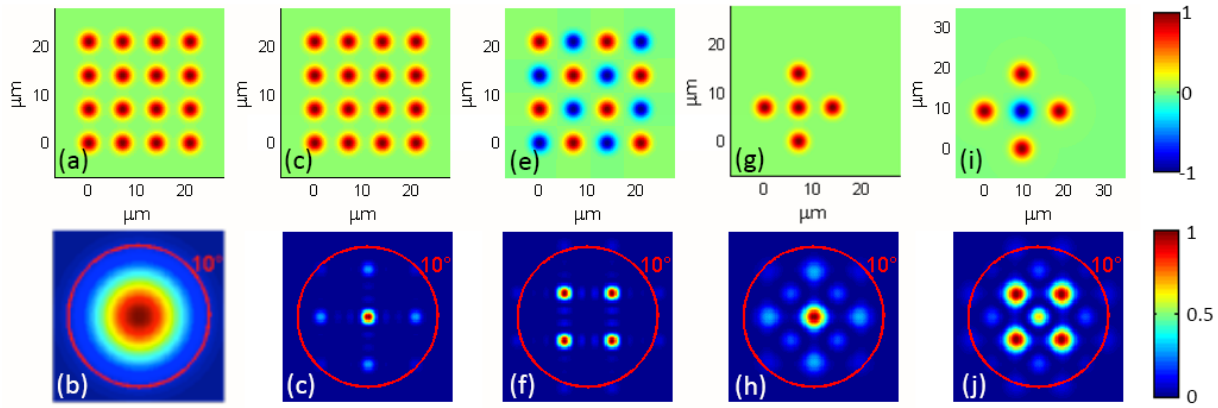

Figure 2.6: Near and far field patterns for (a, b) 4x4 mutually incoherent, (c, d) 4x4 mutually coherent in-phase, (e, f) mutually-coherent out-of-phase and (g, h) in-phase and (i, j) out-of-phase cross-shaped arrays.

2.4 Dynamic Coupled Mode Theory

The most suitable approach for examining the dynamics of antiguided VCSEL arrays is to treat the array as a single entity [75]. Coupled mode theory, alternatively, is only strictly valid for structures where the modes of individual lasing elements are well confined, as in guided coupling. The theory is highly developed though, and has been successfully applied to coupled [42, 76] and injection-locked [25, 77] VCSEL arrays. The assumption of nearest-neighbor coupling with coupled mode theory is also justified for a two-element antiguided array. Coupled mode theory is therefore examined as a

means to explain the phase shifting mechanism observed in two-element phased VCSEL arrays. A more detailed version of the following derivation is provided in Appendix B.

The electric field of element m is defined as $E_m = A_m e^{-i\Phi_m(t)}$, where A_m is the field amplitude and Φ_m is the phase. The time change of the electric field under the influence of neighboring elements, E_{m-1} and E_{m+1}, is governed by the field equation [78]

$$\frac{dE_m}{dt} = \frac{1}{2}\left[G(N_m) - \frac{1}{\tau_p} \right](1 - i\alpha)E_m + i\kappa\left(E_{m+1} + E_{m-1}\right)e^{-i\psi} + i(\omega_0 - \omega_m)E_m, \qquad (2.7)$$

where G is the gain, N is the carrier density, τ_p is the photon lifetime, α is the linewidth enhancement factor, κ is the coupling strength between elements, ψ is the coupling phase (typically 0 or π), ω_0 is the coupling frequency and ω_m is the native frequency of element m. If the laser element is operating near threshold, the gain can be expressed as

$$G(N_m) = G(N_{th}) + g(N_m - N_{th}), \qquad (2.8)$$

where N_{th} is the threshold carrier density and g is the differential gain. With the threshold gain defined as that required to overcome the loss, or $G(N_{th}) = 1/\tau_p$, Equation 2.7 can be expressed as

$$\frac{dE_m}{dt} = \frac{1}{2}\left[g(N_m - N_{th}) \right](1 - i\alpha)E_m + i\kappa\left(E_{m+1} + E_{m-1}\right)e^{-i\psi} + i(\omega_0 - \omega_m)E_m. \qquad (2.9)$$

This can then be transformed into the dimensionless equations [79]

$$\frac{dX_m(t)}{dt} = Z_m X_m - \eta\left[X_{m+1}\sin\left(\phi_m - \Phi_{m+1} - \psi\right) - X_{m-1}\sin\left(\Phi_m - \Phi_{m-1} - \psi\right)\right] \quad (2.10)$$

$$\frac{d\Phi_m(t)}{dt} = \alpha Z_m - \eta\left[\left(X_{m+1}/X_m\right)\cos\left(\Phi_m - \Phi_{m+1} - \psi\right) + \left(X_{m-1}/X_m\right)\cos\left(\Phi_m - \Phi_{m-1} - \psi\right)\right] + \Delta_m, \quad (2.11)$$

where X_m, Φ_m and Z_m are the normalized magnitude, phase and excess carrier density in element m. The following variables are used in the transformation:

$$\begin{aligned} X_m &= \left(\frac{1}{2}g\tau_s\right)^{\frac{1}{2}}\left|E_m\right|, \\ Z_m &= \frac{1}{2}gN_{th}\tau_p\left(\frac{N_m}{N_{th}} - 1\right), \\ \eta &= K\tau_p, \text{ and} \\ \Delta_m &= \left(\omega_0 - \omega_m\right)\tau_p. \end{aligned} \quad (2.12)$$

For a two-element array, Equations 2.10 and 2.11 can be shown to yield

$$\omega_2 - \omega_1 = -\kappa\left(\alpha\left(\frac{X_1}{X_2} + \frac{X_2}{X_1}\right)\sin\left(\Phi_1 - \Phi_2 - \psi\right) + \left(\frac{X_1}{X_2} - \frac{X_2}{X_1}\right)\cos\left(\Phi_1 - \Phi_2 - \psi\right)\right). \quad (2.13)$$

The difference in the native resonant frequencies of the elements, as found on the left side of Equation 2.13, can be controlled by differential current injection into the VCSEL array elements. This frequency difference is thus found to govern the phase shift between elements, with some additional correlation to the relative amplitudes of the elements. The phase shift, in turn, determines the far-field steering angle.

2.4.1 Pendulum Analogy

An intuitive understanding of the commonly-encountered spatial phase shifting mechanism illustrated in Figure 1.1a is straightforward. While Equation 2.13 gives a clear theoretical connection between the resonant frequency detuning between elements and the resultant temporal phase shift, an intuitive understanding of this connection is less obvious. An analogy is attempted to bridge this gap and to further rationalize the application of coupled mode theory.

The self-coherent emission from two independent cavities can be viewed as two independent pendulums, each having its own natural resonant frequency, as in Figure 2.7a. If the pendulums are coupled together by a weak spring as in Figure 2.7b, and their resonant frequencies are the same, the spring will act to lock the pendulums into either a similar or opposite oscillation pattern (in-phase or out-of-phase). If the length of the right pendulum is slightly increased so that its resonant frequency is slightly decreased, the spring will continue to hold the pendulums to a compromised frequency. The dynamics will change though, as the left pendulum will want to pull the right pendulum along at a faster rate, while the right pendulum will resist. The pendulums will therefore maintain the same rate of oscillation, but the right pendulum will temporally lag the oscillation of the left, as in Figure 2.7b. Further, if the weight of the right pendulum is increased, the compromised frequency will shift closer to that of the right pendulum because of the right pendulum's increased relative influence.

Finally, if the length of the right pendulum is increased further, the spring will no longer be able to harmonize the two oscillation rates, and the pendulums will swing independently. These observations are found to be consistent with both Equation 2.13 and with the experimentally-observed phase shifting, coupling frequency and locking range for coherently-coupled VCSEL arrays, as detailed in Chapter 4.

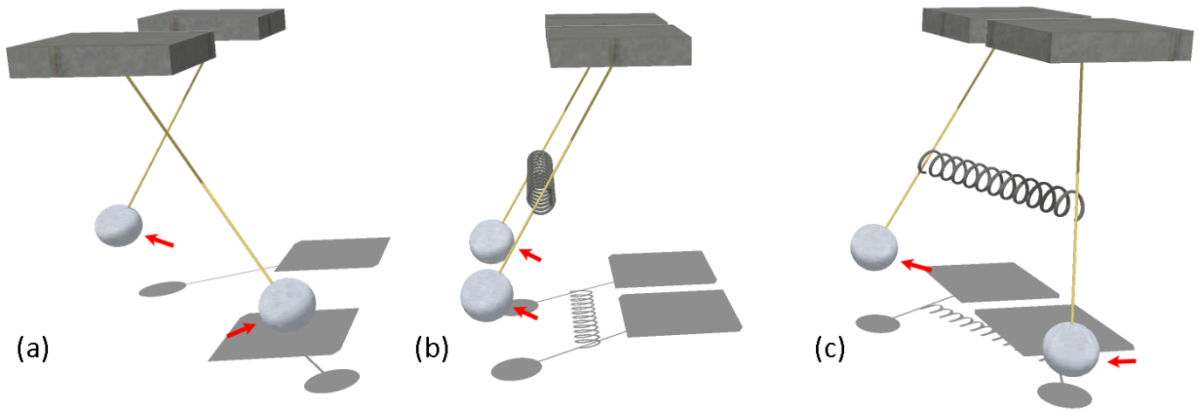

Figure 2.7: Two pendulums (a) uncoupled, (b) coupled in-phase, and (c) coupled in-phase with the foremost pendulum having a decreased native resonant frequency.

2.5 Summary

The coupling theory covered in this chapter is useful for understanding the interaction between array elements and for device design. The Fraunhofer propagation method is used frequently throughout this work as a means to test and validate our understanding of the arrays, and to retrieve the relative phase and coherence of the emitted beam at both the array elements and in the interelement regions. The dynamic coupled mode theory presented will be used to examine the correlation between the native element frequencies and the relative phases of the elements.

Chapter 3: METHODS

3.1 Introduction

The top- and bottom-emitting coherently-coupled VCSEL array designs are first presented. Two critical fabrication steps are then described. First, details of the focused ion beam (FIB) etching process used for both top- and bottom-emitting arrays are presented. The thick patterned metal deposition process used for the bottom-emitting arrays is discussed next. Lastly, the various experimental setups for optical characterization are presented.

3.2 Array Structure

The two primary array structures examined are shown in Figure 3.1 and Figure 3.2. The top-emitting structure is shown by the sketch of Figure 3.1a and SEM image of Figure 3.1b. It consists of a p-type top DBR mirror with 27 periods and an n-type bottom DBR mirror with 35 periods on an n-type GaAs substrate. The active region located between the mirrors consists of three GaAs quantum wells with photoluminescence centered near 850 nm. The photonic crystal hole pattern is designed to optically confine the mode within the defects. These defects are aligned with gain apertures defined by surrounding ion implantation to confine current to the individual elements. The fabrication process is described in previous work [66, 68]. For the work in this thesis, the top metal contact is etched with a focused ion beam in an additional step [63].

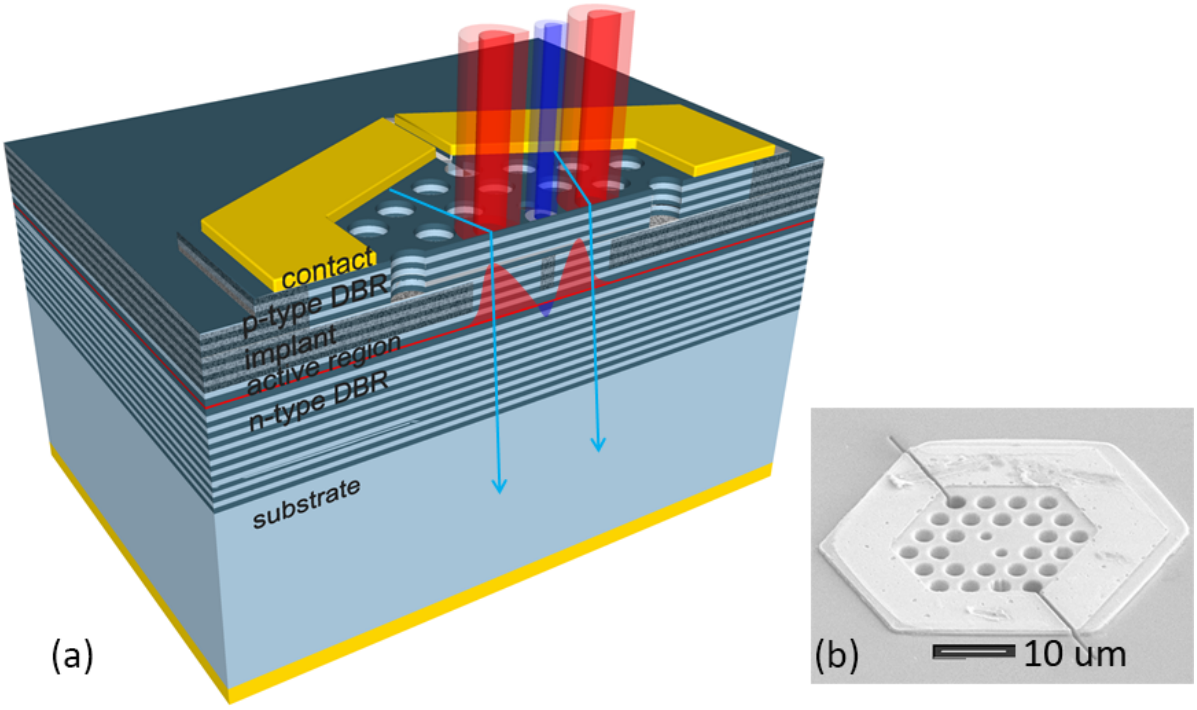

Figure 3.1: (a) Sketch and (b) SEM image of top-emitting VCSEL array structures. Sketch shows preferred current path from either contact and preferred in-phase modal profile and beam.

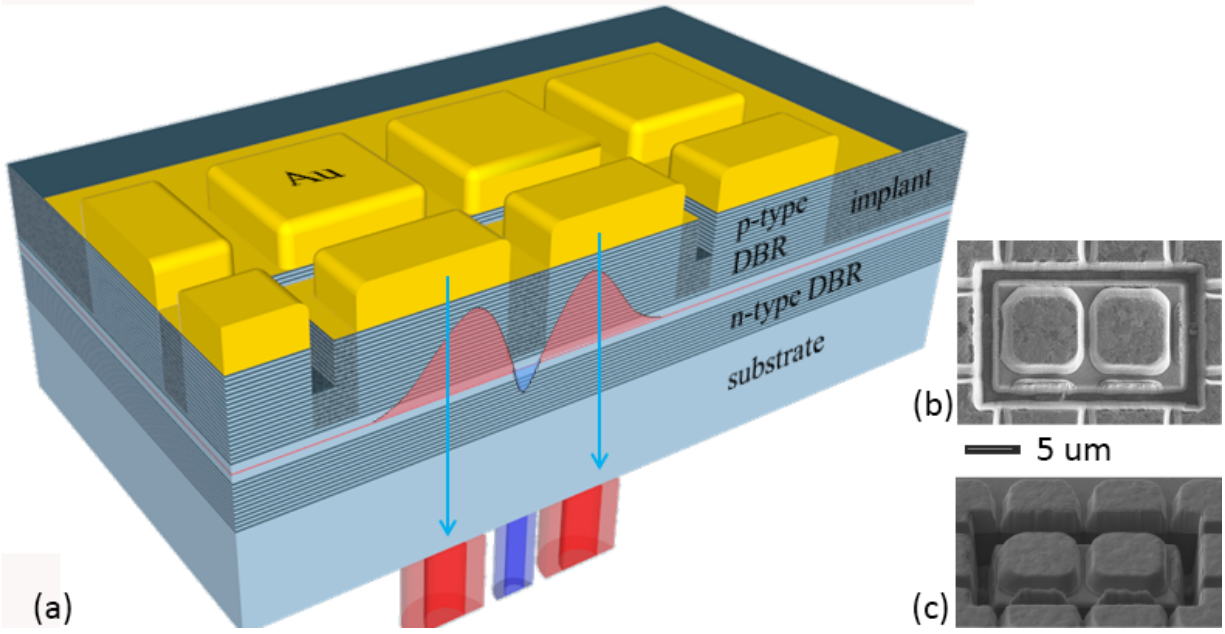

Figure 3.2: (a) Sketch, (b) ion beam image and (c) SEM image of bottom-emitting array.

The bottom-emitting array is shown by a sketch in Figure 3.2a, a top-view ion beam image in Figure 3.2b and an SEM image in Figure 3.2c. It consists of a 29-period n-type

output DBR on top of an n-type substrate. The active region emits nominally at 980 nm. The top, high-reflectivity p-type DBR consists of 32 periods. An array of 3-μm thick, 6x6 μm^2 gold pillars are deposited by an electroplating process to define both the ohmic contact and to serve as a mask for ion implantation. After thinning the substrate, an electrode pattern (not shown) was deposited on the polished substrate around the array perimeter. The array sizes are delineated by a FIB etch into the high-reflectivity DBR. In both array types the refractive index is suppressed in the regions of highest carrier density, which serves to create the desired antiguiding index profile leading to in-phase operation.

3.3 Focused Ion Beam Etch

While the ion implantation is performed to achieve current confinement within the designed apertures, an additional focused ion beam etch is often necessary [81]. The latter is used for beam-steering arrays to allow increased current-injection discrimination between elements, and is performed in the bottom-emitting structures to define the arrays. Similar trends were noticed with both sample types. Etching too deep typically inhibits device operation, likely due to the detrimental effects of non-radiative recombination centers created from Ga^+ ion etching (and implanting) into the active region. Etching too shallowly, on the other hand, would often not provide noticeable current confinement. This is likely due to injected current traveling across

the DBR layers near the VCSEL surface, which have increased doping and therefore increased conductivity, thus limiting electrical isolation.

Various shapes, sizes and depths were FIB etched as a post-fabrication processing step. Good results were obtained from top-emitting and bottom-emitting 2x1 arrays, such as those shown in Figure 3.1b and Figure 3.2c. The FIB etch on the top-emitting array of Figure 3.1b was done with two 0.5 x 20 μm^2 lines etched simultaneously at 1000 pA for 10 seconds. The etch on the bottom-emitting array of Figure 3.2c was performed on a 2 x 75 μm^2 perimeter at 7000 pA for 90 seconds. The bottom-emitting array etch required higher ion beam current in order to penetrate through the thick gold layers.

One difficulty encountered with the FIB process was that while viewing the sample with the ion beam is necessary to achieve good alignment for etching, even the lowest ion beam currents were found to damage the surface, reducing its conductivity. This is particularly disruptive for top-emitting VCSELs that rely on current traveling from the contact through the highly doped top DBR layers to the element apertures, as in Figure 3.1a. The increased resistance causes increased heating, which degrades device performance.

The results from a study performed on this effect are shown in Figure 3.3. Multiple 2x2 arrays, such as shown in the inset of Figure 3.3, are exposed to varying Ga^+ ion implant doses. The resistance between the neighboring metal contacts labeled in the

inset of Figure 3.3c is shown to increase with the Ga^+ implant dose until eventually saturating. The effect is visible in the discoloration of the image inset in Figure 3.3c, which was exposed to the highest dose of 5000 pA·s/μm^2. Even a very small ion beam current of 10 pA is shown to increase the lateral resistance by 500 Ω if a typical image size of 5000x zoom is viewed for 10 seconds. While often detrimental, this effect can also have beneficial applications for beam steering with bottom-emitting VCSEL arrays. The Ga^+ ions penetrate approximately 50 nm into the epitaxial material, and the highly-doped top epitaxial layer for the bottom-emitting samples is only 40 nm thick. A relatively small Ga^+ ion implant dose could therefore significantly improve the current confinement between array elements without causing the undesirable optical effects of etching, and the thick gold pillars would block the ions from damaging the ohmic contacts to the individual elements.

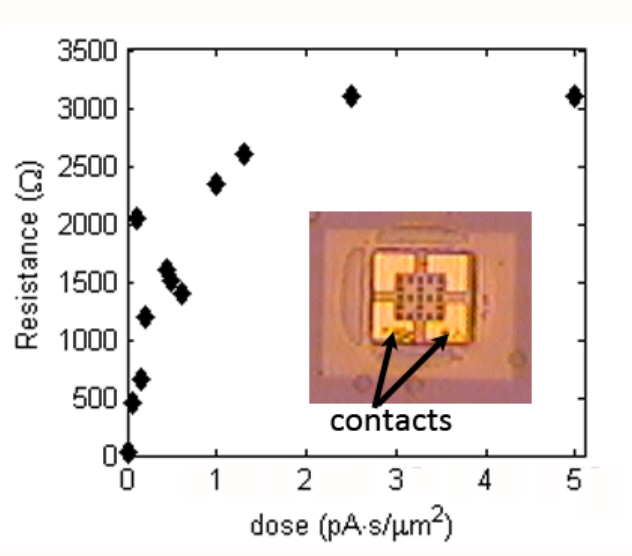

Figure 3.3: Resistance between top metal contacts increases with ion implant beam exposure.

3.4 Thick Metal Deposition

Bottom-emitting VCSELs have their high reflectivity mirror on the top side of the wafer, as in Figure 3.2a, which requires a greater number of DBR pairs. The bottom-emitting VCSELs under study have a 980 nm emission wavelength to allow transmission through the GaAs substrate. This larger number of periods and longer wavelength lead to an increased thickness from the top epitaxial layer to the active region in the bottom-emitting arrays, requiring a different approach for the masking process of ion implantation.

The ion implantation process for the top-emitting VCSELs uses a 6-µm thick photoresist mask layer [80]. The thickness is necessary to block the high energy ion implantation. This makes the process difficult because the implant diameters and separations are on the order of 5 and 1-2 µm, respectively, leading to precariously high pillars of photoresist over the desired apertures. Two different processes have since been used for the bottom-emitting designs, both relying on a thick metal layer consisting primarily of gold as an ion implantation mask. The advantage of this approach is that the gold has a greater stopping power, and therefore only needs to be 2.7 µm thick to block the largest necessary ion implantation energy of 470 keV.

The first successful approach to achieving a thick ion implantation mask was to use a gold electroplating process. The process was previously performed at nLIGHT Corp. and a scanning electron microscope (SEM) image of the resulting gold pillars is shown in

Figure 3.4a. A different approach pursued at the University of Illinois is to perform the standard liftoff procedure using a thick photoresist (AZ9260) mask. The photoresist and resulting gold deposition are shown in Figure 3.4b and Figure 3.4c, respectively, where an edge wall surrounding the gold pillars is evident.

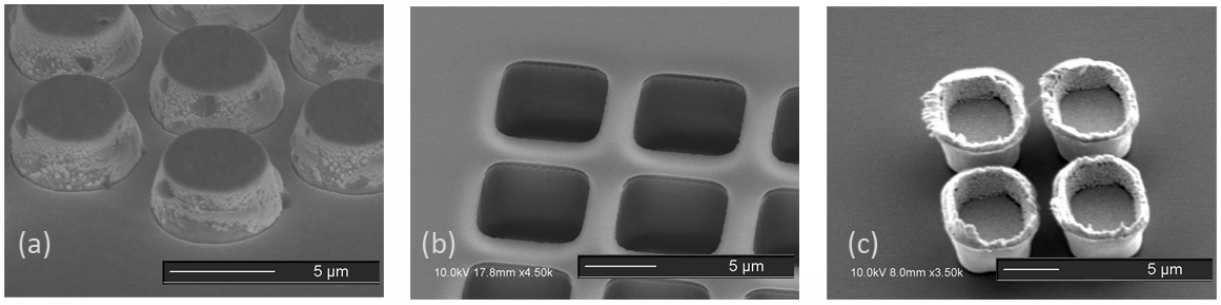

Figure 3.4: SEM images of ion implantation mask structures. (a) Gold pillars created by electroplating process. (b) Holes etched in AZ9260 photoresist for gold liftoff process. (c) Gold pillars created by liftoff process.

3.5 Optical Characterization Setup

Various experimental setups were used in characterizing the devices. Near field, far field, spectra, power and dynamic-beam-steering data were acquired. The most common setup is shown in Figure 3.5, and is used to acquire near-field images and spectral data simultaneously with a beam splitter. Two current sources are needed for beam steering arrays with separate injection into each element [63].

A similar approach used for obtaining spatially-resolved spectra is shown in Figure 3.6. Here a focusing lens is removed so the near field is imaged to a plane

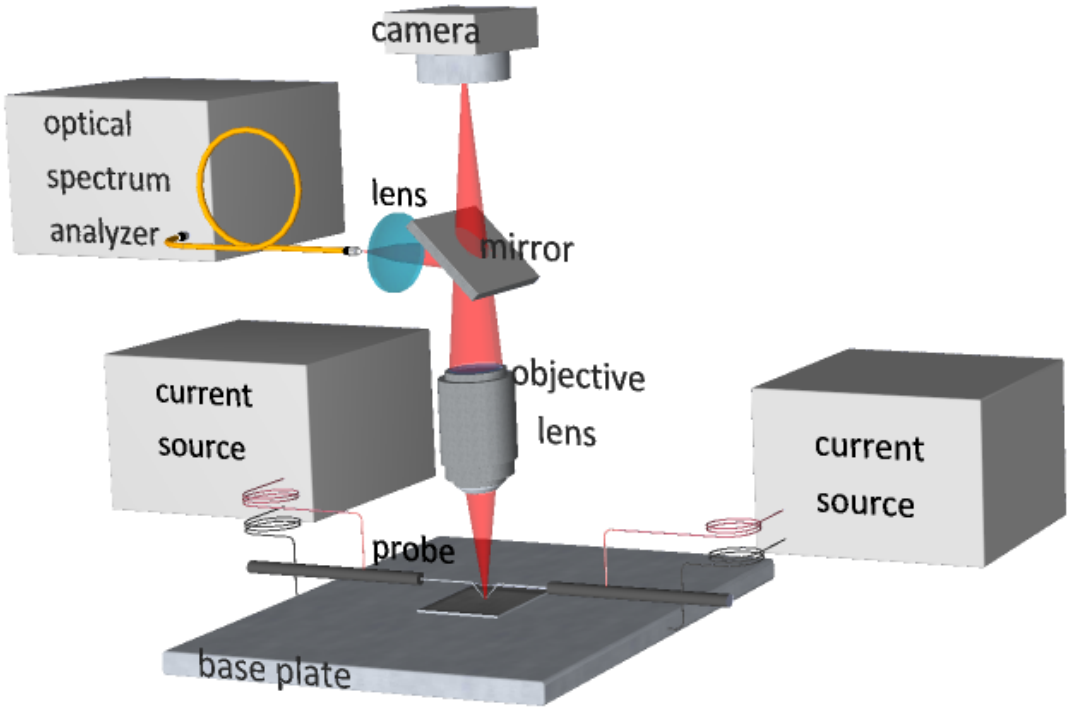

Figure 3.5: Experimental setup for acquiring near-field and spectral data.

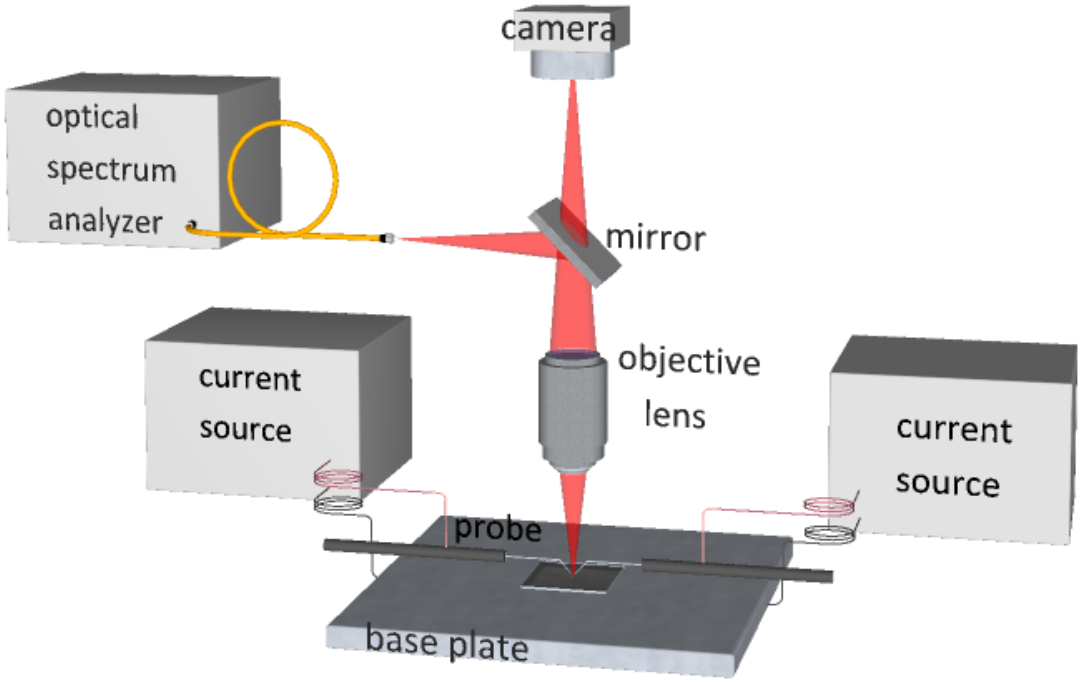

Figure 3.6: Experimental setup for acquiring spatially-resolved spectra.

coinciding with the fiber facet. If a 10x objective lens is used, for example, a multimode fiber with a 62.5 μm diameter core would collect the spectrum from a 6.25 μm diameter circle in the near field. The fiber is aligned to a particular spot in the near field by maximizing the power collected from a single lasing element. The objective lens, beam splitter, camera and fiber are then moved in unison to collect the spectrum from different portions of the near field.

The experimental setup is also configured to collect far field data from a goniometric radiometer as shown in Figures 3.7 and 3.8b. Not shown is a similar setup replacing the radiometer with a photodetector for optical power measurements. The setup was designed to allow seamless transition to/from that of Figure 3.5. This permits consistency in the probe position on the sample among other variables, which facilitates consistent near and far-field measurements.

The radiometer acquires intensity from 3241 data points in the direction of θ, as defined in Figure 3.7, and is incrementally rotated along ϕ to collect a full two-dimensional image. If the radiometer is placed sufficiently high above the sample (18 cm) the beam will subtend a ± 10° angle along the θ direction, allowing for an angular resolution as high as 0.006°. The goniometer was most recently calibrated in November of 2012 to ensure intensity readings within a ± 2% range of a standard reference source.

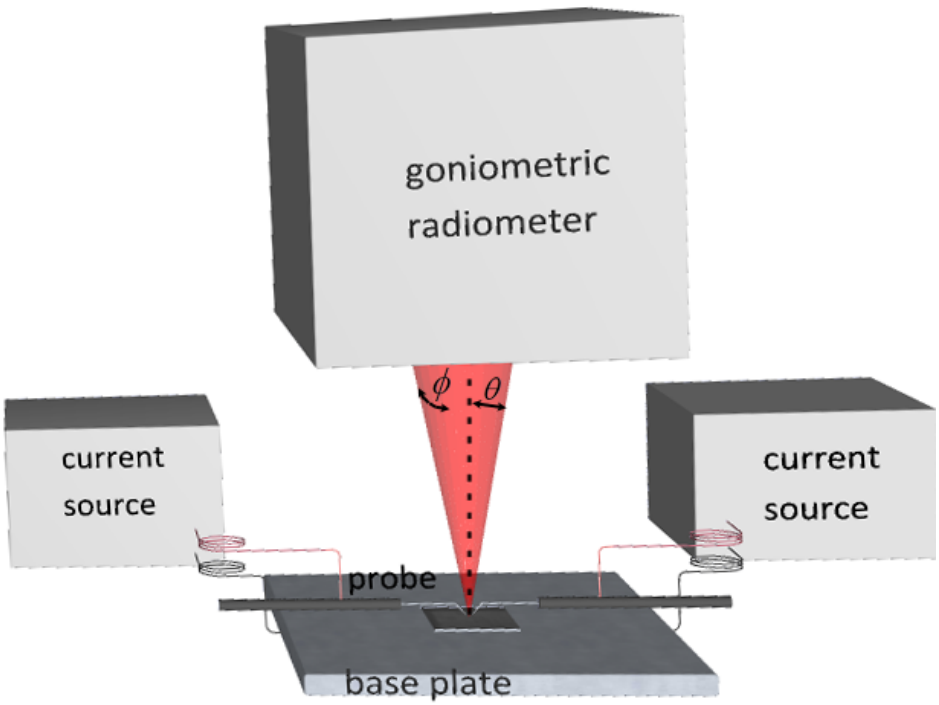

Figure 3.7: Experimental setup for acquiring far-field data.

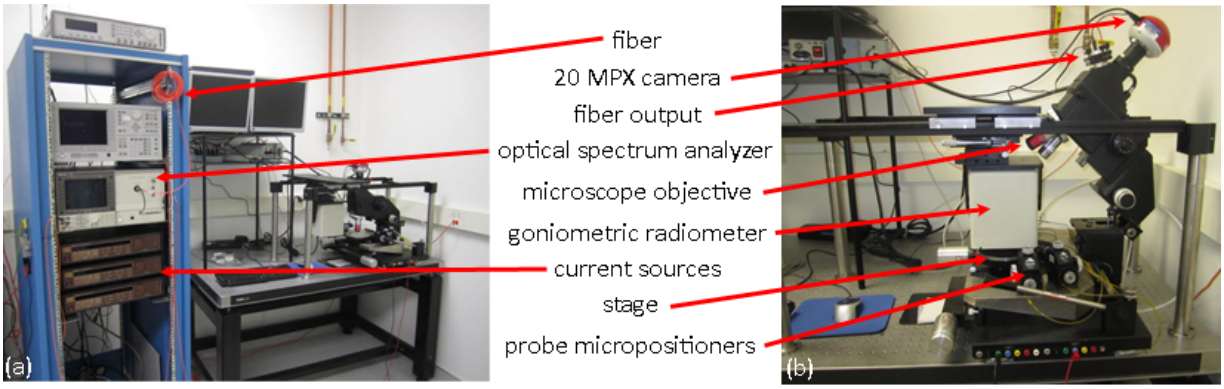

Figure 3.8: (a) Experimental setup for top-emitting VCSEL arrays. (b) Near field setup can be lifted to allow far field measurements as sketched in Figure 3.7.

A top-emitting setup to obtain dynamic steering data is shown in Figure 3.9. A receiver is translated across the far field profile to collect dynamic data at each point, which is read from the oscilloscope. A modified version to obtain high-speed dynamic data is shown in Figure 3.10. A slit is placed to spatially isolate sections of the far field,

which are then focused onto the receiver. This focusing is necessary for high-speed receivers with limited sensitivity. The time-domain intensity oscillations of the far field sections can be incrementally obtained as the slit (or receiver as in Figure 3.9) is translated across the far field beam profile. The far field profiles corresponding to the low and high signals can then be extracted from this data, allowing observation of high speed beam steering [82].

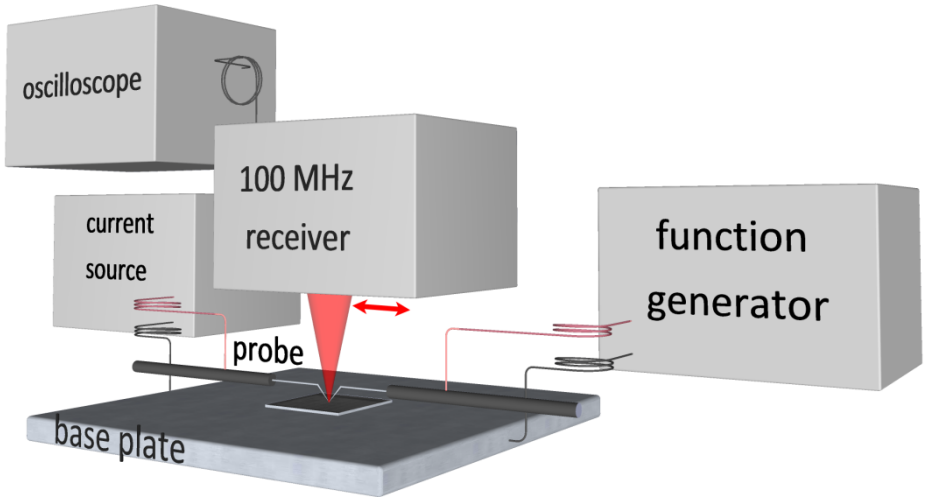

Figure 3.9: Experimental setup for extracting beam steering dynamics under 100 MHz. The free-space receiver is translated to sample varying points along the far-field beam.

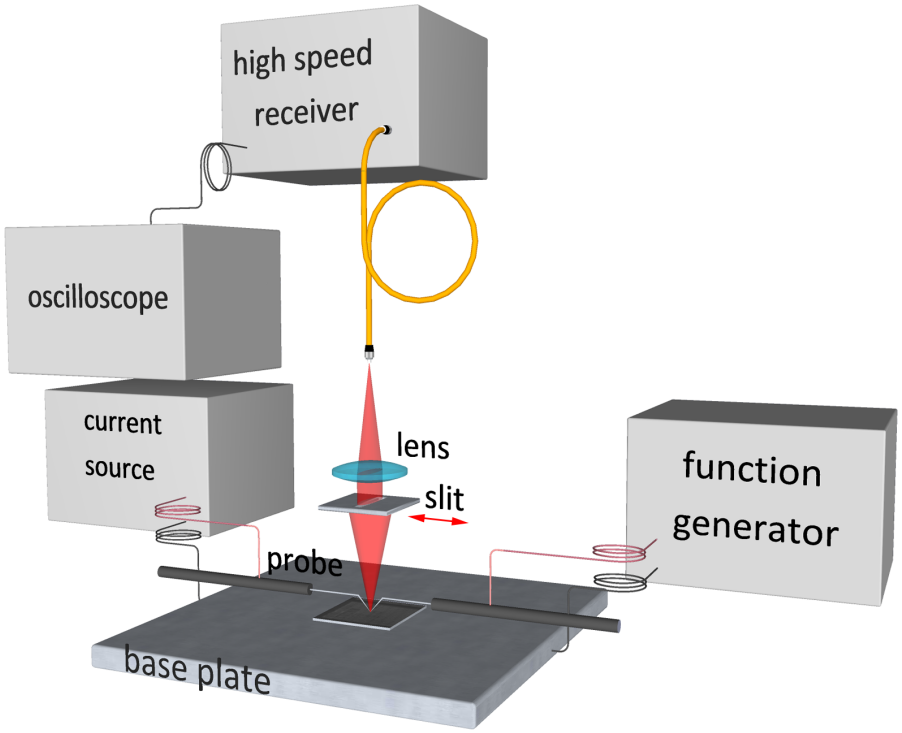

Figure 3.10: Experimental setup for extracting high-speed beam steering dynamics. The slit is translated to spatially filter varying sections of the far-field beam.

The setup shown in Figures 3.11 and 3.12 is used to characterize bottom-emitting arrays, enabling acquisition of optical power, far field, spectral and near-field data. The base plate has a 0.5 x 0.5 cm^2 hole in the middle to allow emission through the bottom substrate. The sample does not have a vacuum attachment to the base plate, although this would be a helpful feature to ensure a good connection for current flow. The photodetector, mirrors, lower camera and fiber are connected together on a 3-axis stage in order to allow focusing and lateral translation while maintaining alignment. A switchable mirror was used instead of a beam splitter to ensure maximum power to the fiber.

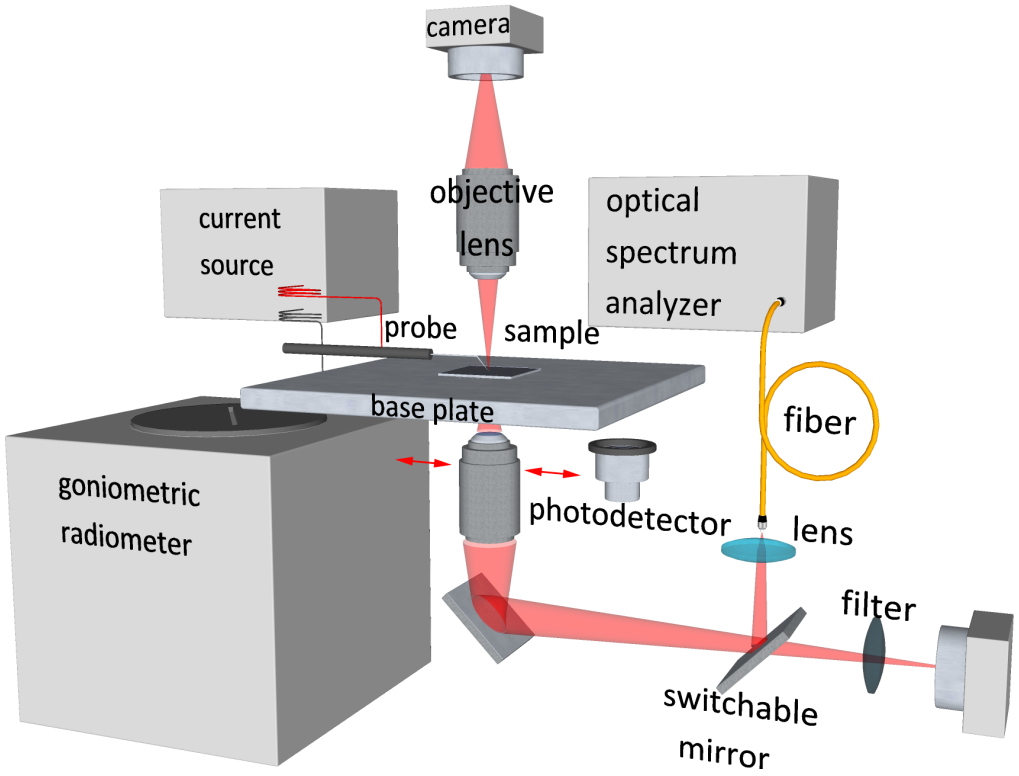

Figure 3.11: Experimental setup for optically characterizing bottom-emitting arrays, allowing collection of near-field, far-field, spectral and output power data.

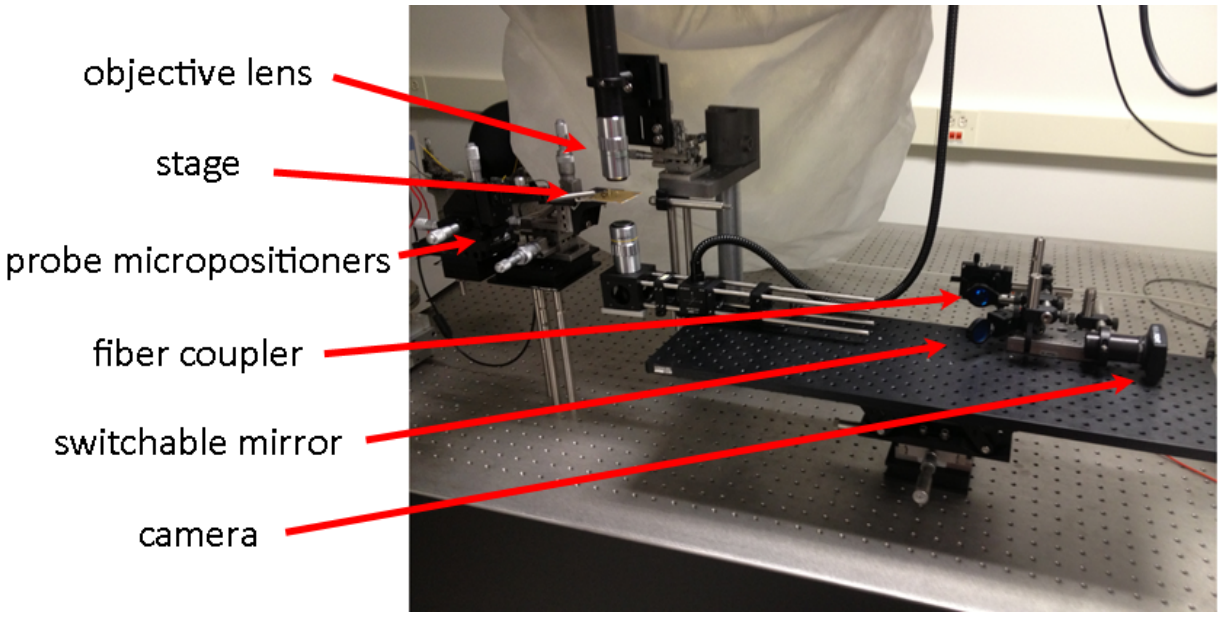

Figure 3.12: Picture of setup sketched in Figure 3.11.

Chapter 4: BEAM-STEERING MECHANISM

4.1 Introduction

This chapter discusses the optical characterization and analysis of beam steering with coherently-coupled top-emitting VCSEL arrays. The relative phase and coherence between array elements are first retrieved at the VCSEL array facet [63]. Results are compared from three different 2x1 arrays operating out-of-phase, in-phase and in-between, with respective central phase differences of π, 0 and $3\pi/2$. The phase sensitivity to current and spatially-resolved spectra are examined next [83]. The dynamics of the steering are then analyzed to gather further information with regards to the beam steering mechanism [83]. Dynamic coupled mode theory is finally applied to correlate the observed beam steering with the resonant frequency detuning between elements [64]. This chapter culminates with a posited explanation of the beam steering mechanism in coherently coupled VCSEL arrays.

4.2 Phase and Coherence Retrieval

The phase and coherence are first experimentally retrieved from three representative 2x1 VCSEL arrays with varying coupling phase differences of $\Psi = 0$, $\Psi = \pi$ and $\Psi = 3\pi/2$, where Ψ is defined as the central phase difference around which the array elements are phase locked [84]. Representative data from these arrays are shown in Figure 4.1, including near field images, near field amplitudes, and propagated and experimental far

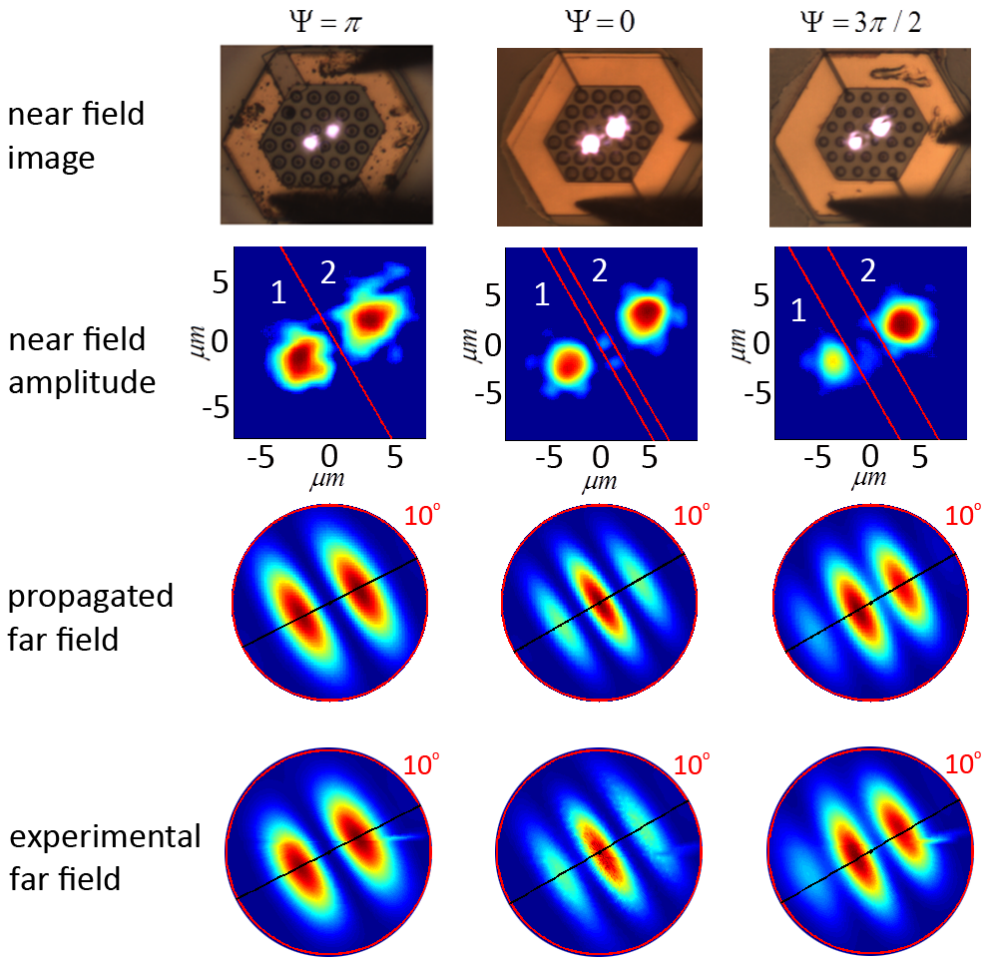

Figure 4.1: Near and far field data for three representative 2x1 VCSEL arrays with varying coupling phases. Data for the $\Psi = \pi$, $\Psi = 0$, and $\Psi = 3\pi/2$ arrays are taken at current differences of I_2-I_1 = 0, -0.14 and -0.49 mA, respectively. The red lines in the near field delineate the aperture sections used to propagate to the far field. The black lines in the far field images show where the far field profile slices were taken.

fields, all of which were taken from the setups shown in Figure 3.5 and Figure 3.7. The near field amplitude profiles were obtained as the square root of the measured intensity profiles after subtracting out the background noise. The near field was then split into the apertures delineated by the red lines in the near-field amplitudes of Figure 4.1. The left and right elements are referred to as elements 1 and 2, respectively.

Using Equation 2.5, the relative phase and coherence of the right element are obtained by matching the propagated and experimental far fields. The central near-field fringe evident in the $\Psi = 0$ and $\Psi = 3\pi/2$ arrays is assumed to be π out of phase with the average phase of elements 1 and 2, where the phase of element 1 is always arbitrarily set to 0. The relative phase of element 2, Φ_2, is determined in an iterative process until the relative amplitudes of the left and right far field lobes match those determined experimentally. This method was used in contrast to the approach of previous works where the far-field angular peaks are matched with antenna array theory [85, 86], as the latter is subject to greater experimental error. The coherence was similarly determined by an iterative process matching the relative amplitude of the far-field nulls. While previous coherence retrieval methods take the visibility and relative intensities of the near field elements into account separately [85, 86], our method accounts for both simultaneously.

Near- and far-field measurements are taken over the locking range of each array for fixed current injection to element 1, and varying current injection into element 2. The propagated-fit and experimental far field profiles are compared for the different array types in Figure 4.2(a, c and e). The profiles match well, lending credence to the underlying assumptions and accuracy of the phase/coherence retrieval method. In all three arrays it can be seen that as the current to the right aperture is increased, the far field is pulled to the right. This is caused by a relative phase lag in element 2

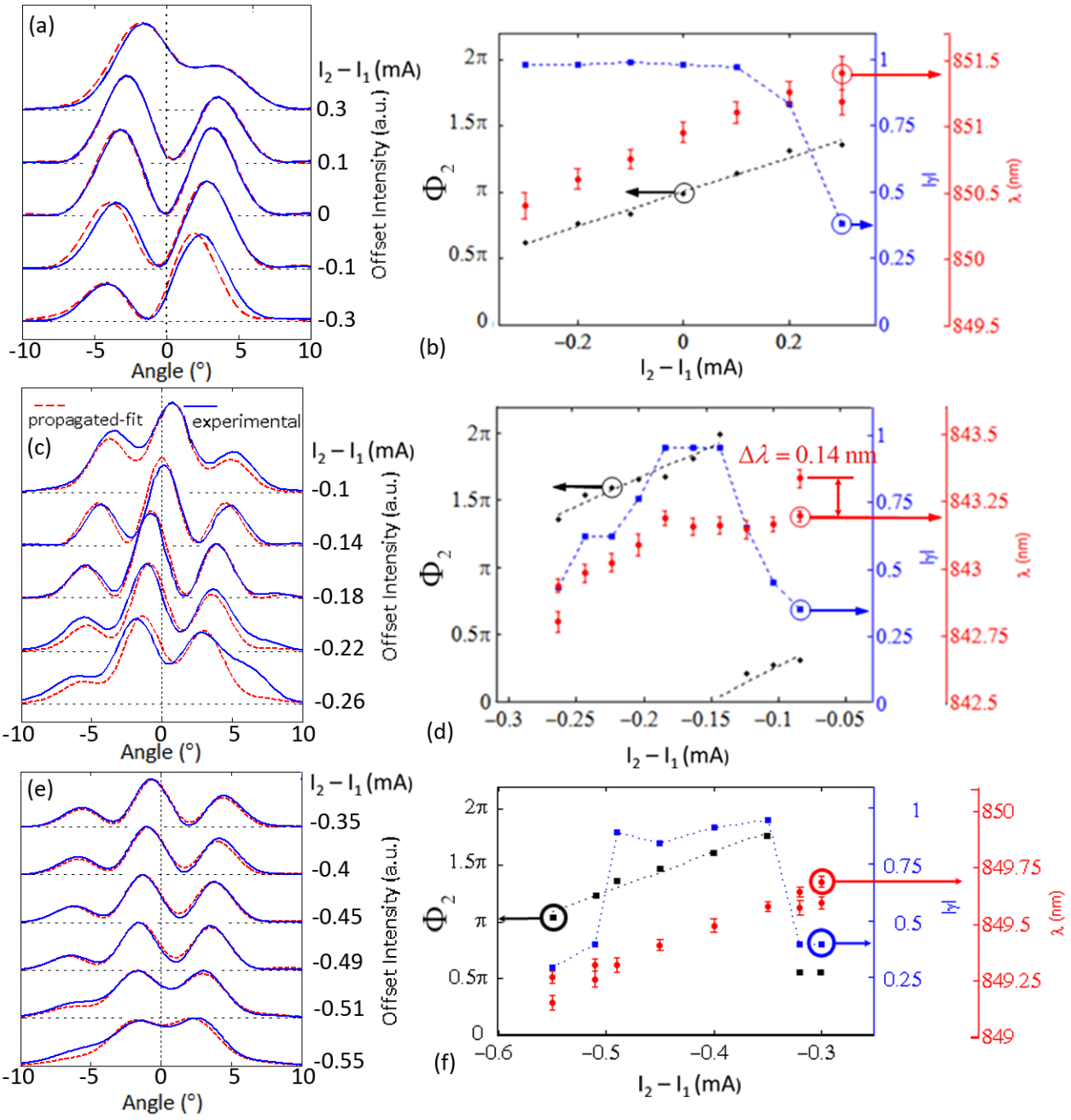

Figure 4.2: Far field profiles, spectrum, phase and coherence as a function of current difference for arrays operating with (a,b) Ψ = π, (c,d) Ψ = 0, and (e,f) Ψ = 3π/. Far field profiles were taken along black lines in Figure 4.1.

that increases with current to element 2, as plotted in Figure 4.2(b, d and f). It is also observed in Figure 4.2(b, d and f) that the arrays tend to maintain high coherence when

operating near Ψ, but completely lose coherence $(|\gamma| \to 0)$ when pushed beyond 0.5π in either direction, which is the apparent limit of their locking ranges [20].

4.3 Spectrum

It is seen from Figure 4.2(b, d and f) that the spectrum splits as the array is pushed beyond its coherent locking range. The simplest explanation is that these two spectral modes represent individual, non-coupled lasers emanating from each element, where the current difference has caused their resonant frequencies to shift beyond the locking range. An alternative explanation would be that the spectral modes represent two distinct modes including contributions from both elements, but at different wavelengths. To examine this, the experimental setup shown in Figure 3.6 was used to examine the spatially-resolved spectrum of each element. The 2x1 VCSEL array under test had a central emission of approximately 980 nm, but was otherwise very similar to the $\Psi = 0$ array discussed above. It operates coherently with 3.6 and 3.5 mA applied to elements 1 and 2, respectively, and loses coherence when the right element current is driven beyond a ±1 mA range. A 65-µm core fiber was used to capture the spectra encompassing both modes and a 9-µm core fiber was used to capture the individual spectra of the left and right elements [83]. The inset image in Figure 4.3 shows the approximate near-field spatial dimensions the spectra were obtained from.

The spectra show that with a reduced current of 3.4 mA to element 2, the element emission is predominantly at a lower relative wavelength than that of element 1. Similarly, if we increase the current in element 2 to 3.6 mA, the emission from element 2 is shown to reside predominantly at the higher wavelength relative to element 1. The results indicate that outside of the locking range, at I_2 = 3.4 or 3.6 mA, the elements are lasing almost completely independently at their respective resonant wavelengths. As the current difference between elements increases and the coherence between elements decreases, there is likely some transition from coupled modes to independent modes at each element, which warrants further examination. The spatially-resolved spectra also reveal that as the current to a given element is increased with respect to the other, its respective resonant wavelength also increases. This is consistent with the thermo-optic effect for GaAs and AlAs, where $\partial n / \partial T \approx 4 \cdot 10^4 \mathrm{K}^{-1}$ and $\approx 10^4 \mathrm{K}^{-1}$, respectively, suggesting the relative temperature difference between elements is the dominant factor in their resonant wavelength detuning.

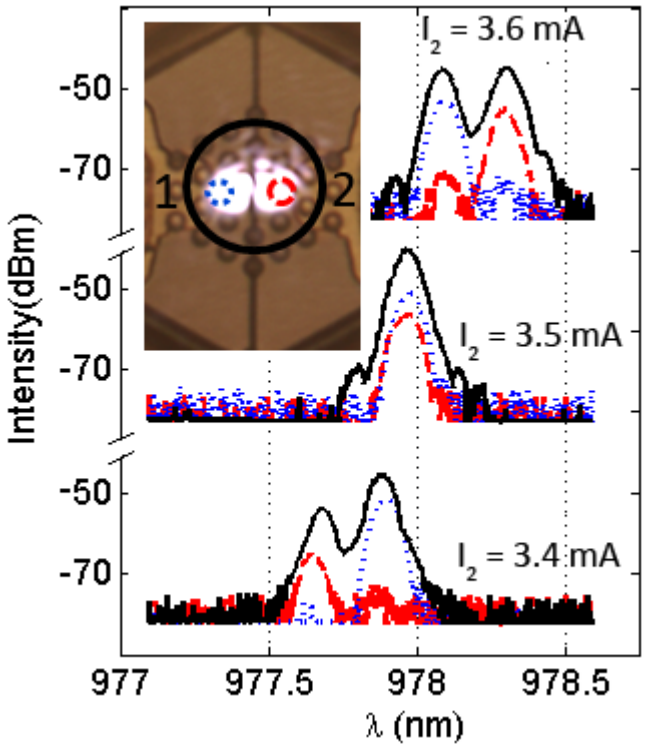

Figure 4.3: Spatially resolved spectra from near field magnified onto fibers with 9 and 62.5 µm diameter cores. Current to element 1 was held constant at 3.6 mA while current to element 2 was varied. Inset shows approximate locations and diameters contributing to the displayed spectra.

4.4 Phase Sensitivity

It is noteworthy that while a current change of ≈ 20 mA is required to achieve a π phase difference in slab-coupled edge-emitting lasers [87], the VCSEL arrays demonstrated here approach a π phase difference over much smaller current and voltage ranges, as tabulated in Table 4.1. The coherently coupled VCSEL arrays thus demonstrate several orders of magnitude greater phase sensitivity to current. It is also noteworthy that typical direct-modulation VCSELs have a peak-to-peak modulation voltage between 0.5 and 2 V, while the VCSEL arrays shown herein can approach a full π phase difference with peak to peak voltages as low as 110 mV.

Table 4.1. Resistance between contacts and current and voltage differences over the locking range of various devices. *Data from device shown in Figure 4.3.

Ψ	$R_{contact}$ (Ω)	ΔI (μA)	ΔV (mV)
0	6300	160	250
π	2600	500	1460
3π/2	4000	200	618
π*	4650	120	110

The differing sensitivities of the arrays is found to depend on the FIB etch depth, which affects the lateral resistance between the element contacts, as also tabulated in Table 4.1. It is apparent that the phase sensitivity increases with increasing current confinement, which is achieved by the focused ion beam etch. The sensitivity could also be increased if the coupling constant between the elements could be decreased, which would decrease the locking range. This is explained further in Section 4.6.2.

4.5 Beam Steering Dynamics

In the following section, the beam steering characteristics are examined with a time-varying input current at modulation speeds of 100 Hz, 100 kHz and 100 MHz.

4.5.1 Steering Modulation Speed: 100 Hz

We first characterize beam steering at low modulation speeds using a simplified version of the experimental setup shown in Figure 3.9, where the receiver is placed and translated within the unfocused far-field beam above the sample. An array with $\Psi = 3\pi/2$, similar to that characterized in Figure 4.2(e and f), is first examined. The current to element 1 is held constant while the current to element 2 is modulated in a square wave with a pattern generator between 3.06 and 3.13 mA at 100 Hz. The time-domain current to element 2 and the corresponding photo-current signals received at angular locations of 0 and 0.8° are shown on the right side of Figure 4.4. The photoreceiver, located 6 cm from the VCSEL array and subtending a 0.8° angular width, is translated across the far field to obtain the photocurrent signals at incremental angular positions. The far field intensity profile can then be recreated based on these signals, as illustrated in Figure 4.4, where the 'low' far field intensity at each angular increment is found as the average of the detected signal during the times of low current to element 2 (I_2 = 3.06 mA).

The far field profiles were also taken with the radiometer at the direct current (DC) high and low values of I_2, as shown by the dotted lines in Figure 4.4. Under both DC current injection and 100 Hz modulation, the far field profile is found to steer to the right with increased current to element 2, consistent with Figure 4.2(a, c, e).

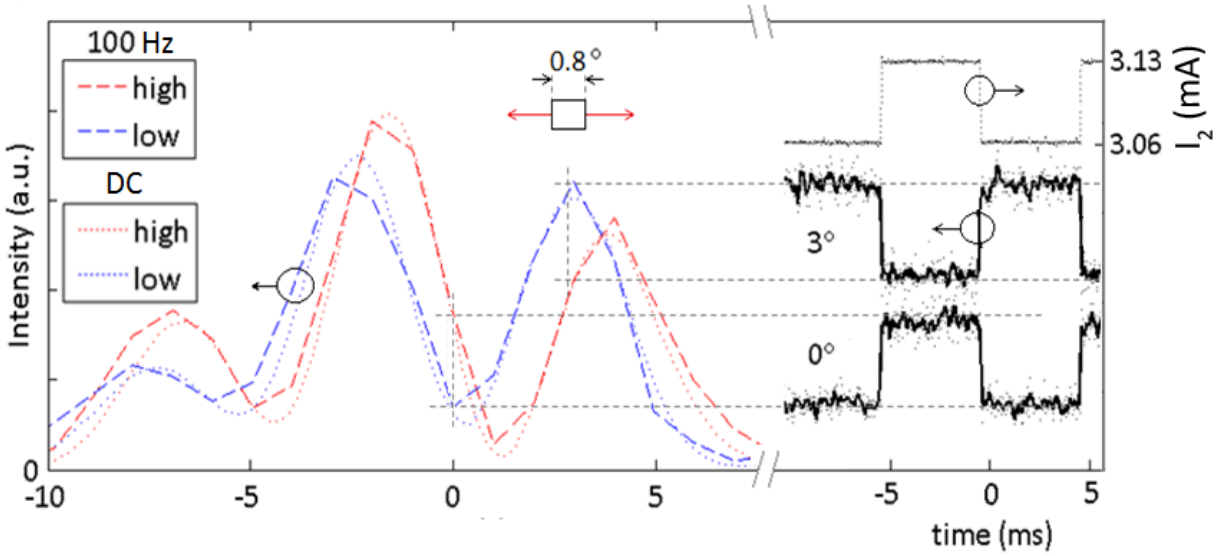

Figure 4.4: Far field profiles obtained from translating photoreceiver at 100 Hz (dashed) and from radiometer with DC current (dotted). The dashed far field profiles are obtained from the intensity peaks and nulls of the time-domain signals corresponding to the high and low input currents.

4.5.2 Steering Modulation Speed: 100 kHz

The modulation rate is next increased to 100 kHz. At this speed we find that the far field profile continues to shift to the right with higher current to the right element, consistent with measurements at 100 Hz and DC. However, the dynamics of the photocurrent signals shown in Figure 4.5 at angular locations of 0 and 3° reveal a rise/fall time on the order of 5 µs. Similar delays of 1-20 µs have been observed for intensity modulation and beam steering with GaAs-based VCSELs dependent on thermal lensing [15, 88, 89]. The observed rise/fall time in Figure 4.5 is therefore consistent with a thermally-dominated beam steering mechanism. The increase of current to the right element is accompanied by an increase in the relative temperature on that side of the array, which increases the relative index on that side in accordance with the thermo-

optic effect. The beam steering speed that is dependent on the thermo-optic effect is thus limited to the kHz regime [83].

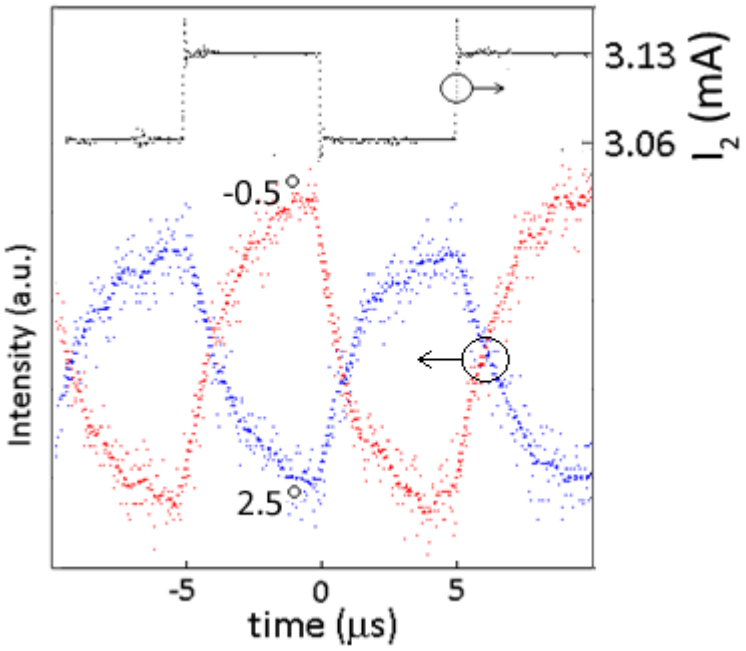

Figure 4.5: Photocurrent received at the angular positions of -0.5 and 2.5° while the current to element 2 is modulated at 100 Hz. A rise/fall time on the order of 5 μs is evident.

4.5.3 Steering Modulation Speed: 100 MHz

If we increase the modulation rate beyond the temporal limits of the temperature response to 100 MHz, we obtain the far field profiles shown in Figure 4.6, which exhibit an entirely different beam steering phenomena. The steering shown corresponds to a record high angular speed of 1.4×10^8 deg/s over a beam steering range of » 0.7° [83]. The difference at this modulation rate, however, is that we find the beam is steered to the *left* with increased current to element 2, which is the opposite of what we find at low modulation speeds. This opposite steering direction is consistent with the carrier-

induced index change, where the index is *suppressed* with increasing current per $\partial n / \partial N \approx -10^{-21}$ cm^3 [90], rather than increased as with the thermo-optic effect.

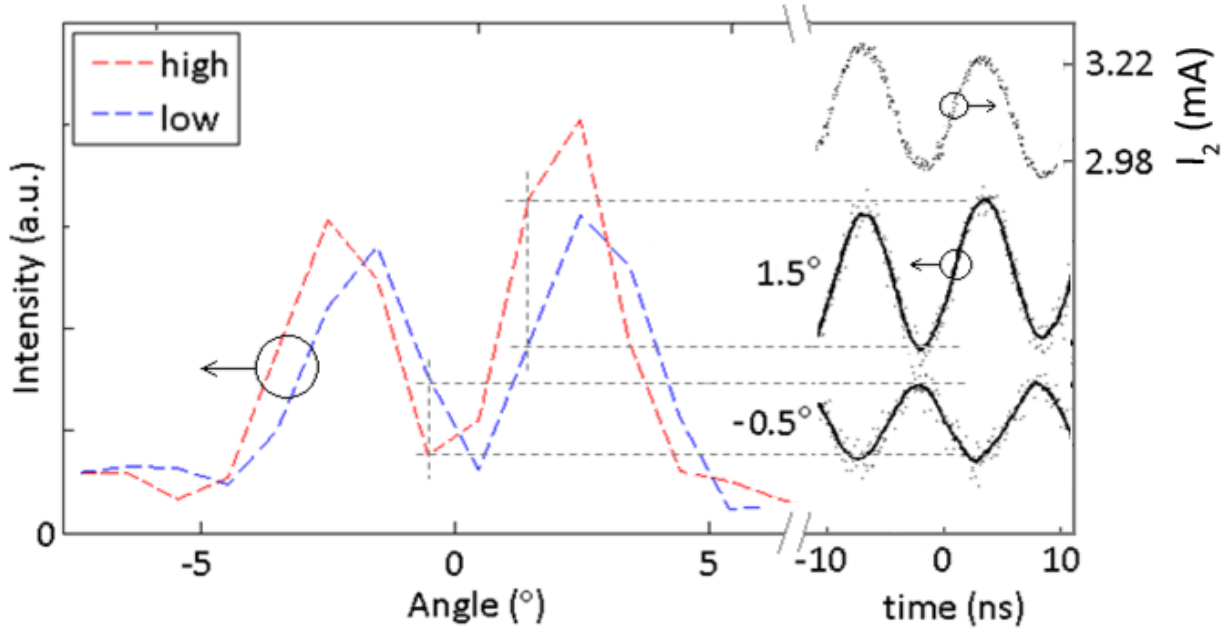

Figure 4.6: Far field profiles at 100 MHz. The photocurrent signals on the right, received at the angular locations shown, demonstrate how the far field was constructed based on the signal values corresponding to the times of high and low input current to element 2.

While the thermo-optic effect is found to dominate at DC and slower modulation rates, when we modulate at faster rates (≥ 10 MHz), the thermal dynamics are effectively neutralized since the temperature cannot keep up with the modulating current. At higher speeds, the weaker and opposite effect of the carrier-induced index change, where the index decreases with increasing current, is then found to be the dominant phase-shifting mechanism. A similar progression from thermal to carrier-dominated phase change at increased current-injection modulation speeds has been shown for injection-locked edge-emitting lasers [21].

4.6 Steering Mechanism

The above analysis indicates that the beam steering mechanism is dependent on the relative index differences between the array elements. There are then two explanations that might be offered as to the root of the phase-shifting mechanism observed in coherently coupled VCSEL arrays: a spatial phase shifting mechanism similar to almost all non-mechanical beam steering methods [1], or a temporal phase shift within the active region.

4.6.1 Spatial Phase Shift

The simplest explanation for the beam steering mechanism would be to view the light propagation path from the active region to the VCSEL facet as traveling through a waveguide, where the two sections of the optical mode are assumed to be phase-locked at the quantum wells within the active region. Then, as the beam propagates from the active region up through the DBRS to the VCSEL facet, the right section of the optical mode sees a higher index and therefore lags the left section. In other words, the right portion of the beam undergoes a spatial phase lag.

Based on the beam steering dynamics and spatially-resolved spectra as discussed previously, we can safely conclude that beam steering observed at DC or low modulation speeds is caused by the localized index changes in the cavities produced by the thermo-optic effect. We can then make some estimates based on the spectral

splitting of $\approx$0.14 nm observed in Figure 4.2d for the Ψ = 0 array. Given a base index of 3.45 within the $Al_{0.3}Ga_{0.7}As$ cavity and the relation $\Delta n_{eff} / n_{eff} \approx \Delta\lambda_0 / \lambda_0$ [91], the thermo-optic coefficients provided above for GaAs and AlAs, the index and temperature difference between the cavities can be estimated as Δn_{eff}= 5.5 x 10^{-4} and ΔT = 1.8° K, respectively.

Assuming ΔT remains constant through the top 27 DBR periods to the VCSEL output facet, the index change in each semiconductor layer can be estimated. From this the total optical path length difference and spatial phase shift experienced by the right section of the optical mode can be estimated. While we observe a phase shift of $\approx 0.5\pi$ at this temperature difference (although with low coherence), the estimated spatial phase lag only accounts for $\approx 0.003\pi$ of phase difference. In order to exclusively account for the observed phase shift with a spatial lag, the cavities, which are only separated by approximately 8 μm, would require an unrealistic temperature difference of $\approx$260°K. A spatial phase shift therefore does not provide a sufficient explanation for the phase shifting observed in VCSEL beam steering.

4.6.2 Temporal Phase Shift

As previously derived in Equation 2.13, dynamic coupled mode theory leads to the following correlation between the temporal phase shift between coupled elements and the resonant frequency detuning between them [64]:

$$\Delta\omega = \omega_2 - \omega_1 = -\kappa\left(\alpha\left(\frac{X_1}{X_2}+\frac{X_2}{X_1}\right)\sin\left(\Phi_1-\Phi_2-\psi\right)+\left(\frac{X_1}{X_2}-\frac{X_2}{X_1}\right)\cos\left(\Phi_1-\Phi_2-\psi\right)\right), \quad (4.1)$$

where the variables are again defined as the resonant frequencies, ω_m, the coupling strength, κ, the linewidth enhancement factor, $\alpha = -5$ [92], the normalized field amplitudes, X_m, and the phase shift, $\Phi_1 - \Phi_2 = -\Phi_2$. This equation is applied to the $\Psi = \pi$ and $\Psi = 3\pi/2$ arrays shown in Figure 4.1 and Figure 4.2. The normalized fields X_1 and X_2 are determined as the total integrated amplitude measured in each near-field element. As can be seen from the near field amplitude of the $\Psi = 3\pi/2$ array shown in Figure 4.1, $X_2 > X_1$ in this array at the given current difference. These values were obtained from each of the near field images corresponding to the varying current differences. The coupling strength can be approximated from Equation 4.1 as $\kappa = -\Delta\omega_{max}/2\alpha$ where $\Delta\omega_{max}$ is the maximum resonant frequency detuning within the locking range, outside of which spectral splitting is observed. This approximation of κ ensures that solutions to Equation 4.1 exist within the locking range, but not outside of it. The values of $\Delta\lambda_{max}$ are obtained as illustrated in Figure 4.8 (p. 61), and lead to the κ values shown in Table 4.2.

Table 4.2. Coupling values obtained for two different arrays.

Ψ	Δλ (nm)	Δω (GHz)	κ (GHz)
3π/2	0.06	167	16.7
π	0.17	444	44

4.6.2.1 Phase Retrieval

Within the locking range, $\lambda_{coupled}$ is observed while λ_1 and λ_2 cannot be, by definition. In order to extract the phase based on Equation 4.1, we have to first estimate how $\Delta\lambda = \lambda_1 - \lambda_2$ varies within the locking range. Since for the $\Psi = 3\pi/2$ array we have $\Delta\lambda$ on either side of the locking range, one approach is to assume $\Delta\lambda$ varies linearly across the locking range. For the $\Psi = \pi$ array we only observe spectral splitting on one side of the locking range, as shown in Figure 4.2b. In order to extrapolate $\Delta\lambda$ across the locking range we assume $\Delta\lambda = 0$ at the point where $I_2 = I_1$, because we have extracted a π phase difference at that point. So given these two values of $\Delta\lambda$ for the $\Psi = \pi$ array, we can linearly extrapolate $\Delta\lambda$ at the other points. Given these assumptions, the phase values retrieved from the propagated-fit method and from Equation 4.1 are compared in Figure 4.7. The retrieved phases are found to match well for the $\Psi = \pi$ array while slight variance is observed for the $\Psi = 3\pi/2$ array, which could be attributed to a non-linear progression of $\Delta\lambda$ across the locking range.

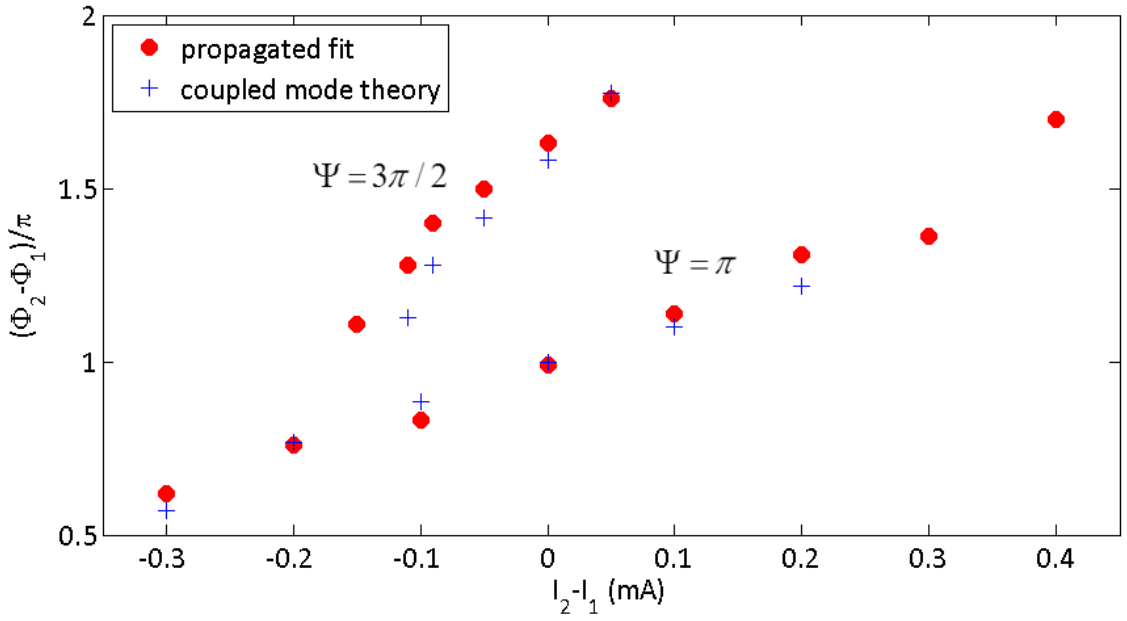

Figure 4.7: Relative phase values retrieved from propagated-fit method and from coupled mode theory. The current difference for the $\Psi = 3\pi/2$ array is offset by +0.4 mA for clarity.

4.6.2.2 Native Resonance Retrieval

Another approach is to use the phase extracted from the propagated-fit method to retrieve the native resonant wavelengths within the locking range, where they are related to the coupling wavelength by [64]

$$\begin{aligned}\omega_1 &= \omega_{coupled} - \kappa\frac{X_2}{X_1}\left[\cos(\phi_1-\phi_2-\psi)-\alpha\left(\left[\sin(\phi_1-\phi_2-\psi)\right]\right)\right]\\ \omega_2 &= \omega_{coupled} - \kappa\frac{X_1}{X_2}\left[\cos(\phi_1-\phi_2-\psi)+\alpha\left(\left[\sin(\phi_1-\phi_2-\psi)\right]\right)\right]\end{aligned}. \qquad (4.2)$$

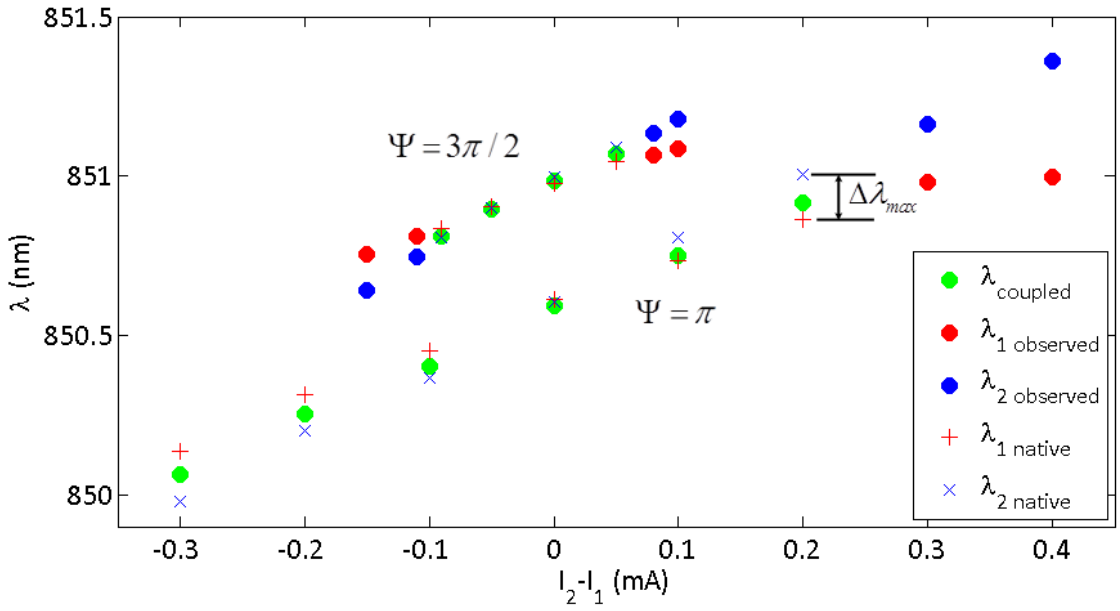

Figure 4.8: Peak wavelength values measured (solid) and retrieved (+ and x) from Equation 4.2. The current difference and wavelength of the $\Psi = 3\pi/2$ array are offset by +0.4 mA and +1.5 nm, respectively, for clarity.

Relatively linear progressions of the native resonance wavelengths across the locking range are retrieved for both arrays, as shown in Figure 4.8. It is also noteworthy that for the $\Psi = 3\pi/2$ array, $\lambda_{coupled}$ is found to reside closer to λ_2 due to the disparity between X_1 and X_2.

4.7 Summary

We have examined several coherently coupled 2x1 VCSEL arrays. By extracting the relative phase and coherence of the arrays, and by examining their spatially-resolved spectra and beam-steering dynamics, we have concluded the beam steering is caused by a relative index differential between the array elements. We have further determined this index difference is primarily dependent on the thermo-optic and carrier-induced

index changes at low and high modulation speeds, respectively. Finally, we have applied dynamic coupled mode theory to show that by simply considering the spectral detuning between elements and their locking range, we can arrive at a good approximation of the phase shift between elements that is observed within the locking range. The application of coupled mode theory thus completes our theoretical understanding of the beam steering mechanism in coherently coupled VCSEL arrays.

Chapter 5: BOTTOM-EMITTING ARRAYS

5.1 Introduction

Bottom-emitting coherently coupled VCSEL arrays offer pronounced advantages over their top-emitting counterparts. The key design advantages include direct current injection into the array elements and reduced thermal resistance between the active region and heat sink. It is difficult to achieve uniform current injection in coherently-coupled top-emitting arrays with more than two elements in both dimensions. One approach for top-emitters is to use metal contacts between the array elements, but unless carefully phase-matched [45], this has the undesired effect of discriminating against the preferred in-phase mode [42, 43]. The previously reported bottom-emitting coherent arrays have employed reflectivity modulation and/or mesa etching, which led to out-of-phase operation [42, 43, 93]. The bottom-emitting VCSEL arrays presented in this chapter are designed to have an antiguided index profile created by a simple, self-aligned process, which allows in-phase, continuous wave (CW) operation [57].

The devices were fabricated as discussed in Chapter 3, and characterized with the setup shown in Figures 3.11 and 3.12. Large, 50x50 arrays were initially fabricated, and a focused ion beam etch was subsequently performed to define smaller array sizes. The significant achievements detailed in this chapter include the demonstration of a 2x1 array operating in the preferred in-phase mode, and improved current injection

uniformity for a 3x3 array [57], both of which are important steps toward large coherently coupled VCSEL array sizes.

5.2 Single VCSEL Emitter

A single-element bottom emitter with a 5 µm diameter implant aperture is shown by the SEM image in Figure 5.1a. Figure 5.1 also shows the oscillating behavior in the CW light vs. current curve that stems from the interference effects between the substrate interfaces to the DBR and air. The far field profiles of Figure 5.1b are also found to vary with the cyclic interference effects, while the spectra shown in Figure 5.1c

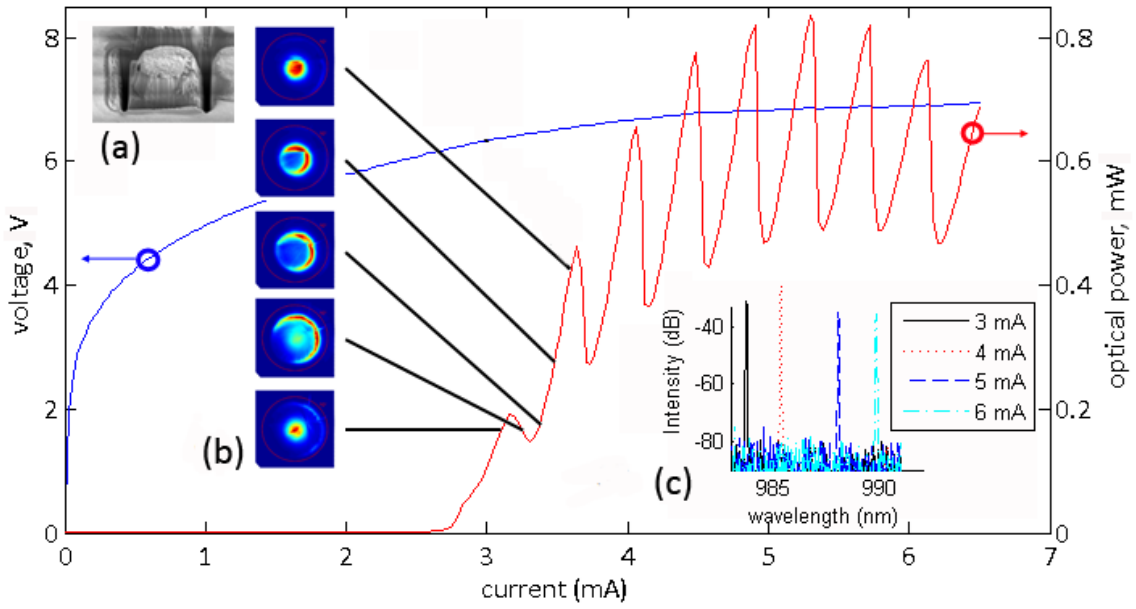

Figure 5.1: LIV curve and other data for a single, 5 µm diameter VCSEL. (a) SEM image showing the FIB etch around the device perimeter. (b) The far-field pattern is shown to cycle with the oscillating LIV curve, while the (c) spectra indicate single mode operation through rollover.

indicate single mode behavior through rollover. The far field full width at half maximum (FWHM) for this single element is found to be 5.4°.

5.3 2x1 VCSEL Array

A simplified structure of the 2x1 array characterized is shown by the sketch in Figure 5.2. The current is directly injected into the laser elements and confined by both the ion implantation and the FIB etch.

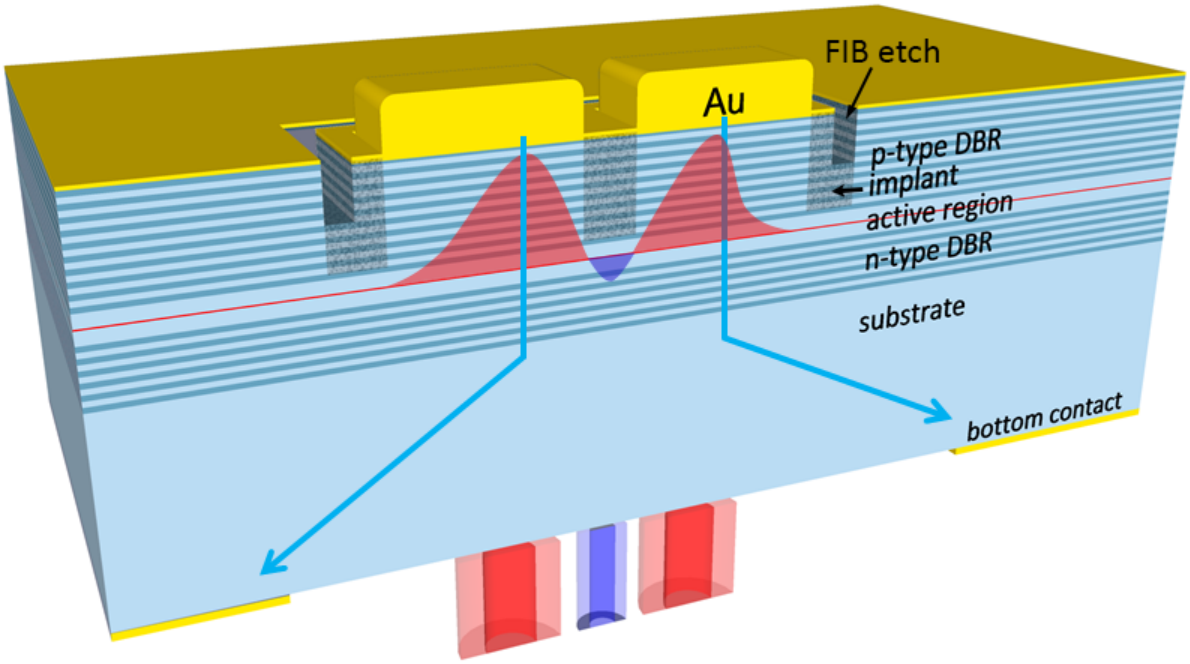

Figure 5.2: Bottom-emitting 2x1 VCSEL array structure. The arrows indicate current flow and the blue and red beam profiles represent operation in the preferred [+ - +] mode.

Near-field images of the array operating below threshold and at 8.7 mA (1.3 x $I_{threshold}$) with 0.9 mW output power are shown in Figure 5.3a and Figure 5.3b, respectively. The sub-threshold image reveals the carrier density distribution caused by the ion implantation apertures. A slice of the near field is taken at the black line in Figure 5.3a to estimate the refractive index profile. The slice is taken diagonally because the [+ - +] mode is observed to fit within the index profile in this direction. The

approximated index profile is shown in Figure 5.3c and is determined from the same maximum carrier density value (5 x 10^{18} cm^{-3}) and temperature distribution used in Ref. [73]. Given this index profile, a one-dimensional Helmholtz equation is solved using the finite difference method to yield the theoretical near field modal intensity also shown in Figure 5.3c [73]. The measured near field intensity is taken along the black line shown in Figure 5.3b for comparison in Figure 5.3c. The theoretical and experimental profiles show good agreement given the approximations made in determining the index profile.

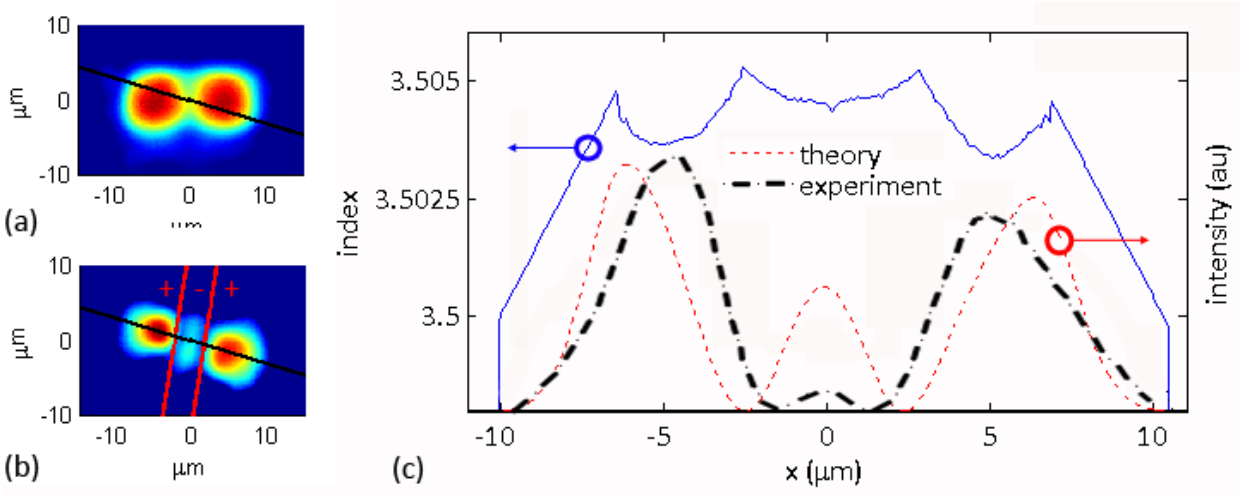

Figure 5.3: Near-field of 2x1 array (a) intensity below threshold and (b) amplitude at a current of 8.7 mA operating in the [+ - +] mode. (c) Approximated refractive index profile and theoretical and experimental near field profiles obtained along the black lines in (a) and (b).

Upon separating the near field into the three elements delineated by the red lines shown in Figure 5.3b, the left and right elements labeled '+' are assumed to be in-phase while the central lobe labeled '-' is assumed to be π out-of-phase. The beam is then propagated to the far field based on the Fraunhofer propagation method [63]. This

simulated far field, displayed in Figure 5.4a, can be compared to the experimentally determined far field of Figure 5.4b, which has a FWHM of 2.1°. The far fields show good agreement, especially considering the interference effects from the air/substrate interface were not taken into account with the simulation. The lasing spectra, plotted at various currents in Figure 5.4c, show the array operates in a single mode under an injection current range of 8.7 ± 0.5 mA. The near field, far field and spectral data thus confirm the array is operating in the [+ - +] mode with the preferred on-axis, low-divergence, far-field maximum.

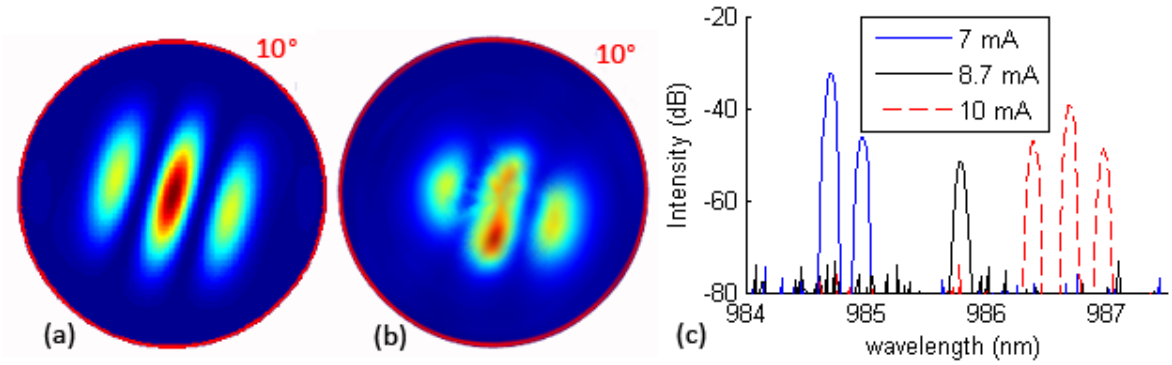

Figure 5.4: (a) Simulated and (b) experimental far field intensities. (c) Spectra showing single-mode operation with an injection current of 8.7 mA.

5.4 Two-Dimensional VCSEL Arrays

Intensity profiles for a 2x2 array are depicted in Figure 5.5. The sub-threshold near field intensity is shown in Figure 5.5a, indicating gain pixelation as desired. The far field at 6.4 mA (1.3 x $I_{threshold}$) current injection is shown in Figure 5.5c, and exhibits a narrow on-axis lobe as expected for a two-dimensional in-phase array [46]. However, the corresponding near field image in Figure 5.5b and the multimode spectral data (not

shown) do not correspond with a single in-phase mode. The FWHM of the central far-field lobe in Figure 5.5c is 3.8°, which is between that mentioned above for the single element and the in-phase 2x1 array, indicating partial coherence.

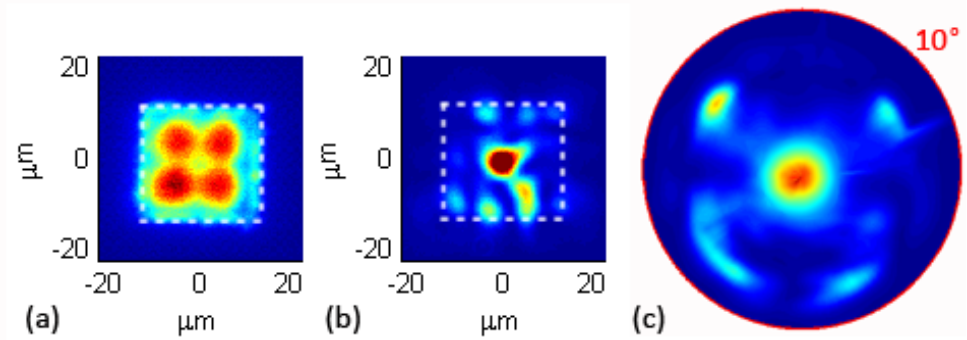

Figure 5.5. Near field intensity of 2x2 array operating (a) below threshold and (c) with current injection of 6.4 mA. (c) Far field intensity under 6.4 mA, showing an on-axis far field intensity peak with reduced divergence.

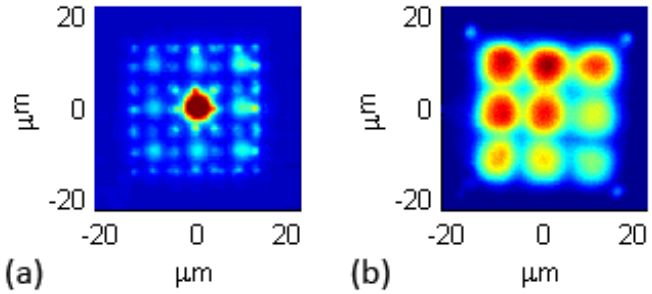

Figure 5.6: Near-field sub-threshold intensity profiles of (a) top-emitting and (b) bottom-emitting 3x3 VCSEL arrays.

The sub-threshold intensity images of top- and bottom-emitting 3x3 VCSEL arrays are shown in Figure 5.6a and Figure 5.6b, respectively. The current in the bottom-emitting array is found to distribute much more evenly than in the top-emitting array, which is a critical necessity for scaling beyond two elements in either dimension. Above threshold this 3x3 array was found to support multiple modes simultaneously due to lack of sufficient modal discrimination.

5.5 Conclusion

Various ion-implanted bottom-emitting VCSEL array geometries have been characterized. We have demonstrated the first in-phase operation of a coherently-coupled bottom-emitting VCSEL array and shown improved current uniformity in a large array, representing two critical steps towards coherent, high-brightness, two-dimensional VCSEL arrays. The primary challenge encountered is lack of sufficient modal discrimination. Improvement requires careful design and control of the real and imaginary parts of the array's index profile. Some approaches to achieve this include varying the element size and separations, incorporating a photonic crystal pattern [41, 68], and patterning the top metal to vary the reflectivity profile [42, 45]. The undesirable interference effects arising from the substrate/air interface can be mitigated by deposition of an anti-reflection coating onto the substrate [94].

Chapter 6: SUMMARY

6.1 Overview

Coherently coupled VCSEL arrays have many features that make them viable candidates for beam steering and high-brightness applications. The advantages of VCSEL arrays for both applications include their small size, low cost, durability, manufacturing ease and single longitudinal mode. Their primary advantages specific to beam steering and high-brightness applications include their record high beam steering speed [83] and two-dimensional configurability [14], respectively.

6.2 Beam Steering

We have examined coherently coupled 2x1 arrays with coupling phases of $\Psi = 0$, $\Psi = \pi$ and $\Psi = 3\pi/2$. We first retrieved the phase and coherence of the three array types as they were tuned through their respective locking ranges by differential current injection into their two elements [63]. The propagated and experimental far fields showed good agreement, verifying both the phase and coherence data collected and the underlying assumptions of the applied Fraunhofer approximation. The data also showed the VCSEL arrays had record high phase sensitivity to current [83].

By examining the spatially-resolved spectra and beam-steering dynamics of similar arrays, we have concluded the beam steering is caused by a relative index differential

between the array elements [83]. Further, we have determined this index difference is primarily dependent on the thermo-optic and carrier-induced index changes at low and high modulation speeds, respectively [83]. Finally, we have applied dynamic coupled mode theory to show that the observed temporal phase shift between elements is caused by the detuning of their resonant wavelengths [64]. Hence, a complete theoretical connection between the differential current injection and the beam steering direction has been established in this thesis, as illustrated in Figure 6.1.

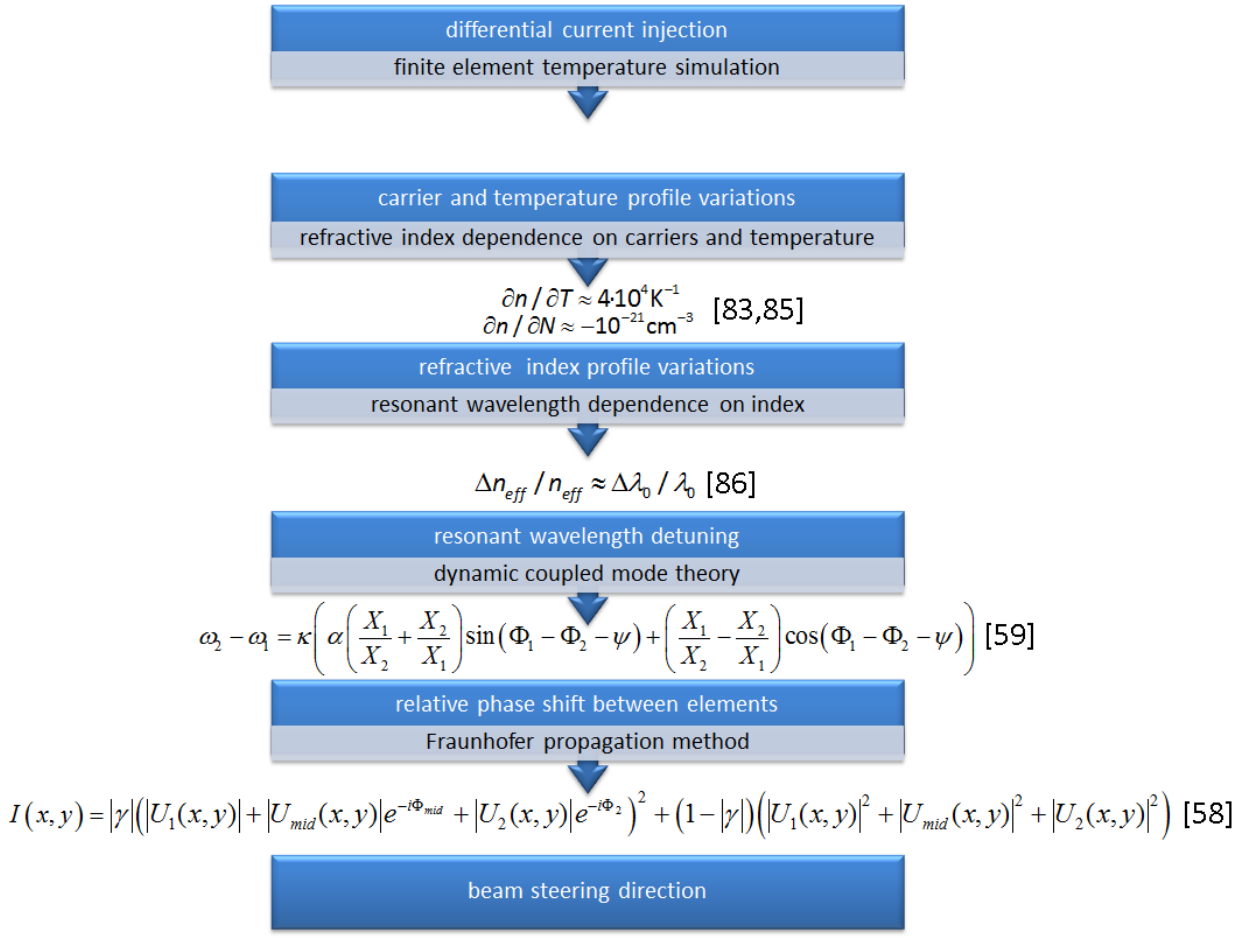

Figure 6.1: Progression and links between differential current injection and beam steering direction.

6.3 Bottom-Emitting Arrays

The key advantages of bottom-emitting over top-emitting arrays for high-brightness applications include the capability of direct current injection into array elements and a reduced thermal resistance between the active region and heat sink. The bottom-emitting VCSEL arrays were designed to have an antiguided index profile created by a simple, self-aligned process, which allows in-phase, continuous wave operation [57]. Various ion-implanted bottom-emitting VCSEL array geometries were characterized. We demonstrated the first in-phase operation of a coherently-coupled bottom-emitting VCSEL array and showed improved current uniformity in a 3x3 array, representing two critical steps towards coherent, high-brightness, two-dimensional VCSEL arrays.

6.4 Future Work

There are many potentially fruitful avenues of continued research to build on over a decade of ground-breaking work devoted to coherently-coupled VCSEL arrays performed in the photonic devices research group. Three such avenues include high speed beam steering, increased modal discrimination and scaling up of the array sizes.

6.4.1 High Speed Beam Steering

Since the observed beam steering has recently been explained by dynamic coupled mode theory [64], the theory can now be extended to identify the temporal limits of beam steering with coherently coupled VCSEL arrays. These arrays have already

demonstrated record-high beam steering speeds [83], and simulations have suggested such arrays are capable of modulation speeds over 40 GHz [95], well above the relaxation oscillation frequency of directly-modulated VCSELs.

6.4.2 Modal Discrimination

Characterization of the implant-defined bottom-emitting VCSEL arrays has shown that while they can support the preferred in-phase mode, they also allow excitation of multiple additional and undesirable modes. Various approaches to exclusively selecting the in-phase mode include spatially patterning loss to the undesirable modes and incorporating a built-in index profile.

6.4.2.1 Loss Patterning

Previous work has shown that a photonic crystal etch can provide sufficient modal discrimination to preferentially select the in-phase mode in 2x2 VCSEL arrays through rollover [46]. Similar photonic crystal designs have been incorporated in the next generation of bottom-emitting arrays. These patterns have the effect of both introducing loss to undesirable modes and of providing index guiding to reduce the lateral radiation loss common to antiguided arrays [68].

While the photonic crystal patterns primarily introduce loss to the higher order modes on the lateral edges of an array, another approach is to increase the optical loss in the interelement regions. This technique has been shown to significantly discriminate

against undesirable higher-order modes in both edge-emitting and VCSEL arrays [45, 70]. One approach taken in the design of the next generation of bottom-emitting VCSEL arrays is to refrain from depositing the top metal over the interelement regions. This is expected to reduce the reflectivity in these regions, thereby introducing additional loss. Another approach would be to carefully etch the interelement regions surrounding the thick, gold implant-blocking pillars. This self-aligned process could introduce significant optical loss if the top DBR was etched to an antiresonant thickness [45]. One drawback of this technique is that it would likely decrease the effective index in these regions [91], which is counter to the preferred antiguiding effect.

6.4.2.2 Built-In Antiguiding

A significant breakthrough for coherently-coupled edge-emitting laser arrays came with the introduction of a built-in antiguiding index profile, where the real index contrast between the element and interelement regions was on the order of 0.02 [96], as opposed to index contrast on the order of 0.003 for the previous gain-guided arrays [73]. While this is sufficient index contrast to achieve antiguiding, the index contrast is easily overcome by thermal variations in index that arise with increased current injection, where the thermo-optic effect can induce an index change across a device on the order of 0.007 [73]. Such gain-guided arrays are thus susceptible to modal instability with increased current [97].

One technique for increasing the index contrast is with ion implantation. Free carriers within a semiconductor contribute negatively to the semiconductor's refractive index. Proton implantation reduces the free carrier concentration within a semiconductor, thereby increasing its refractive index. The change in index produced by a given concentration of free carriers, N, can be obtained as [98]

$$\Delta n = \frac{-Ne^2}{2n\epsilon_0 m^* \omega^2} , \tag{6.1}$$

where ϵ_0 is the free-space dielectric constant, e is the electron charge, m^* is the effective mass of the carriers, and ω is the optical frequency. If the ion implant reduces the free carrier concentration in a region to $N_{implanted}$, the index contrast between the implanted and non-implanted layers is found as

$$\Delta n = n_{implanted} - n = \frac{\left(N - N_{implanted}\right)e^2}{2n\epsilon_0 m^* \omega^2} . \tag{6.2}$$

It is noted from Equation 6.2 that reducing $N_{implanted}$ beyond an order of magnitude below N has little further impact on Δn. An H^+ implant dose of $5 \cdot 10^{14}/cm^3$ at 300 keV into n-type GaAs with $N = 10^{18}$ cm^{-3} has been shown to provide a 3.5x reduction in $N_{implant}$ [99]. Given the parameters for $Al_xGa_{1-x}As$ shown in Table 6.1, the index contrast values are shown in Table 6.2 for varying doping types, densities and H^+ implant doses. The index contrast calculated for ion implantation in p-type DBRs is found to be small. The index contrast calculated for n-type DBRs is found to be 6x greater than this, due to the

smaller electron effective mass. If a stacked implant with doses of $1 \cdot 10^{15}/cm^3$ were performed on an n-type DBR with N = 3 x 10^{18} cm^{-3}, a $\Delta n_{implant}$ value greater than 0.003 could be attained. In this case, the built-in antiguiding effect would combine with the index suppression from current injection of $\Delta n_{carrier} \approx 0.004$ for a total index contrast of $\Delta n \approx 0.007$. An illustration of the combined index variations is shown in Figure 6.2. While this index contrast remains short of that desired for strong antiguiding, it should still enhance an array's modal discrimination by further securing the antiguided index profile against thermo-optic fluctuations.

Table 6.1. Parameters for $Al_xGa_{1-x}As$ [100].

parameter	value
x	0.53
m_e/m_0	0.111
mh/m_0	0.654
n	3.214

Table 6.2. Calculated refractive index contrast for varying doping types, densities and H^+ implant doses.

DBR doping	N_{DBR} (cm^{-3})	dose (H^+/cm^{-3})	Δn
p-type	2 x 10^{18}	5 x 10^{14}	0.00029
n-type	2 x 10^{18}	5 x 10^{14}	0.00173
p-type	3 x 10^{18}	10^{15}	0.00051
n-type	3 x 10^{18}	10^{15}	0.00302

It is noteworthy that the effects of implantation of H^+ ions into n-type GaAs have been shown to anneal out rapidly at temperatures above 300 ^oC, which is typically

reached during additional VCSEL processing steps [101]. Ion implantation with O^+ ions into n-type GaAs, for example, has shown much improved thermal stability, and may be a better option [101].

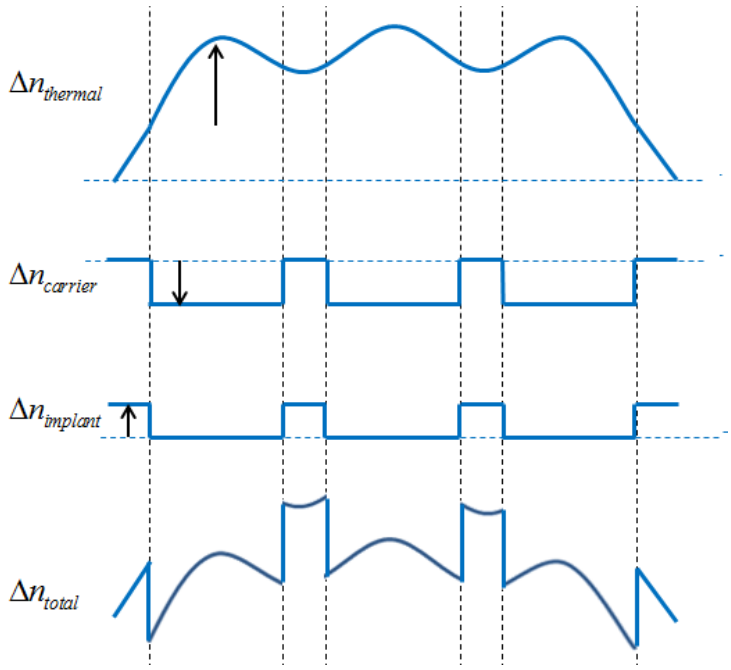

Figure 6.2: Index profile as totaled from thermal, carrier and ion implantation contributions.

One drawback that is often cited when considering the optical effects of ion implantation is the increased loss introduced in the ion-implanted regions [102], which can be mitigated with an annealing step. However, as mentioned earlier, introducing loss into the interelement regions is a standard way of preferentially selecting the in-phase mode [45, 70], and is especially important for larger arrays [103]. Interelement loss on the order of α =50-90 cm^{-1} has been shown to strongly suppress the out-of-phase and adjacent modes for a 10-element structure while having negligible effect on

the in-phase mode [70]. The primary drawback for ion-implanted waveguides thus turns out to be an advantage for ion-implanted antiguiding.

The key advantages to this approach then include its simplicity, self-alignment, and the introduction of optical loss into the interelement regions. The approach does not require any additional fabrication processes of significance. Additionally, the self-alignment allowed by the thick gold mask layer ensures that the gain directly overlaps the regions of lower index, and that the regions of increased optical loss directly overlap the interelement regions.

6.5 Array Scaling

Large top-emitting in-phase arrays of up to 10x10 elements have been shown [45]. However, a difficult regrowth and phase-matching fabrication process was required, and the total output power was thermally limited to < 2 mW. Our group has demonstrated in-phase 2x2 arrays with a simple fabrication process, but efforts to scale this beyond two elements in either direction have been hampered by problems with current uniformity. We have shown bottom-emitting arrays to offer significantly improved current uniformity (Figure 5.6), which is expected to allow scaling to large array sizes. Further, stronger coupling and decreased lateral radiation losses are expected for larger antiguided arrays due to the parallel coupling between all elements.

Appendix A: FRAUNHOFER PROPAGATION CODE

The program below simulates the propagation of a given near field pattern to the far field, based on the Fraunhofer approximation. The code allows simulation of up to a 4x4 array of near-field elements, each with their own relative amplitude and phase. The pitch, diameter and many other variables can also be set. These parameters are set in an Excel file which is read in by the MATLAB code. This allows making multiple sheets for various designs while using the same code. A new sheet in the excel file can be created and the *sheet* variable assigned in the MATLAB code can be updated accordingly.

In order to use this code, the propagation script, Fraunhofer function, and Excel file with both sheets would have to be saved in the same directory. Arrays with fewer than 4x4 elements can be simulated by setting non-essential element amplitudes to zero, and larger arrays would require some modifications. Propagating the experimentally-determined near field to the far field, as performed in this thesis, is based on the same code. For example, the near-field amplitude images in Figure 4.1 could be imported into MATLAB, separated into two or three apertures, assigned the appropriate phase and coherence, and then *propagated* with the code below to acquire the corresponding far field images also shown in Figure 4.1.

A.1 Propagation Script

```
%%%%%%%%%%%%%%%%%%%%%%%%%%%%%%%%%%%%%%%%%%%%%%%%%%%%%%%%%%%%%%%%%%%%%%%%%
% VCSEL array model
% Simulating far field from array of near-field Gaussian sources aligned in hexaganol pattern as defined by parameters in excel file
% OUTPUTS:
% Intensity_Normalized_Phi          (far field intensity)
% Z_both                            (intensity profile from far-field slice)
%%%%%%%%%%%%%%%%%%%%%%%%%%%%%%%%%%%%%%%%%%%%%%%%%%%%%%%%%%%%%%%%%%%%%

% DEFINING SOME INITIAL VALUES
clear all;
ext='';
column = 2;
filename_data = 'variables.xlsx';   % name of file containing simulation parameters
num_var = 26;   % number of variable parameters in excel document, have to update this number if you add another variable
sheet=10;       % sheet the excel data is on
plot_style_vec = {'b';':r';'--c';'-.m'};    % linestyles to plot
legend_vec = {'4';'3';'2';'1'};             % strings to plot in legend

% READING IN PARAMETERS FROM EXCEL FILE
[num,txt,raw] = xlsread(filename_data,sheet,['A2:B',num2str(num_var+1)]); % pulling parameters from excel
vars=genvarname(raw(1:num_var,1));   % assigning values to variable names defined in excel file
for ii=1:length(vars)
   str=char(vars(ii));
   eval([str '=num(ii,1)'])
end;

% OBTAINING INTENSITY AND PHASE MAP
[num1,txt1,raw1] = xlsread(filename_data,map_sheet,'A1:H16');  %intensity/phase info in different sheet

% DEFINING/INITIALIZING OTHER VARIABLES
N_theta = ceil(theta_sim*N/500);
FWHMs=zeros(1,map_N);
Intensity_max=zeros(1,map_N);

% INITIATING LOOP TO GO THROUGH MULTIPLE INTENSITY/PHASE MAPS
for NN=1:map_N;
   Amp = num1((NN-1)*10+1:(NN-1)*10+map_dim,1:map_dim);    % intensity and phase maps offset by 10 rows
   Phi = num1((NN-1)*10+map_dim+2:(NN-1)*10+2*map_dim+1,1:map_dim);
   plot_style=char(plot_style_vec(NN));
   fignum = (NN-1)*10;           % different figure numbers for different maps
   if NN > 1
      cleared = 0;
   end;

   % GAUSSIAN VALUES %
   FWHM = FWHM_perc*dia;       % full width half maximum
   c_beam = FWHM/2.35482;      % beam waist
   k = 2*pi/lambda;            % wave vector

   % SAMPLE AND DETECTOR GRIDS %
   grid_size = N*dx;          % number of pixels in one dimension times pixel width
   [xs ys] = meshgrid((-N/2:N/2-1).*dx);   % defining near field grid
   dx_det = lambda*z/grid_size;       % far field pixel width
   [x_det y_det] = meshgrid((-N/2:N/2-1).*dx_det); % defining far field grid

   % INITIALIZING APERTURES %
   U_ap_total = zeros(N);
   U_total_Phi = zeros(N);
   Intensity_total_incoh = zeros(N);
   for ii = 1:7
      for jj = 1:7
         U_ap(:,:,ii,jj) = zeros(N); %setting near field matrices to zero
         U(:,:,ii,jj) = zeros(N);    %setting far field matrices to zero
      end;
   end;
```

```
% Assigning Gaussian values to apertures with corresponding amplitude/phase
for ii = 1:7
   for jj = 1:7
      if mod(jj,2) == 0    % if ii is even
         U_ap(:,:,ii,jj) = Amp(ii,jj)*exp(-((xs-(jj-1)*x_pitch).^2 ...
         + (ys-(ii*2-1)*y_pitch/2).^2)/(2*c_beam^2))*exp(i*Phi(ii,jj));
      else              % if ii is odd
         U_ap(:,:,ii,jj) = Amp(ii,jj)*exp(-((xs-(jj-1)*x_pitch).^2 ...
         + (ys-(ii-1)*y_pitch).^2)/(2*c_beam^2))*exp(i*Phi(ii,jj));
      end;
   end;
end;

for ii = 1:7
   for jj = 1:7
      U(:,:,ii,jj) = Fraunhoffer(U_ap(:,:,ii,jj), k, z, x_det, y_det, lambda);
      U_ap_total = U_ap_total + U_ap(:,:,ii,jj);
      U_total_Phi = U_total_Phi+U(:,:,ii,jj);
      Intensity_total_incoh = Intensity_total_incoh + (abs(U(:,:,ii,jj)).^2);
   end;
end;

%ADDING COMPLEX FIELDS AND SOLVING FOR FAR FIELD INTENSITY
% from Equations 2.2-2.5
Intensity_total_coh = U_total_Phi.^2;
Intensity_total_Phi = (1-coh)*Intensity_total_incoh + coh*...
   Intensity_total_coh;
% normalizing intensity
Intensity_normalized_Phi = Intensity_total_Phi/max(max(Intensity_total_Phi));

% PLOTTING NEAR AND FAR FIELDS
angle_x = atan(x_det/z)*360/(2*pi); %translating to angular values
angle_y = atan(y_det/z)*360/(2*pi);

% PLOT NEAR FIELD
Fig2 = figure(2+fignum);
if cleared == 1
   clf;
end;
set(Fig2, 'Position', [30 400 250 200]); colormap(jet);
surf(xs*10^6,-ys*10^6, real(U_ap_total),...
'LineStyle','none','FaceColor','interp',...
'FaceLighting','phong','AmbientStrength',0.3);
shading flat;
axis([x_ap_min x_ap_max y_ap_min y_ap_max]);  % setting axis limits
caxis([0 1]);
set(gca,'dataaspectratio',[1,1,1]);
grid off; view([0 90]);
xlabel('\mum','FontSize',fs,'FontName','Calibri');
ylabel('\mum','FontSize',fs,'FontName','Calibri');
set(gcf,'PaperPositionMode','auto');

% PLOT FAR FIELD
Fig3 = figure(8+column+fignum); clf;
set(Fig3, 'Position', [300+50*(column-1) 400 200 150]);
surf(angle_x, -angle_y, abs(Intensity_normalized_Phi),...
'LineStyle','none','FaceColor','interp','FaceLighting','phong',...
'AmbientStrength',0.3), shading flat;
axis([-theta_sim theta_sim -theta_sim theta_sim 0 1]); % setting axis limits
set(gca,'Visible','off','plotboxaspectratio',[1,1,3]);
camva(3);
grid off;
view([0 90]);
% adding 10 degree circle and cut line
hold on;
   x1=0:pi/500:10;
   t=ones(1,length(x1));
   plot3(theta_circle*cos(x1),theta_circle*sin(x1),t,'r','LineWidth',2);
   text(0.8*theta_circle,0.8*theta_circle,1,[num2str(theta_circle),'°'],'Color','r','FontSize',fs);
```

```
        if plot_cutline == 1   % plots line along slice angle
            plot3(0,0,1,'.k');
            plot3(x1,x1*tan(angcut*2*pi/360),t,'k','Linewidth',2);
            plot3(-x1,-x1*tan(angcut*2*pi/360),t,'k','Linewidth',2);
        end;
    hold off;

    % PLOT FAR FIELD INTENSITY SLICE
    % Plots intensity along slice angle
    Fig8 = figure(8);
    set(Fig8, 'Position', [10 10 500 300]);
    if cleared == 1
        clf;
    end;
    hold on;
    % interpolating to find values along cut
    point1 = [0; 0];
    point2 = [theta_circle; theta_circle*tan(-angcut*2*pi/360)];
    t = 0:1/(N_theta):1;
    xi = point2(1)*t+point1(1)*(1-t);
    yi = point2(2)*t+point1(2)*(1-t);
    Z_interp1=interp2(angle_x,angle_y,abs(Intensity_normalized_Phi),xi,yi);
    Z_interp2=interp2(angle_x,angle_y,abs(Intensity_normalized_Phi),-xi,-yi);
    xyi_both(N_theta+1:-1:1)=-sqrt(xi.^2+yi.^2);
    xyi_both(N_theta+2:2*(N_theta+1)-1)=sqrt(xi(2:N_theta+1).^2+yi(2:N_theta+1).^2);
    Z_both(N_theta+1:-1:1)=Z_interp2;
    Z_both(N_theta+2:2*(N_theta+1)-1)=Z_interp1(2:N_theta+1);
    plot(xyi_both,Z_both,plot_style,'linewidth',2);
    axis([-theta_sim*sim_trim theta_sim*sim_trim 0 1]);
    figure(8);
    xlabel('angle(\circ)','FontSize',fs,'FontName','Calibri');
    ylabel('Intensity (a.u.)','FontSize',fs,'FontName','Calibri');
    if plot_legend == 1
        legend(legend_vec);
    end;
end;
```

A.2 Fraunhofer Function

```
function [U_det] = Fraunhofer(U_ap, k, z, xs, ys, lambda)
%%%%%%%%%%%%%%%%%%%%%%%%%%%%%%%%%%%%%%%%%%%%%%%%%%%%%%%%%%%%%%%%%%%%%%%%%%%%%%%%%%%
% Fraunhofer
% Translates Near Field (U_ap) to Far Field (U_det)
% (assuming various Fraunhofer assumptions are valid)
% INPUTS:
% U_ap        (Field at aperture)
%
% OUTPUTS:
% U_det       (Field at detector)
%%%%%%%%%%%%%%%%%%%%%%%%%%%%%%%%%%%%%%%%%%%%%%%%%%%%%%%%%%%%%%%%%%%%%%%%%%%%%%%%%
Angular_Spectrum = fftshift(fft2(fftshift(U_ap))); %Near Field
U_det = exp(i*k*z)*exp(i*k*(xs.^2+ys.^2)/(2*z)).*Angular_Spectrum...
    /(i*lambda*z);
End
```

A.3 Example Sheet 1

variable	value	notes
plot_cutline	0	
plot_percentage	0.000	
plot_legend	0	plot legend?
map_sheet	8.000	sheet the intensity and phase maps are on
map_period	10.000	how many rows between different sets of intensity/phase
map_N	7.000	how many sets of intensity/phase to go through
map_dim	7.000	how many elements in each dimension
FWHM_perc	0.589	full width half maximum proportional to diameter
lambda	808E-09	wavelength in meters
dia	124.8E-06	diameter of near-field Gaussian beams
x_pitch	175.5E-06	distance btween elements
y_pitch	0.000157	
N	2500.000	# of pixels in each dimension (fidelity and processing time)
dx	5E-06	width of each pixel
z	1000000	distance from near to far field
coh	0.9	coherence magnitude
y_ap_min	-1200	for plotting near field
y_ap_max	200	for plotting near field
x_ap_min	-200.000	for plotting near field
x_ap_max	1200.000	for plotting near field
theta_sim	0.500	axis limit for far-field plot
theta_circle	0.290	reference circle angle
angcut	0.000	angle to take far-field intensity slice from
cleared	1.000	to initially reset figures
sim_trim	0.600	proportion of theta_sim to show in intensity slice axis
fs	13.000	font size

A.4 Example Sheet 2

Amplitude	**T**	**U**	**V**	**W**	**X**	**Y**	**Z**	**notes**
A	0	0	0	0.2	0	0	0	maximum amplitude of each element
B	0	0.2	0.2	0.7	0.2	0.2	0	
C	0.1	0.5	0.7	0.9	0.7	0.5	0.1	
D	0.2	0.6	0.9	1	0.9	0.6	0.2	
E	0.2	0.5	0.9	0.9	0.9	0.5	0.2	
F	0.1	0.1	0.5	0.5	0.5	0.1	0.1	
G	0	0	0.1	0.1	0.1	0	0	
Phase	**T**	**U**	**V**	**W**	**X**	**Y**	**Z**	
A	0	0	0	0	0	0	0	phase of each element
B	0	0	0	0	0	0	0	
C	0	0	0	0	0	0	0	
D	0	0	0	0	0	0	0	
E	0	0	0	0	0	0	0	
F	0	0	0	0	0	0	0	
G	0	0	0	0	0	0	0	

APPENDIX B: PHASE SHIFT DERIVATION

This appendix provides a thorough derivation of the correlation between the resonant frequency detuning between two coupled elements and their associated temporal phase shift. The time-dependent electric field of element m is defined as $E_m(t) = A_m(t)e^{-i\phi_m(t)}$, where A_m is the field amplitude and ϕ_m is the phase. The time change of the electric field under the influence of neighboring elements, E_{m-1} and E_{m+1}, is governed by the field equation [78]

$$\frac{dE_m}{dt} = \frac{1}{2}\left[G(N_m) - \frac{1}{\tau_p}\right](1 - i\alpha)E_m + i\kappa\left(E_{m+1} + E_{m-1}\right)e^{-i\psi} + i(\omega_0 - \omega_m)E_m, \quad \text{(B.1)}$$

where G is the gain, N is the carrier density, τ_p is the photon lifetime, α is the linewidth enhancement factor, κ is the coupling strength between elements, ψ is the coupling phase (typically 0 or π), ω_0 is the coupling frequency and ω_m is the native frequency of element m. If the laser element is operating near threshold, the gain can be expressed as

$$G(N_m) = G(N_{th}) + g(N_m - N_{th}),$$

where N_{th} is the threshold carrier density and g is the differential gain. With the threshold gain defined as that required to overcome the loss, or $G(N_{th}) = 1/\tau_p$, Equation 2.7 can be expressed as

$$\frac{dE_m}{dt} = \frac{1}{2}\left[g\left(N_m - N_{th}\right)\right](1 - i\alpha)E_m + i\kappa\left(E_{m+1} + E_{m-1}\right)e^{-i\psi} + i\left(\omega_0 - \omega_m\right)E_m . \qquad \text{(B.2)}$$

In order to solve for the dimensionless, normalized, time-dependent amplitude and phase, we use the following substitutions [104]:

$$X_m = \left(\frac{1}{2}g\tau_s\right)^{\frac{1}{2}}\left|E_m\right|,$$

$$Z_m = \frac{1}{2}gN_{th}\tau_p\left(\frac{N_m}{N_{th}} - 1\right),$$

$\eta = \kappa\tau_p$, and

[ ].

We first expand the electric field into amplitude and phase components as $E_m = A_m(t)e^{-i\phi_m(t)}$ to obtain

$$\frac{d\left(A_m(t)e^{-i\phi_m(t)}\right)}{dt} = A_m\frac{d\left(e^{-i\phi_m(t)}\right)}{dt} + e^{-i\phi_m(t)}\frac{d\left(A_m(t)\right)}{dt} = -iA_m e^{-i\phi_m(t)}\frac{d\phi_m(t)}{dt} + e^{-i\phi_m(t)}\frac{d\left(A_m(t)\right)}{dt}.$$

We then substitute this expansion into B.2 to yield

$$-iA_m e^{-i\phi_m(t)}\frac{d\phi_m(t)}{dt} + e^{-i\phi_m(t)}\frac{d\left(A_m(t)\right)}{dt} = \frac{1}{2}\left[g\left(N_m - N_{th}\right)\right](1 - i\alpha)A_m e^{i\phi_m(t)} + i\kappa\left(A_{m+1}e^{-i\phi_{m+1}(t)} + A_{m-1}e^{-i\phi_{m+1}(t)}\right)e^{-i\psi} + i\left(\omega_0 - \omega_m\right)A_m e^{-i\phi_m(t)}.$$

We further expand the equation with the normalization substitutions to obtain

$$-iX_m\left(\frac{1}{2}g\tau_s\right)^{-\frac{1}{2}}e^{-i\phi_m(t)}\frac{d\phi_m(t)}{dt}+\left(\frac{1}{2}g\tau_s\right)^{-\frac{1}{2}}e^{-i\phi_m(t)}\frac{d\left(X_m(t)\right)}{dt}=\frac{Z_m}{\tau_p}(1-i\alpha)X_m\left(\frac{1}{2}g\tau_s\right)^{-\frac{1}{2}}e^{-i\phi_m(t)}+$$
$$i\kappa\left(X_{m+1}\left(\frac{1}{2}g\tau_s\right)^{-\frac{1}{2}}e^{-i\phi_{m+1}(t)}+X_{m-1}\left(\frac{1}{2}g\tau_s\right)^{-\frac{1}{2}}e^{-i\phi_{m-1}(t)}\right)e^{-i\psi}+i\left(\omega_0-\omega_m\right)X_m\left(\frac{1}{2}g\tau_s\right)^{-\frac{1}{2}}e^{-i\phi_m(t)},$$

where the normalization parameters cancel out, and we are left with

$$-iX_me^{-i\phi_m}\frac{d\phi_m}{dt}+e^{-i\phi_m(t)}\frac{dX_m}{dt}=\frac{Z_m}{\tau_p}(1-i\alpha)X_me^{-i\phi_m}-i\kappa\left(X_{m+1}e^{-i\phi_{m+1}}+X_{m-1}e^{-i\phi_{m+1}}\right)e^{-i\psi}$$
$$+i\left(\omega_0-\omega_m\right)X_me^{-i\phi_m}.$$

We can then move the exponentials together on the right side

$$-iX_m\frac{d\phi_m}{dt}+\frac{dX_m}{dt}=\frac{Z_m}{\tau_p}(1-i\alpha)X_me^{-i\phi_m}e^{i\phi_m}+i\kappa\left(X_{m+1}e^{-i\phi_{m+1}}+X_{m-1}e^{-i\phi_{m+1}}\right)e^{-i\psi}e^{i\phi_m}$$
$$+i\left(\omega_0-\omega_m\right)X_me^{-i\phi_m}e^{i\phi_m},$$
$$=\frac{Z_m}{\tau_p}(1-i\alpha)X_m+i\kappa\left(X_{m+1}e^{i(-\phi_{m+1}+\phi_m-\psi)}+X_{m-1}e^{i(-\phi_{m-1}+\phi_m-\psi)}\right)+i\left(\omega_0-\omega_m\right)X_m$$

and break the exponentials into real and imaginary components, yielding

$$iX_m\frac{d\phi_m}{dt}+\frac{dX_m}{dt}=\frac{Z_m}{\tau_p}(1-i\alpha)X_m+$$
$$i\kappa\begin{pmatrix}X_{m+1}\left[\cos\left(-\phi_{m+1}+\phi_m-\psi\right)+i\sin\left(-\phi_{m+1}+\phi_m-\psi\right)\right]+\\X_{m-1}\left[\cos\left(-\phi_{m-1}+\phi_m-\psi\right)+i\sin\left(-\phi_{m-1}+\phi_m-\psi\right)\right]\end{pmatrix}+i\left(\omega_0-\omega_m\right)X_m.$$

The equation can then be separated into its real and imaginary components to yield the time-dependent amplitude and phase

$$\frac{dX_m}{dt} = \frac{Z_m}{\tau_p} X_m - \kappa\left(X_{m+1}\sin\left(\phi_m - \phi_{m+1} - \psi\right) + X_{m-1}\sin\left(\phi_m - \phi_{m-1} - \psi\right)\right),$$

$$-iX_m \frac{d\phi_m}{dt} = -i\alpha \frac{Z_m}{\tau_p} X_m + i\kappa\left[X_{m+1}\cos\left(\phi_m - \phi_{m+1} - \psi\right) + X_{m-1}\cos\left(\phi_m - \phi_{m-1} - \psi\right)\right] + i\left(\omega_0 - \omega_m\right)X_m,$$

$$\text{and } \frac{d\phi_m}{dt} = \frac{\alpha Z_m}{\tau_p} - \kappa\left[\frac{X_{m+1}}{X_m}\cos\left(\phi_m - \phi_{m-1} - \psi\right) + \frac{X_{m-1}}{X_m}\cos\left(\phi_m - \phi_{m-1} - \psi\right)\right] + \frac{\Delta_m}{\tau_p}.$$

And finally, the derivatives can be normalized to a reduced time t/τ_p as

$$\frac{dX_m}{dt/\tau_p} = Z_m X_m - \eta\left(X_{m+1}\sin\left(\phi_m - \phi_{m+1} - \psi\right) + X_{m-1}\sin\left(\phi_m - \phi_{m-1} - \psi\right)\right), \text{ and} \qquad \text{(B.3)}$$

$$\frac{d\phi_m}{dt/\tau_p} = \alpha Z_m - \eta\left[\frac{X_{m+1}}{X_m}\cos\left(\phi_m - \phi_{m-1} - \psi\right) + \frac{X_{m-1}}{X_m}\cos\left(\phi_m - \phi_{m-1} - \psi\right)\right] + \Delta_m. \qquad \text{(B.4)}$$

At steady state, Equation B.4 yields

$$\frac{\alpha Z_m + \Delta_m}{\eta} = \left(X_{m+1}/X_m\right)\cos\left(\phi_m - \phi_{m+1} - \psi\right) + \left(X_{m-1}/X_m\right)\cos\left(\phi_{m-1} - \phi_m - \psi\right).$$

For a 2x1 array comprised of elements 1 and 2, this yields the following equations:

$$\frac{\alpha Z_1 + \Delta_1}{\eta} = \left(X_2/X_1\right)\cos\left(\phi_1 - \phi_2 - \psi\right),$$

$$\frac{\alpha Z_2 + \Delta_2}{\eta} = \left(X_1/X_2\right)\cos\left(\phi_1 - \phi_2 - \psi\right),$$

$$\alpha Z_1 = \eta\left(X_2/X_1\right)\cos\left(\phi_1 - \phi_2 - \psi\right) - \Delta_1, \text{ and} \qquad \text{(B.5)}$$

$$\alpha Z_2 = \eta\left(X_1 / X_2\right)\cos\left(\phi_1 - \phi_2 - \psi\right) - \Delta_2 . \tag{B.6}$$

Equations B.5 and B.6 can then be combined to obtain

$$\alpha\left(Z_2 - Z_1\right) = \eta\left(X_1 / X_2\right)\cos\left(\phi_1 - \phi_2 - \psi\right) - \eta\left(X_2 / X_1\right)\cos\left(\phi_1 - \phi_2 - \psi\right) - \Delta_2 + \Delta_1 ,$$

$$-\Delta_2 + \Delta_1 = -\left(\omega_0 - \omega_2\right)\tau_p + \left(\omega_0 - \omega_1\right)\tau_p = \left(\omega_2 - \omega_1\right)\tau_p \text{, and}$$

$$\alpha\left(Z_2 - Z_1\right) = \eta\left(X_1 / X_2 - X_2 / X_1\right)\cos\left(\phi_1 - \phi_2 - \psi\right) + \left(\omega_2 - \omega_1\right)\tau_p . \tag{B.7}$$

At steady state, equation B.3 is reduced to

$$0 = Z_m X_m - \eta\left[X_{m+1}\sin\left(\phi_m - \phi_{m+1} - \psi\right) + X_{m-1}\sin\left(\phi_m - \phi_{m+1} - \psi\right)\right] \text{, and}$$

$$Z_m X_m = \eta\left[X_{m+1}\sin\left(\phi_m - \phi_{m+1} - \psi\right) + X_{m-1}\sin\left(\phi_m - \phi_{m+1} - \psi\right)\right].$$

For a 2x1 array comprised of elements 1 and 2, this yields

$$Z_1 X_1 = \eta\left[X_2\sin\left(\phi_1 - \phi_2 - \psi\right)\right],$$

$$Z_2 X_2 = -\eta\left[X_1\sin\left(\phi_1 - \phi_2 - \psi\right)\right],$$

$$Z_1 = \eta\left[\frac{X_2}{X_1}\sin\left(\phi_1 - \phi_2 - \psi\right)\right] \text{, and} \tag{B.8}$$

$$Z_2 = -\eta\left[\frac{X_1}{X_2}\sin\left(\phi_1 - \phi_2 - \psi\right)\right]. \tag{B.9}$$

Substituting B.8 and B.9 into B.7, we find

$$\alpha\left(-\eta\left[\frac{X_1}{X_2}\sin\left(\phi_1-\phi_2-\psi\right)\right]-\eta\left[\frac{X_2}{X_1}\sin\left(\phi_1-\phi_2-\psi\right)\right]\right)=\eta\left(\frac{X_1}{X_2}-\frac{X_2}{X_1}\right)\cos\left(\phi_1-\phi_2-\psi\right)+\left(\omega_2-\omega_1\right)\tau_p,$$

$$-\alpha\left(\left[\frac{X_1}{X_2}\sin\left(\phi_1-\phi_2-\psi\right)\right]+\left[\frac{X_2}{X_1}\sin\left(\phi_1-\phi_2-\psi\right)\right]\right)=\left(\frac{X_1}{X_2}-\frac{X_2}{X_1}\right)\cos\left(\phi_1-\phi_2-\psi\right)+\frac{\left(\omega_2-\omega_1\right)\tau_p}{\eta},$$

$$\frac{\left(\omega_2-\omega_1\right)\tau_p}{\eta}=-\alpha\left(\left[\frac{X_1}{X_2}\sin\left(\phi_1-\phi_2-\psi\right)\right]+\left[\frac{X_2}{X_1}\sin\left(\phi_1-\phi_2-\psi\right)\right]\right)-\left(\frac{X_1}{X_2}-\frac{X_2}{X_1}\right)\cos\left(\phi_1-\phi_2-\psi\right),$$

and $$\frac{\left(\omega_2-\omega_1\right)\tau_p}{\eta}=-\alpha\left(\frac{X_1}{X_2}+\frac{X_2}{X_1}\right)\sin\left(\phi_1-\phi_2-\psi\right)-\left(\frac{X_1}{X_2}-\frac{X_2}{X_1}\right)\cos\left(\phi_1-\phi_2-\psi\right).$$

From this we finally arrive at our equation correlating the resonant frequency detuning between the elements and their relative amplitudes and phases, as

$$\omega_2-\omega_1=-\kappa\left[\alpha\left(\frac{X_1}{X_2}+\frac{X_2}{X_1}\right)\sin\left(\phi_1-\phi_2-\psi\right)+\left(\frac{X_1}{X_2}-\frac{X_2}{X_1}\right)\cos\left(\phi_1-\phi_2-\psi\right)\right].$$

We can also solve for native resonant frequencies of element 1 from Equations B.5 and B.8 as

$$\alpha Z_1=\eta\left(X_2/X_1\right)\cos\left(\phi_1-\phi_2-\psi\right)-\Delta_1,$$

$$\left(\omega_{coupled}-\omega_1\right)\tau_p=\eta\left(X_2/X_1\right)\cos\left(\phi_1-\phi_2-\psi\right)-\alpha Z_1,$$

$$\omega_{coupled}-\omega_1=\frac{1}{\tau_p}\left(\eta\left(X_2/X_1\right)\cos\left(\phi_1-\phi_2-\psi\right)-\alpha Z_1\right),$$

$$\omega_{coupled} - \omega_1 = \frac{1}{\tau_p}\left(\eta\frac{X_2}{X_1}\cos\left(\phi_1 - \phi_2 - \psi\right) - \alpha\eta\left[\frac{X_2}{X_1}\sin\left(\phi_1 - \phi_2 - \psi\right)\right]\right),$$

$$\omega_{coupled} - \omega_1 = \kappa\left(\frac{X_2}{X_1}\cos\left(\phi_1 - \phi_2 - \psi\right) - \alpha\left[\frac{X_2}{X_1}\sin\left(\phi_1 - \phi_2 - \psi\right)\right]\right),$$

$$-\omega_1 = -\omega_{coupled} + \mathrm{K}\left(\frac{X_2}{X_1}\cos\left(\phi_1 - \phi_2 - \psi\right) - \alpha\left[\frac{X_2}{X_1}\sin\left(\phi_1 - \phi_2 - \psi\right)\right]\right), \text{ and}$$

$$\omega_1 = \omega_{coupled} - \mathrm{K}\frac{X_2}{X_1}\left(\cos\left(\phi_1 - \phi_2 - \psi\right) - \alpha\left[\sin\left(\phi_1 - \phi_2 - \psi\right)\right]\right).$$

Similarly, ω_2 can be obtained from Equations B.6 and B.9 as

$$\omega_2 = \omega_{coupled} - \kappa\frac{X_1}{X_2}\left[\cos\left(\phi_1 - \phi_2 - \psi\right) + \alpha\sin\left(\phi_1 - \phi_2 - \psi\right)\right].$$

REFERENCES

[1] P. F. McManamon, P. J. Bos, M. J. Escuti, J. Heikenfeld, S. Serati, H. Xie and E. A. Watson, "A review of phased array steering for narrow-band electrooptical systems," *Proc IEEE,* vol. 97, pp. 1078-1096, 2009.

[2] R. Meyer, "Optical beam steering using a multichannel lithium tantalate crystal," *Appl. Opt.,* vol. 11, pp. 613-616, 1972.

[3] A. Fray and D. Jones, "Large-angle beam deflector using liquid crystals," *Electron. Lett.,* vol. 11, pp. 358-359, 1975.

[4] P. F. McManamon, T. A. Dorschner, D. L. Corkum, L. J. Friedman, D. S. Hobbs, M. Holz, S. Liberman, H. Q. Nguyen, D. P. Resler and R. C. Sharp, "Optical phased array technology," *Proc IEEE,* vol. 84, pp. 268-298, 1996.

[5] A. Tuantranont, V. Bright, J. Zhang, W. Zhang, J. Neff and Y. Lee, "Optical beam steering using MEMS-controllable microlens array," *Sensors and Actuators A: Physical,* vol. 91, pp. 363-372, 2001.

[6] U. Krishnamoorthy, K. Li, K. Yu, D. Lee, J. Heritage and O. Solgaard, "Dual-mode micromirrors for optical phased array applications," *Sensors and Actuators A: Physical,* vol. 97, pp. 21-26, 2002.

[7] W. Guo, P. Binetti, C. Althouse, H. Ambrosius, L. Johansson and L. A. Coldren, "Improved performance of optical beam steering through an InP photonic integrated circuit," in *CLEO: Science and Innovations,* 2012.

[8] N. R. Smith, D. C. Abeysinghe, J. W. Haus and J. Heikenfeld, "Agile wide-angle beam steering with electrowetting microprisms," *Opt. Express,* vol. 14, pp. 6557-6563, 2006.

[9] J. Bae, Y. Choi, K. Choi, Y. Kim, Y. Kwon, H. Song, E. Kim, S. Choi, J. Lee and S. Lee, "Arrayed beam steering device for advanced 3D displays," in *SPIE MOEMS-MEMS,* 2013.

[10] W. R. Huang, J. Montoya, J. E. Kansky, S. M. Redmond, G. W. Turner and A. Sanchez-Rubio, "High speed, high power one-dimensional beam steering from a 6-element optical phased array," *Opt. Express,* vol. 20, pp. 17311-17318, 2012.

[11] X. Gu, T. Shimada, A. Fuchida, A. Matsutani, A. Imamura and F. Koyama, "Ultra-compact beam-steering device based on Bragg reflector waveguide amplifier with number of resolution points over 100," *Electron. Lett.,* vol. 48, pp. 336-337, 2012.

[12] M. Jarrahi, R. F. W. Pease, D. A. B. Miller and T. H. Lee, "Optical switching based on high-speed phased array optical beam steering," *Appl. Phys. Lett.,* vol. 92, pp. 014106-014106-3, 2008.

[13] T. Ide, M. Shimizu, S. Mukai, M. Ogura, T. Kikuchi, Y. Suzuki, R. Kaji, H. Itoh, M. Watanabe and H. Yajima, "Continuous output beam steering in vertical-cavity surface-emitting lasers with two p-type electrodes by controlling injection current profile," *Jpn. J. Appl. Phys,* vol. 38, pp. 1966, 1999.

[14] D. F. Siriani and K. D. Choquette, "Electronically controlled two-dimensional steering of in-phase coherently coupled vertical-cavity laser arrays," *IEEE Photon. Technol. Lett.,* vol. 23, pp. 167-169, 2011.

[15] M. I. Cohen, A. A. Allerman, K. D. Choquette and C. Jagadish, "Electrically steerable lasers using wide-aperture VCSELs," *IEEE Photon. Technol. Lett.,* vol. 13, pp. 544-546, 2001.

[16] G. D. Love, A. K. Kirby and R. A. Ramsey, "Sub-millisecond, high stroke phase modulation using polymer network liquid crystals," *Opt. Express,* vol. 18, pp. 7384-7389, 2010.

[17] J. Sun, R. A. Ramsey, Y. Chen and S. T. Wu, "Submillisecond-response sheared polymer network liquid crystals for display applications," *Display Technology, Journal Of,* vol. 8, pp. 87-90, 2012.

[18] X. Dong, P. LiKamWa, J. Loehr and R. Kaspi, "Current-induced guiding and beam steering in active semiconductor planar waveguide," *IEEE Photon. Technol. Lett.,* vol. 11, pp. 809-811, 1999.

[19] J. Doylend, M. Heck, J. Bovington, J. Peters, M. Davenport, L. Coldren and J. Bowers, "Hybrid III/V silicon photonic source with integrated 1D free-space beam steering," *Opt. Lett.*, vol. 37, pp. 4257-4259, 2012.

[20] B. Lucke, G. Hergenhan, U. Branch and A. Giesen, "Phase tuning of injection-locked VCSELs," *IEEE Photon. Technol. Lett.,* vol. 13, pp. 100-102, 2001.

[21] S. Kobayashi and T. Kimura, "Optical phase modulation in an injection locked AlGaAs semiconductor laser," *Microwave Theory and Techniques, IEEE Transactions On,* vol. 30, pp. 1650-1657, 1982.

[22] J. F. Seurin, C. L. Ghosh, V. Khalfin, A. Miglo, G. Xu, J. D. Wynn, P. Pradhan and L. A. D'Asaro, "High-power high-efficiency 2D VCSEL arrays," in *Proceedings of SPIE - the International Society for Optical Engineering,* 2008.

[23] D. Richardson, J. Nilsson and W. Clarkson, "High power fiber lasers: current status and future perspectives [Invited]," *J. Opt. Soc. Am. B,* vol. 27, pp. B63-B92, 2010.

[24] J. Walker, D. Kuchta and J. Smith, "Vertical-cavity surface-emitting laser diodes fabricated by phase-locked epitaxy," *Appl. Phys. Lett.,* vol. 59, pp. 2079-2081, 1991.

[25] F. H. Peters, M. G. Peters, D. B. Young, J. W. Scott, B. J. Thibeault, S. W. Corzine and L. A. Coldren, "High-power vertical-cavity surface-emitting lasers," *Electron. Lett.,* vol. 29, pp. 200-201, 1993.

[26] R. Michalzik, M. Grabherr and K. J. Ebeling, "High-power VCSELs: Modeling and experimental characterization," in *Optoelectronics and High-Power Lasers & Applications,* 1998.

[27] M. Grabherr, R. Jäger, M. Miller, C. Thalmaier, J. Heerlein, R. Michalzik and K. J. Ebeling, "Bottom-emitting VCSEL's for high-CW optical output power," *IEEE Photon. Technol. Lett.,* vol. 10, pp. 1061-1063, 1998.

[28] D. Francis, H. Chen, W. Yuen, G. Li and C. Chang-Hasnain, "Monolithic 2D-VCSEL array with >2W CW and > 5W pulsed output power," *Electron. Lett.,* vol. 34, pp. 2132-2133, 1998.

[29] J. Seurin, L. A. D'Asaro and C. Ghosh, "A new application for VCSELs high-power pump lasers," *Photonics Spectra,* vol. 41, pp. 66-71, 2007.

[30] M. Grabherr, B. Weigl, G. Reiner, R. Michalzik, M. Miller and K. J. Ebeling, "High power top-surface emitting oxide confined vertical-cavity laser diodes," *Electron. Lett.,* vol. 32, pp. 1723-1724, 1996.

[31] M. Grabherr, M. Miller, R. Jager and K. Ebeling, "Efficient bottom-emitting VCSEL arrays for high CW optical output power," *Electron. Lett.,* vol. 34, pp. 1227-1228, 1998.

[32] M. Miller, M. Grabherr, R. Jäger and K. J. Ebeling, "High-power VCSEL arrays for emission in the watt regime at room temperature," *IEEE Photon. Technol. Lett*., vol. 13, pp. 173-175, 2001.

[33] C. Yan, Y. Ning, L. Qin, D. Cui, Y. Liu, Y. Sun, Z. Jin, H. Li, G. Tao and C. Wang, "High-power vertical-cavity surface-emitting laser with an extra Au layer," *IEEE Photon. Technol. Lett.*, vol. 17, pp. 1599-1601, 2005.

[34] L. D'Asaro, J. Seurin and J. Wynn, "High-power, high-efficiency VCSELs pursue the goal," *Photonics Spectra*, vol. 39, 2005.

[35] R. A. Morgan, G. D. Guth, M. W. Focht, M. T. Asom, K. Kojima, L. E. Rogers and S. E. Callis, "Transverse mode control of vertical-cavity top-surface-emitting lasers," *IEEE Photon. Technol. Lett.,* vol. 5, pp. 374-377, 1993.

[36] K. L. Lear, R. P. Schneider Jr., K. D. Choquette, S. P. Kilcoyne, J. J. Figiel and J. C. Zolper, "Vertical-cavity surface-emitting-lasers with 21% efficiency by metalorganic vapor

phase epitaxy," in *Conference Digest - IEEE International Semiconductor Laser Conference,* 1994.

[37] C. Jung, R. Jäger, M. Grabherr, P. Schnitzer, R. Michalzik, B. Weigl, S. Müller and K. J. Ebeling, "4.8mW singlemode oxide confined top-surface emitting vertical-cavity laser diodes," *Electron. Lett.,* vol. 33, pp. 1790-1791, 1997.

[38] A. J. Fischer, K. D. Choquette, W. W. Chow, A. A. Allerman, D. K. Serkland and K. M. Geib, "High single-mode power observed from a coupled-resonator vertical-cavity laser diode," *Appl. Phys. Lett.,* vol. 79, pp. 4079-4081, 2001.

[39] D. Zhou and L. J. Mawst, "High-power single-mode antiresonant reflecting optical waveguide-type vertical-cavity surface-emitting lasers," *IEEE J. Quant. Electron.,* vol. 38, pp. 1599-1606, 2002.

[40] A. Haglund, J.S. Gustavsson, J. Vukusic, P. Modh and A. Larsson, "Single fundamental-mode output power exceeding 6 mW from VCSELs with a shallow surface relief," *IEEE Photon. Technol. Lett.,* vol. 16, pp. 368-370, 2004.

[41] N. Samal, S. Johnson, D. Ding, A. Samal, S. Q. Yu and Y. H. Zhang, "High-power single-mode vertical-cavity surface-emitting lasers," *Appl. Phys. Lett.,* vol. 87, pp. 161108, 2005.

[42] M. Orenstein, E. Kapon, J. Harbison, L. Florez and N. Stoffel, "Large two-dimensional arrays of phase-locked vertical cavity surface emitting lasers," *Appl. Phys. Lett.,* vol. 60, pp. 1535-1537, 1992.

[43] R. A. Morgan, K. Kojima, T. Mullally, G. D. Guth, M. W. Focht, R. E. Leibenguth and M. Asom, "High-power coherently coupled 8× 8 vertical cavity surface emitting laser array," *Appl. Phys. Lett.,* vol. 61, pp. 1160-1162, 1992.

[44] G. R. Hadley, "Modes of a two-dimensional phase-locked array of vertical-cavity surface-emitting lasers," *Opt. Lett.,* vol. 15, pp. 1215-1217, 1990.

[45] L. Bao, N. H. Kim, L. J. Mawst, N. N. Elkin, V. N. Troshchieva, D. V. Vysotsky and A. P. Napartovich, "Near-diffraction-limited coherent emission from large aperture antiguided vertical-cavity surface-emitting laser arrays," *Appl. Phys. Lett.,* vol. 84, p. 320, 2004.

[46] D. F. Siriani and K. D. Choquette, "In-phase, coherent photonic crystal vertical-cavity surface-emitting laser arrays with low divergence," *Electron. Lett.,* vol. 46, pp. 712-714, 2010.

[47] J. J. Raftery Jr, A. C. Lehman, A. J. Danner, P. O. Leisher, A. V. Giannopoulos and K. D. Choquette, "In-phase evanescent coupling of two-dimensional arrays of defect cavities in photonic crystal vertical cavity surface emitting lasers," *Appl. Phys. Lett.,* vol. 89, pp. 081119, 2006.

[48] M. Orenstein, E. Kapon, N. Stoffel, J. Harbison, L. Florez and J. Wullert, "Two-dimensional phase-locked arrays of vertical-cavity semiconductor lasers by mirror reflectivity modulation," *Appl. Phys. Lett.,* vol. 58, pp. 804-806, 1991.

[49] J. M. Catchmark, L. Rogers, R. Morgan, M. Asom, G. Guth and D. Christodoulides, "Optical characteristics of multitransverse-mode two-dimensional vertical-cavity top surface-emitting laser arrays," *IEEE J. Quant. Electron.,* vol. 32, pp. 986-995, 1996.

[50] P. Claisse, W. Jiang, P. Kiely, B. Gable and B. Koonse, "Single high order mode VCSEL," *Electron. Lett.,* vol. 34, pp. 681-682, 1998.

[51] F. M. di Sopra, M. Brunner, R. Hoevel, M. Moser and E. E. Kapon, "Continuous-wave operation of phase-coupled vertical-cavity surface-emitting laser arrays," in *Symposium on Integrated Optics,* 2001.

[52] D. Zhou, L. J. Mawst and Z. Dai, "Modal properties of two-dimensional antiguided vertical-cavity surface-emitting laser arrays," *IEEE J. Quant. Electron.,* vol. 38, pp. 652-664, 2002.

[53] P. Debernardi, G. P. Bava, F. Monti di Sopra and M. B. Willemsen, "Features of vectorial modes in phase-coupled VCSEL arrays: experiments and theory," *IEEE J. Quant. Electron.,* vol. 39, pp. 109-119, 2003.

[54] D. Serkland, K. Geib, G. Hadley and G. Peake, "Leaky-mode coupled vertical-cavity surface-emitting lasers fabricated using a dielectric distributed bragg reflector," in *Lasers and Electro-Optics Society, 2004. LEOS 2004. the 17th Annual Meeting of the IEEE,* 2004.

[55] J. W. Shi, J. L. Yen, C. H. Jiang, K. M. Chen, T. J. Hung and Y. J. Yang, "Vertical-cavity surface-emitting lasers (VCSELs) with high-power and single-spot far-field distributions at 850-nm wavelength by use of petal-shaped light-emitting apertures," *IEEE Photon. Technol. Lett.,* vol. 18, pp. 481-483, 2006.

[56] A. S. Gadallah and R. Michalzik, "High-output-power single-higher-order transverse mode VCSEL with shallow surface relief," *IEEE Photon. Technol. Lett.,* vol. 23, pp. 1040-1042, 2011.

[57] M. T. Johnson, D. F. Siriani, P. O. Leisher and K. D. Choquette, "In-phase antiguided bottom-emitting vertical cavity laser arrays ," *Electron. Lett.,* vol. 49, pp. 897-898, 2013.

[58] D. F. Siriani and K. D. Choquette, "Chapter 6 - coherent coupling of vertical-cavity surface-emitting laser arrays," in *Semiconductors and Semimetals*, San Diego, CA: Elsevier, 2012, pp. 227-267.

[59] D. Botez and D. R. Scifres, *Diode Laser Arrays.* Cambridge University Press, 2005.

[60] D. Botez, L. Mawst, P. Hayashida, G. Peterson and T. Roth, "High-power, diffraction-limited-beam operation from phase-locked diode-laser arrays of closely spaced 'leaky' waveguides (antiguides)," *Appl. Phys. Lett.,* vol. 53, pp. 464-466, 1988.

[61] L. Mawst, D. Botez, T. Roth and G. Peterson, "High-power, in-phase-mode operation from resonant phase-locked arrays of antiguided diode lasers," *Appl. Phys. Lett.,* vol. 55, pp. 10-12, 1989.

[62] D. Botez, "High-power monolithic phase-locked arrays of antiguided semiconductor diode lasers," in *Optoelectronics, IEE Proceedings J,* 1992.

[63] M. T. Johnson, D. F. Siriani, J. D. Sulkin and K. D. Choquette, "Phase and coherence extraction from a phased vertical cavity laser array," *Appl. Phys. Lett.,* vol. 101, p. 031116, 2012.

[64] M. T. Johnson, M. T. Siriani and K. D. Choquette, "Beam steering mechanism in phased vertical cavity laser arrays," in *IEEE Photonics Conference,* Bellevue, Washington, 2013.

[65] E. Kapon, J. Katz and A. Yariv, "Supermode analysis of phase-locked arrays of semiconductor lasers," *Opt. Lett.,* vol. 9, pp. 125-127, 1984.

[66] E. Kapon, L. Lu, Z. Rav-Noy, M. Yi, S. Margalit and A. Yariv, "Phased arrays of buried-ridge InP/InGaAsP diode lasers," *Appl. Phys. Lett.,* vol. 46, pp. 136-138, 1985.

[67] P. Eliseev, R. Nabiev and Y. M. Popov, "Analysis of laser-structure anisotropic semiconductors by the Bloch-function method," *Journal of Soviet Laser Research,* vol. 10, pp. 449-458, 1989.

[68] D. Siriani and K. Choquette, "Reduced loss and improved mode discrimination in resonant optical waveguide arrays," *Electron. Lett.,* vol. 48, pp. 591-593, 2012.

[69] D. Botez, L. Mawst and G. Peterson, "Resonant leaky-wave coupling in linear arrays of antiguides," *Electron. Lett.,* vol. 24, pp. 1328-1330, 1988.

[70] D. Botez, L. J. Mawst, G. L. Peterson and T. J. Roth, "Phase-locked arrays of antiguides: model content and discrimination," *Quantum Electronics, IEEE Journal Of,* vol. 26, pp. 482-495, 1990.

[71] A. C. Lehman, J. J. Raftery Jr, A. J. Danner, P. O. Leisher and K. D. Choquette, "Relative phase tuning of coupled defects in photonic crystal vertical-cavity surface-emitting lasers," *Appl. Phys. Lett.,* vol. 88, pp. 021102, 2006.

[72] J. W. Goodman, *Introduction to Fourier Optics.* Roberts & Company Publishers, 2005.

[73] D. F. Siriani and K. D. Choquette, "Implant defined anti-guided vertical-cavity surface-emitting laser arrays," *IEEE J. Quant. Electron.,* vol. 47, pp. 160-164, 2011.

[74] F. Koyama and X. Gu, "Beam steering, beam shaping, and intensity modulation based on VCSEL photonics," *IEEE J. Sel. Top. Quant. Electron.*, vol. 19, p. 1701510, 2013.

[75] S. Wang and H. G. Winful, "Propagation model for the dynamics of gain-guided semiconductor laser arrays," *J. Appl. Phys.,* vol. 73, pp. 462-464, 1993.

[76] P. Debernardi and G. P. Bava, "Coupled mode theory: a powerful tool for analyzing complex VCSELs and designing advanced device features," *IEEE J. Sel. Top. Quant. Electron.,* vol. 9, pp. 905-917, 2003.

[77] F. Mogensen, H. Olesen and G. Jacobsen, "Locking conditions and stability properties for a semiconductor laser with external light injection," *IEEE J. Quant. Electron.,* vol. 21, pp. 784-793, 1985.

[78] R. Lang, "Injection locking properties of a semiconductor laser," *IEEE J. Quant. Electron.,* vol. 18, pp. 976-983, 1982.

[79] H. Winful and S. Wang, "Stability of phase locking in coupled semiconductor laser arrays," *Appl. Phys. Lett.,* vol. 53, pp. 1894-1896, 1988.

[80] K. D. Choquette and K. M. Geib, "Fabrication and performance of vertical-cavity surface-emitting lasers," in *Vertical-Cavity Surface-Emitting Lasers: Design, Fabrication, Characterization, and Applications*, C. W. Wilmsen and H. Temkin, Eds. Cambridge University Press, 2001, pp. 193.

[81] Y. K. Kim, A. J. Danner, J. J. Raftery and K. D. Choquette, "Focused ion beam nanopatterning for optoelectronic device fabrication," *IEEE J. Sel. Top. Quant. Electron.,* vol. 11, pp. 1292-1298, 2005.

[82] M. T. Johnson, D. F. Siriani and K. Choquette, "Beam Steering Modulation with Phased Vertical Cavity Laser Aarrys," presented at the IEEE Photonics Conference, Burlingame, CA, Sep. 2013.

[83] M. T. Johnson, D. F. Siriani, M. P. Tan and K. D. Choquette, "High speed beam steering with phased vertical cavity laser arrays," *IEEE J. Sel. Top. Quant. Electron.,* vol. 19, p. 1701006, 2013.

[84] H. G. Winful and R. K. Defreez, "Dynamics of coherent semiconductor laser arrays," in *Diode Laser Arrays*, D. Botez and D. R. Scifres, Eds. Cambridge University Press, 1994, pp. 226-230.

[85] A. C. Lehman, J. J. Raftery, P. S. Carney and K. D. Choquette, "Coherence of photonic crystal vertical-cavity surface-emitting laser arrays," *IEEE J. Quant. Electron.,* vol. 43, pp. 25-30, 2007.

[86] L. D. A. Lundeberg, G. P. Lousberg, D. L. Boiko and E. Kapon, "Spatial coherence measurements in arrays of coupled vertical cavity surface emitting lasers," *Appl. Phys. Lett.,* vol. 90, p. 021103, 2007.

[87] R. K. Huang, B. Chann, L. J. Missaggia, S. J. Augst, M. K. Connors, G. W. Turner, A. Sanchez-Rubio, J. P. Donnelly, J. L. Hostetler and C. Miester, "Coherent combination of slab-coupled optical waveguide lasers," in *Proceedings of SPIE,* 2009.

[88] N. K. Dutta, L. W. Tu, G. Hasnain, G. Zydzik, Y. H. Wang and A. Y. Cho, "Anomalous temporal response of gain guided surface emitting lasers," *Electron. Lett.,* vol. 27, pp. 208-210, 1991.

[89] G. Hasnain, K. Tai, L. Yang, Y. Wang, R. Fischer, J. D. Wynn, B. Weir, N. Dutta and A. Cho, "Performance of gain-guided surface emitting lasers with semiconductor distributed Bragg reflectors," *IEEE J. Quant. Electron.,* vol. 27, pp. 1377-1385, 1991.

[90] B. R. Bennett, R. A. Soref and J. A. Del Alamo, "Carrier-induced change in refractive index of InP, GaAs and InGaAsP," *IEEE J. Quant. Electron.,* vol. 26, pp. 113-122, 1990.

[91] G. R. Hadley, "Effective index model for vertical-cavity surface-emitting lasers," *Opt. Lett.,* vol. 20, pp. 1483-1485, 1995.

[92] W. Schmid, C. Jung, B. Weigi, G. Reiner, R. Michalzik and K. Ebeling, "Delayed self-heterodyne linewidth measurement of VCSELs," *IEEE Photon. Technol. Lett.,* vol. 8, pp. 1288-1290, 1996.

[93] H. Yoo, J. Hayes, E. Paek, J. Harbison, L. Florez and Y. Kwon, "Phase-locked two-dimensional arrays of implant isolated vertical cavity surface emitting lasers," *Electron. Lett.,* vol. 26, pp. 1944-1946, 1990.

[94] R. Geels, S. Corzine, J. Scott, D. Young and L. Coldren, "Low threshold planarized vertical-cavity surface-emitting lasers," *IEEE Photon. Technol. Lett.,* vol. 2, pp. 234-236, 1990.

[95] P. Goorjian and N. Cun-Zheng, "Ultrafast beam self-switching by using coupled vertical-cavity surface-emitting lasers," *Journal of Modern Optics,* vol. 49, pp. 707-718, 2002.

[96] D. Botez, "Monolithic phase-locked semiconductor laser arrays," in *Diode Laser Arrays*, Cambridge, UK: Cambridge University Press, 2005, pp. 1-71.

[97] A. C. Lehman and K. D. Choquette, "One-and two-dimensional coherently coupled implant-defined vertical-cavity laser arrays," *IEEE Photon. Technol. Lett.,* vol. 19, pp. 1421-1423, 2007.

[98] R. G. Hunsperger, "Waveguide fabrication techniques," in *Integrated Optics: Theory and Technology*, R. G. Hunsperger, Ed. Springer, 1984, p. 53.

[99] M. Mentzer, M. Wlodawski, R. Hunsperger, J. Zavada, H. Jenkinson and T. Gavanis, "Characterization and optimization of proton implanted optical (1.15 μm) GaAs waveguides," in *1983 Technical Symposium East,* 1983.

[100] S. L. Chuang, *Physics of Photonic Devices.* John Wiley & Sons New York, 2009.

[101] S. Pearton, "Ion implantation for isolation of III-V semiconductors," *Materials Science Reports,* vol. 4, pp. 313-363, 1990.

[102] E. Garmire, H. Stoll, A. Yariv and R. Hunsperger, "Optical waveguiding in proton-implanted GaAs," *Appl. Phys. Lett.,* vol. 21, pp. 87, 1972.

[103] L. Bao, N. Kim, L. J. Mawst, N. Elkin, V. Troshchieva, D. Vysotsky and A. Napartovich, "Modeling, fabrication, and characterization of large aperture two-dimensional antiguided vertical-cavity surface-emitting laser arrays," *IEEE J. Sel. Top. Quant. Electron.,* vol. 11, pp. 968-981, 2005.

[104] H. G. Winful, "Instability threshold for an array of coupled semiconductor lasers," *Physical Review A,* vol. 46, pp. 6093-6094, 1992.